Copper Metallization with an Electron Cyclotron Resonance Plasma Source

by

Khashayar Shadman

B.S. Nuclear and Electrical Engineering (1994)

University of California Berkeley

Submitted to the Department of Nuclear Engineering in Partial Fulfillment of the Requirements for the Degree of Master of Science in Nuclear Engineering

at the

Massachusetts Institute of Technology

June 1998

Signature of Author.....
Department of Nuclear Engineering
March 26, 1998

Certified by.....
Dr. Kevin Wenzel
Thesis Reader

Certified by.....
Jeffrey Philip Freidberg
Professor of Nuclear Engineering
Thesis Supervisor

Accepted by.....
Lawrence Mark Lidsky
Professor of Nuclear Engineering
Chairman Department Committee on Graduate Students

Copper Metallization with an Electron Cyclotron Resonance Plasma Source

by

Khashayar Shadman

B.S. Nuclear and Electrical Engineering (1994)

University of California Berkeley

Submitted to the Department of Nuclear Engineering in Partial Fulfillment of the Requirements for the Degree of Master of Science in Nuclear Engineering

ABSTRACT

An "electron cyclotron resonance" plasma source, used for physical vapor deposition of copper into sub-micron features, was studied to determine whether parameters, such as gas atom density, electron density and temperature, surface bias, and copper ionization fraction at the deposition surface, influenced fill quality of the features. The results indicated that the fill quality was insensitive to all parameters except for the surface biasing conditions; however, with the use of an argon plasma, the bias was limited to less than $\approx |-40V|$ due to the sputtering of the dielectric features by the argon ions (a phenomenon know as faceting). Switching to a copper evaporative system allowed for a pure copper plasma, enabling the use of greater (in magnitude) surface bias , $\approx |-200V|$, before faceting by copper ions was observed. The fill quality of the features degraded with moderate bias ($\leq |-100V|$) but improved with bias $> |-150V|$. These results suggest that one formula for successful metallization is the use of an etch-resistant dielectric material in conjunction with large negative surface bias.

Thesis Supervisor: Jeffrey Philip Feidberg

Title: Professor of Nuclear Engineering

ACKNOWLEDGMENTS

The research was conducted at Applied Science and Technology (Astex). I thank the company president, Dr. Richard Post, and the 'project 7' group (Dr. Xing Chen, Dr. John Urban, Dr. Bill Holber, Dr. Xinyu Xang, Mr. Larry Bourget, and Mr. Wayne Brooks) for the friendship and the supervision. In addition, I thank Dr. Kevin W. Wenzel and Professor Jeffrey Philip Freidberg for their continuing support of my education at MIT.

TABLE OF CONTENTS

CHAPTER 1

1.0: INTRODUCTION

As chip sizes decrease (because of the demand for compact, light-weight devices), and the demand for more memory and specialized functions increase, the number of transistors per chip increases. This increase results in increased metal interconnection density, which enhances the contribution of the RC-delay from the metal interconnects, thereby limiting the speed of the chip (which is inversely proportional to the RC time constant). To understand the limitation imposed on the chip speed by the increased interconnect density, a simple model[1] for the line resistance and capacitance (per unit length) of the interconnect will be used. Figure 1.0-1 illustrates the simplified model of the interconnection layers.

FIGURE 1.0-1: A CROSS-SECTION OF THE METAL/DIELECTRIC INTERCONNECTION LAYERS

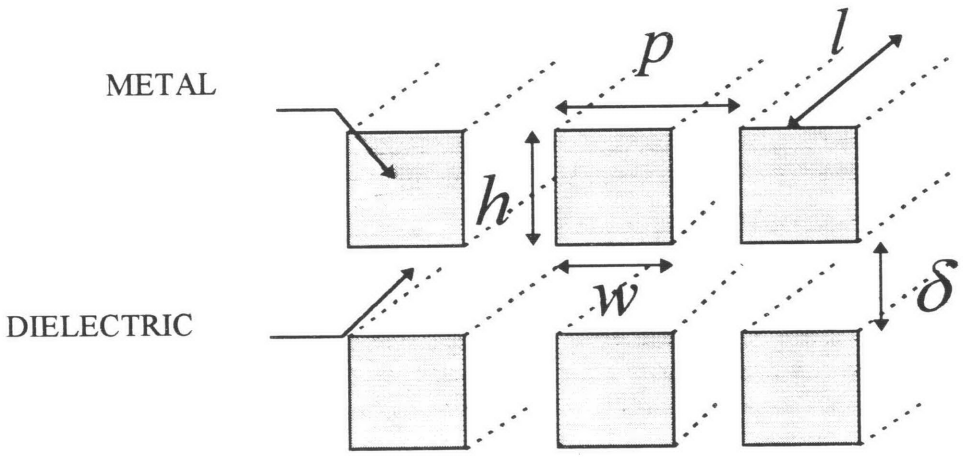

The line resistance and the line capacitance are given by the following formulas:

[1] Solid State Technology, Sept. 96, pp. 105-111

$$R \equiv \frac{\rho}{wh}\left(ohms/m\right) : [1.0-1]$$

$$C_{lateral} \equiv 2\varepsilon_r \varepsilon_0 \frac{h}{p-w}\left(farads/m\right) : [1.0-2]$$

$$C_{vertical} \equiv 2\varepsilon_r \varepsilon \frac{w}{\delta}\left(farads/m\right) : [1.0-3]$$

where

ρ is the metal resistivity in $ohm-m$

w is the width of the metal

h is the metal height

p is the average pitch (the width of one metal-dielectric line) and

$p-w$ is the intra-level dielectric thickness

δ is the inter-level dielectric thickness

$\varepsilon_r, \varepsilon_0$ are the relative permitivity of the dielectric and the permitivity of free space respectively

If the width of the metal is taken to be a fraction ' f ' of the pitch, then the formula for the ' RC ' delay becomes:

$$RC = 2\rho\varepsilon_r\varepsilon_0\left(\frac{l}{p}\right)^2\left\{\frac{1}{f(1-f)}+\frac{p^2}{h\delta}\right\} : [1.0-4]$$

where

l is the total line length

and the optimum value for f that will minimize the ' RC ' is 1/2

By inserting the optimum value for f and defining the aspect ratio of the trench $A \equiv \frac{h}{w}$, and noting that the inter-level dielectric thickness is of the order of the trench height $(\delta \approx h)$, the formula for the RC delay becomes:

$$RC \approx 8\rho\varepsilon_r\varepsilon_0\left(\frac{l}{p}\right)^2\left\{1+\frac{1}{A^2}\right\} : [1.0-5]$$

The formula for the RC time constant demonstrates the $(1/p^2)$ dependence of the time constant on the pitch . As the interconnect density increases, the pitch decreases, drastically increasing the interconnect 'RC' time constant. Inserting typical values for the variables:

$$\begin{aligned}
&\rho_{Al} \cong 1.7\cdot 10^{-8}\,\Omega - m \\
&\varepsilon_r^{SiO_2} = 4 \\
&l \approx 1cm \\
&p \approx .5\mu m \\
&A \approx 2
\end{aligned} \quad ,$$

we find an 'RC' value of $2.4n\,\text{sec}$, corresponding to a frequency of $400MHz$. Hence, we can see that the interconnection 'RC' delay will become a hindering factor as the industry pushes for a smaller chip size ($\Rightarrow p < .5\mu m$) and greater chip 'speeds' ('speeds' of $\approx 1GHz$).

To compensate for this increase in the RC-delay, the industry is investigating a few options:

1) **the use of a metal with lower resistivity**: at the present aluminum $(3\ \mu ohm\cdot cm)$ is the standard choice, but copper $(1.7\ \mu ohm\cdot cm)$ will be the choice for the future.

2) **the use of a dielectric with lower relative permitivity** : at the present SiO_2 (relative permitivity of 4) is the prevalent choice, but the use of some type of polymers with relative permitivity of 2 is being investigated. There are issues of structural integrity and material compatibility.

3) **increasing the number of metal interconnect layers**: structural integrity and the increase in the process time limit the number of layers to less than 10.

4) **increasing the vertical distance between the metal lines**: the increase in the vertical distance between the metal lines will decrease the vertical capacitance, but the gain from this is limited by the lateral capacitance; in addition, depositing more dielectric between the metal lines increases the process time.

5) **increasing the aspect ratio of the metal trench to compensate for the decrease in the current carrying area due to the decrease in the pitch(line resistance is inversely proportional to the area)** : there is not much gain in increasing the aspect ratio beyond a value of 3 because of the increase in the lateral capacitance; currently the industry is implementing metal trenches with aspect ratios of ~ 1. **The need for increasing the metal trench aspect ratio has motivated the research for this thesis.**

THE PROCESS OF METALLIZATION

Understanding the deposition of metal in high aspect ratio $(\geq 3/1)$ features requires a description of the metallization process (the process by which the metal interconnection layers are created). The process is illustrated in figure 1.0-2:

FIGURE 1.0-2: ILLUSTRATION OF THE METALIZATION PROCESS

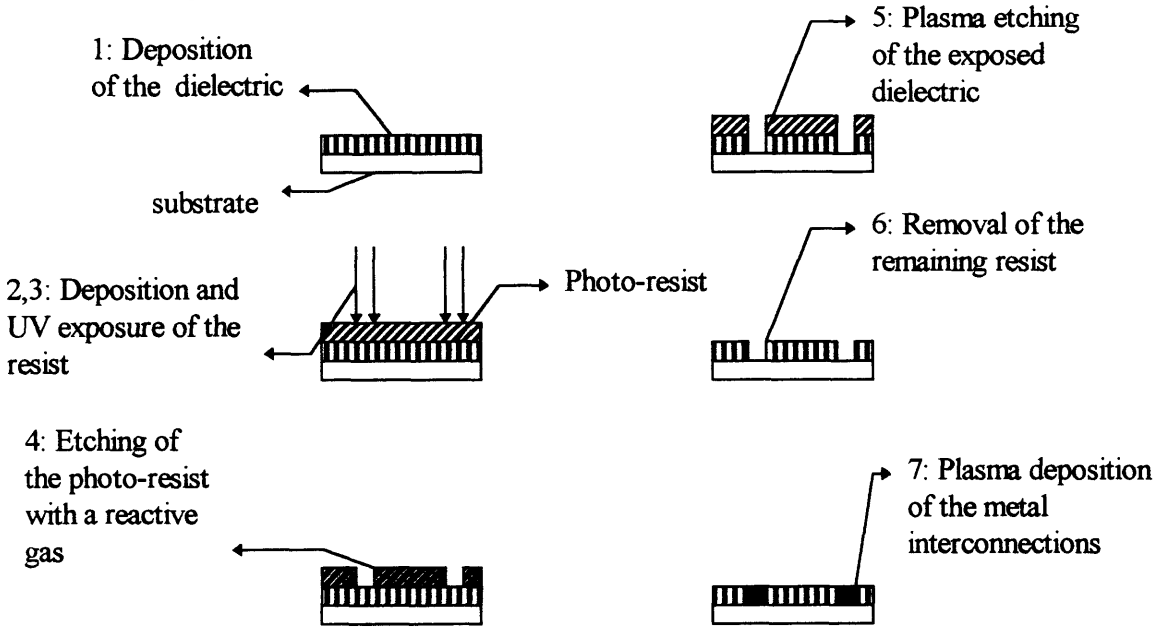

1) a layer of metal (such as aluminum)or dielectric (such as SiO_2) is deposited and chemically polished.

2) a layer of photo-resist is deposited on the metal or dielectric; a photo- resist is a material with chemical bonds that are sensitive to ultra-violet ray exposure.

3) once the layer of resist has been applied, UV rays are directed onto the resist through a patterned mask.

4) with the pattern imprinted into the resist, the resist is exposed to a plasma with a reactive gas (such as fluorine or chlorine); the plasma dissociates the gas molecules into atoms; these atoms subsequently etch the part of the resist that was exposed to the UV and leave the underlying metal or dielectric exposed.

5) the exposed metal or dielectric is then directionally etched (plasma enhanced etching) with halogens to produce the metal or dielectric trenches.

6) once the metal or dielectric trenches are formed, the remaining resist is exposed to UV and removed.

7) the dielectric or metal is then deposited via (chemical vapor deposition) ;the overburden is removed, and the surface polished .

8) the process is repeated for the next layer.

As the industry is pushing for the use of lower resistive metals, copper will replace aluminum. Unfortunately, there is no practical method for chemically etching copper (because of the difficulty in the removal of the reaction by-products resulting from their low vapor pressure); therefore, the process must begin with the deposition of a layer of dielectric, and the metal must be deposited into the trenches formed by etching the dielectric; hence, the need for the metalization of large aspect ratio features.

There are a few methods for the deposition of metal into large aspect ratio sub-micron trenches of which I will mention two:

1) CVD (chemical vapor deposition): The idea is to expose the metal source to a reactive gas; the gas then reacts with the metal to form a metal vapor compound, which is then transported to the wafer where it is deposited once the compound dissociates either upon contact with the dielectric or with the aid of another gas.

There are inherent disadvantages with CVD. It requires the use of highly reactive chemical compounds (toxic to humans and damaging to the environment), which require care to implement and dispose, rendering the process very expensive. Even for the less reactive compounds such as the metal-organic compounds, there are concerns about trapped impurities within the metal fill resulting from the compound's large affinity for attachment to the metal atom.

These disadvantages have rendered a second method more attractive for metallization: PVD.

2) PVD (physical vapor deposition): This method relies on physical sputtering of the metal source; sputtering is the removal of atoms from their lattice through bombardment by other energetic atoms (or more likely, ions). Therefore, there is no need for reactive compounds.

Both CVD and PVD either benefit or rely on the use of a plasma source; to understand the need for a plasma for CVD and PVD applications, the basic properties of plasmas must be explained. Plasmas are created by the input of energy into the few free electrons in a gas (these electrons are created from the ionizing collisions between photons and the background gas atoms); this energy input can be from a voltage source, an inductive drive mechanism, or from a microwave source coupled with the use of electromagnets. The energetic electrons subsequently collide with the bound electrons in the gas atoms. The collisions result in the excitation and in the eventual ionization of the gas atoms. The ejected electrons are then accelerated in the same manner as the original free electrons via the mechanisms discussed and ionize more atoms. The result is a sea of atoms, ions, and electrons referred to as a plasma . The electrons are much less massive than the ions in the plasma (for an argon plasma, the electron to ion mass ratio is ~1/70,000); therefore, the electrons are much more mobile. This difference in mobility results initially in the dominance of the electron flux contribution to the boundary of the plasma source. The charge separation resulting from the excess electron flux to the plasma boundaries creates an electric field, which enhances the ion mobility to the boundaries while simultaneously retarding the electron flux. Equilibrium is reached when

the electric field created by the charge separation reaches the strength to correct for the initial disparity in the ion and electron flux to the boundaries. The large mobility of the electrons yields a very conductive plasma; therefore, the electric field created by the charge separation can not penetrate far into the plasma. The distance of penetration, denoted as the sheath thickness is related to the Debye length (~10's of microns):

$$\lambda_D \equiv \frac{v_{Te}}{\omega_{pe}} \equiv \frac{\sqrt{(T_e/m_e)}}{\sqrt{\left(\frac{e^2 n_e}{\varepsilon_0 m_e}\right)}} = \sqrt{\frac{\varepsilon_0 T_e}{e^2 n_e}} : [1.0 - 6] \ ,$$

where

v_{T_e} is $\sqrt{2}$ times the electron thermal speed,

ω_{pe} is the electron plasma radian frequency,

T_e is the electron temperature,

n_e is the electron density,

e is the electron charge,

and

ε_0 is the permitivity of free space.

The Debye length is proportional to the ratio of the velocity with which the electric field can penetrate the plasma (the electron thermal speed) to the electron response frequency. At greater distances from the boundary, the plasma is quasi-neutral and free of any significant electric fields (there is a region between the sheath and the quasi-neutral region denoted as the pre-sheath where there is a small potential drop of about $\left(\frac{T_e}{2e}\right)$).

Therefore, the electric potential in the plasma has essentially a flat profile followed by a

sharp drop to the boundary within the sheath. Sheath formation is the essential property of the plasma that renders it attractive for directional etching and deposition in metallization for ULSI technology. Another attractive property of the plasma is its ability to sustain a very high electron temperature (~1-10eV), allowing for the disassociation of gas molecules into reactive atoms; these reactive atoms are a necessity in the applications of chamber cleaning and environmental waste disposal.

As mentioned before, there are different methods for igniting a plasma. The method of choice depends on the application. For metallization, the important criterion (besides actually filling the trenches with metal) are spatial uniformity and process rates. The uniformity is a function of spatial power absorption and particle energy transport. The process rate is a function of the plasma (ion) current density to the wafer, which is proportional to the electron density and to the square root of the electron temperature (a deposition rate of $0.1\,\mu m/\min$ requires a current density of $2.3\,mA/cm^2$, which implies that $f^{sub}_{Cu^+/Ar^+} n_e(T_e)^{1/2} \approx 2.3*10^{11}(eV)^{1/2}/cm^3$; for a typical copper-to-argon ion flux fraction at the substrate of $f^{sub}_{Cu^+/Ar^+} \approx 10\%$ this product may be realized with $n_e \approx 10^{12}/cm^3$ and $T_e \approx 5eV$).

Therefore, high process rates require the use of a plasma source that can sustain a 'high' electron density and temperature. One such source is an electron cyclotron resonance (ECR) plasma source.

FIGURE 1.0-3:A SIMPLE SCHEMATIC OF THE ECR SOURCE AND THE ASSOCIATED HARDWARE

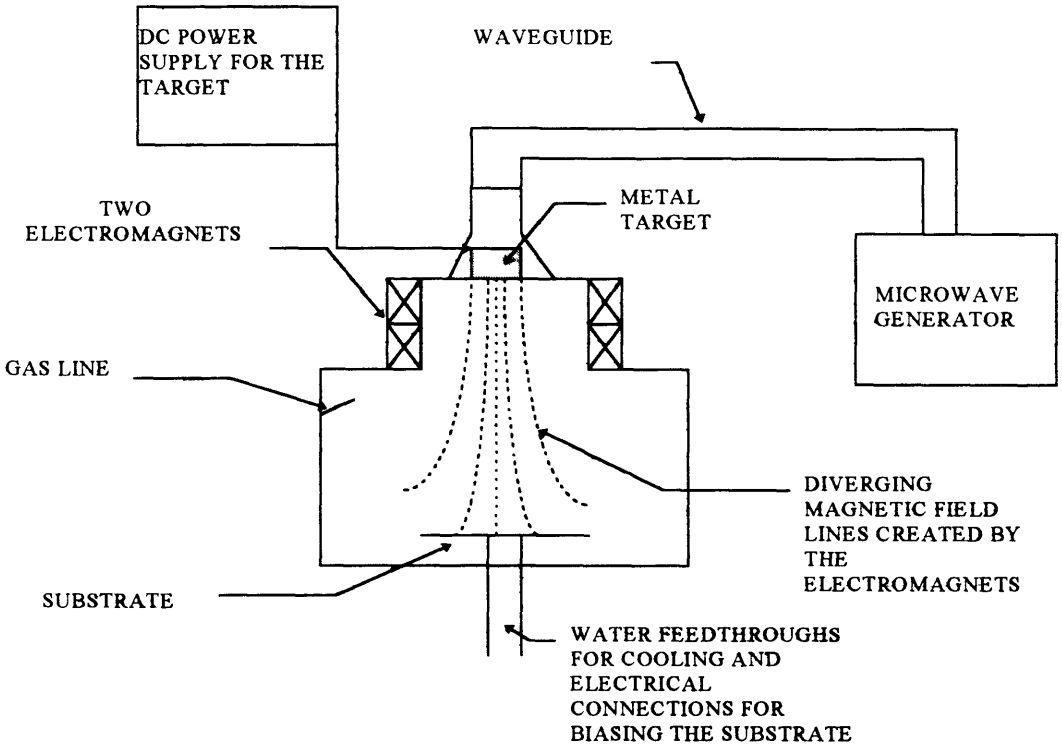

As illustrated in figure 1.0-3, an ECR source consists of a microwave generator and wave-guide, plus electromagnets. The electromagnets create an axial magnetic field , which is essential for the provision of

a) the radial confinement for the plasma charged particles (ions and electrons)

b) the cyclotron motion of the electrons to which the right hand circularly polarized component of the launched microwaves couple.

To understand the ECR source's ability to sustain high electron densities and temperatures, a zero dimensional energy conservation model (which was adopted by Liebermann et al.[2]) will be employed.

Assuming an optically thin plasma and negligible radiation energy loss from:

[2] Liebermann and Lichtenberg, Principles of Plasma Discharges and Materials Processing, 1994, Chp. 10

a) ion-ion collisions

b) ion-electron collisions

c) electron-electron collisions

d) the electron cyclotron motion

and also assuming

a) a single ion species

b) only singly ionized ions $\Rightarrow \frac{n_{Ar^{2+}}}{n_{Ar^{+}}} << 1$; this is a good approximation because the energy (29eV) required to doubly ionize argon $\left(Ar^{+} \Rightarrow Ar^{2+}\right)$ is much greater than the energy $(\approx 16eV)$ required to singly ionize $\left(Ar^{0} \Rightarrow Ar^{+}\right)$, and the cross-section for double ionization is much less, and

c) negligible ion energy loss to the neutrals from charge exchange and elastic collisions

the radiation energy lost (E_c) per electron-ion pair created from ionization collisions can be derived from the following argument:

In a time "dt", the number of electron-ion pairs created per unit volume from ionizing collisions is given by

$$\left(n_e n_g K_{iz0} + n_i n_g K_{iz1}\right)dt : [1.0-7]$$

During that time, the total radiation energy loss in the bulk of the plasma from the various reactions is given by :

$$n_e n_g dt\{K_{iz0}E_{iz0} + (n_i/n_e)K_{iz1}E_{iz1} + K_{ex}E_{ex} + K_{el}[3(m_e/m_g)T_e] + (n_i/n_g)K_{rec}E_{rec}\} : [1.0-8]$$

where

n_e is the electron density;

n_i is the ion density (singly ionized);

n_g is the gas atom density;

K_{iz0} is the reaction rate coefficient for electron-neutral ionization;

K_{iz1} is the reaction rate coefficient for ion-neutral ionization;

K_{ex} is the reaction rate coefficient for excitation collisions with neutrals;

K_{el} is the reaction rate coefficient for elastic collisions;

K_{rec} is the reaction rate coefficient for electron-ion recombination;

E_{iz0} is the average radiation energy loss in the electron-neutral ionizing collisions;

E_{iz1} is the average radiation energy loss in the ion-neutral ionizing collisions;

E_{ex} is the average radiation energy loss in electron excitation collisions with neutrals;

E_{el} is the average energy loss to the neutrals in the electron-neutral elastic collisions;

E_{rec} is the average radiation energy loss in the electron-ion recombination reactions;

and

$$K_j E_j \equiv \frac{1}{n_1 n_2} \iint d^3 v_1 d^3 v_2 v_r f_1(\vec{v}_1) f_2(\vec{v}_2) \int d\Omega \cdot \frac{d\sigma_j}{d\Omega} \cdot \Delta E_j(v_r, \Omega);$$

where

n_1, n_2 are the densities of the reacting species;

f_1, f_2 are the velocity distribution functions of the reacting species;

$v_r \equiv \left\| \vec{v}_1 - \vec{v}_2 \right\|$ is the relative speed of the two species;

ΔE_j is (with the exception of the electron-neutral elastic collisions) the radiation energy loss for the reaction due to the change in states of the reacting species;

$\frac{d\sigma_j}{d\Omega}$ is the differential cross section for the specific reaction; and

the last integral represents the average energy loss for a given initial state (v_r), where the average is taken over all the possible final states for the particular reaction.

The radiation energy loss per electron-ion pair created (E_c) is then given by the ratio of equations 1.0-8 and 1.0-7:

$$E_c \equiv \frac{K_{iz0}E_{iz0} + (n_i/n_e)K_{iz1}E_{iz1} + K_{ex}E_{ex} + K_{el}\left[3(m_e/m_g)T_e\right] + (n_i/n_g)K_{rec}E_{rec}}{K_{iz0} + (n_i/n_e)K_{iz1}} : [1.0-9]$$

In equation 1.0-9, the average energy loss for elastic collisions is calculated to be[3]

$$E_{el} \approx 3 * \frac{m_e}{m_g} * T_e$$

assuming

a) a Maxwellian electron velocity distribution function and a stationary 'cold' neutral background, and

[3] Liebermann and Lichtenberg, Principles of Plasma Discharges and Materials Processing, 1994, Chp. 3

b) a cross section for the reaction derived from a model that accounts for the polarization of the atom by the electron's electric field.

We note that with the exception of K_{iz1}, which is a function of the ion and neutral temperatures, the remaining reaction rates (which involve the electron distribution function), to a good approximation, are only a function of the electron temperature. The reason for this simplification is that the average electron speed is much greater than both the ion and the neutral speeds; hence, for the reaction rates that involve the electron, the ion and the neutral distribution functions can be treated as a delta function centered at their drift speed.

Besides the energy loss channels within the bulk of the plasma, there are energy losses at the plasma surface boundaries due to particle losses. The average energy loss per unit area of the plasma boundary is just the particle kinetic energy averaged over the particle flux normal to the surface. For this calculation, the ions are treated as a cold fluid (the distribution function is approximated as a delta function with a directed energy of "E_{sheath}" normal to the boundary, where E_{sheath} is the energy gained through the sheath). The ion average energy loss is then E_{sheath} :

$$E_{sheath} \equiv \left(V_p - V_f\right) + \left(V_f - V_{sub}\right)$$

V_p = the plasma potential relative to the system ground

V_f = the floating potential relative to the system ground

V_{sub} = the substrate voltage relative to the system ground

$V_{pf} \equiv V_p - V_f \approx \left(3.34 + 0.5 * \ln\left(m_i / m_H\right)\right) * T_e$; (for a Maxwellian electron velocity distribution function)

m_i / m_H = the ratio of the ion mass to the proton mass

T_e = electron temperature in eV

for an argon plasma $\left(m_i \approx 40 m_H\right) \Rightarrow V_{pf} \approx 5.2 T_e$.

The electron distribution function is assumed to be Maxwellian, yielding an average energy loss to the boundaries of $2T_e$. To obtain the energy loss to the plasma boundary per electron-ion pair created, quasi-neutrality $\left(n_e \approx n_i\right)$ and particle conservation is invoked: at equilibrium, the electron and ion creation rates must balance their loss rates. Assuming that the dominant species comprise only neutrals and singly charged particles, the ion and electron creation and loss rates are equal:

$$\sum_b \Gamma_{ib} A_b = \sum_b \Gamma_{eb} A_b = \left(n_e n_g K_{iz0} + n_i n_g K_{iz1} - n_e n_i K_{rec}\right) \cdot Vol : [1.0 = 10]$$

Γ_{ib}, Γ_{eb} are the electron and ion fluxes at the boundary

$$\Gamma_{ib} = n_{sb} U_b$$

$$\Gamma_{eb} = \frac{1}{4} n_{sb} V_{eb}$$

$$V_{eb} \equiv \left[8 T_{eb} / \pi m_e\right]^{1/2}$$

A_b is the area of the particular boundary

T_{eb} is the electron temperature at the boundary

$U_b \equiv \left(T_{eb} / m_i\right)^{1/2}$; the Bohm Sheath velocity

n_{sb} is the electron (=ion) density at the sheath

Together, the particle and energy conservation equations yield:

$$\left(K_{iz0}/U_b\right)\left[1+\left(K_{iz1}/K_{iz0}\right)-\left(n_e/n_g\right)\left(K_{rec}/K_{iz0}\right)\right]=\left(\sum_b\left(H_{Teb}\right)^{1/2}H_{nb}A_b\right)\Big/N_g \quad :[1.0-11]$$

$$n_e=\frac{P_{abs}}{K_{iz0}N_g\left[\left(E_b+E_c\right)\left(1+K_{iz1}/K_{iz0}\right)-E_b\left(n_eK_{rec}/n_gK_{iz0}\right)\right]} \quad :[1.0-12]$$

a) $E_b \equiv \sum_b\left(2T_{eb}\Gamma_{eb}A_b+E_{sheathb}\Gamma_{ib}A_b\right)\Big/\sum_b\Gamma_{ib}A_b$

b) $N_g \equiv n_gVol$; Vol is the plasma volume, and N_g is the total number of gas atoms

c) $H_{Teb} \equiv T_{eb}/T_e$; the ratio of the electron temperature at the boundary to that in the bulk plasma

d) $H_{nb} \equiv n_b/n_e$; the ratio of the electron density at the boundary to that in the bulk plasma

e) the sum is over all the boundaries

f) P_{abs} is the absorbed power (Microwave heating, DC bias, inductive drive.....)

g) $n_i+n_g=n_{g0} \equiv \left(3*10^{13}/cm^3\right)*\left(\mathrm{Pr}/(mtorr)\right)$; typically $\frac{n_i}{n_g}\approx 1\%$;

therefore, to a good approximation $n_g \cong n_{g0}$.

If recombination is neglected, then the particle conservation equation 1.0-11, will determine the bulk electron temperature directly provided that

a) the ion-neutral ionization rate is negligible (otherwise the ion and the neutral temperatures must be determined)

b) the ion and neutral drift speeds are negligible when compared to the average electron speed

Once the electron temperature is known, the electron density will be determined from equation 1.0-12. If recombination can not be ignored, then equations 1.0-11 and 1.0-12 will have to be solved simultaneously. If a second ion species is added (from sputtering copper into the plasma for example), then there will be some modifications to the above equations:

a) the added effect of (ionization, excitation, and recombination of copper atoms and ions and the copper ion flux to the boundaries) to the particle and energy conservation equations

b) the gas density will comprise both copper and argon

c) quasi-neutrality $\Rightarrow n_e \approx n_{Ar^+} + n_{Cu^+}$.

This simple global model readily demonstrates the benefits of an ECR source as compared to a typical DC discharge. A DC discharge consists of a pair of parallel plates with one plate biased to a large voltage $(\cong 1kV)$ relative to the other. The large voltage, which accelerates the electrons, is the plasma's only power source. Now because the electron temperature is a very strong function of the source geometry, there is no intrinsic advantage in an ECR source as compared to a DC discharge source for obtaining large electron temperatures. However, the electron density is dependent on the ratio of the power absorbed to the energy of the ions leaving the source. For a DC discharge, the energy of the departing ions is dependent on the DC bias, which happens to be the source

of power for the plasma. Therefore as the absorbed power increases so does the ion energy at the plasma boundary, which prevents the increase of the electron density. An ECR source has the microwave power as its principle power source, which allows for independent control of the ion energy at the boundaries and the electron density. This independent control is crucial for applications that simultaneously require precise ion energies and high process rates such as the deposition and etching of metal and dielectric in the metallization process.

The ECR source's ability to create a high temperature, high density plasma does not necessarily render it useful for metallization. High process rates are important but useless if the process itself can not be achieved. The metallization application explored in this work is the filling of sub-micron, high aspect-ratio features with metal. Therefore, the main criterion for an ECR source is its ability to provide the conditions that will result in the filling of these features. Before the ECR source's capabilities can be assessed, the physics that will lead to a successful fill must be understood and the following questions answered:

1) What is meant by a successful fill?

2) Do the conditions that lead to a successful fill exist in an ECR sputter source?

3) If the conditions do exist, then what are the properties required of a plasma source that will enable it to operate within a process window that will yield these conditions?

The first question can be answered by the illustration in figure 1.0-4:

FIGURE 1.0-4:
CR0SS-SECTION OF A
METAL TRENCH

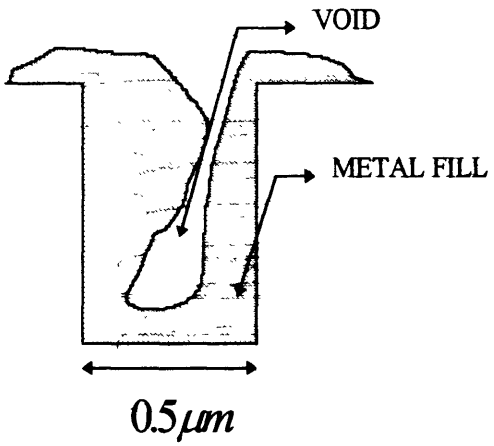

A successful fill has no visible voids; voids degrade the metal line's conductivity as well as enhance electro-migration (the diffusion of atoms resulting from the presence of electric fields), which redistributes the atoms in the metal lines creating more voids. A successful fill also requires that there be no damage to the dielectric surrounding the metal trench from the sputtering that can result from the incident energetic ions.

The answer to the second question was not known at the time for copper metallization of trenches with widths of less than $0.5\mu m$ and aspect ratios greater than 2. It was hypothesized that multiple particle reflections within the trench are necessary for filling geometrically complicated structures. In fact, there are a few other criteria that were believed to be fundamental to the evolution of a successful fill, and they will be discussed in the later sections.

The surface conditions influencing the evolution of the fill were believed to be functions of a few plasma parameters at the surface such as

a) the ratio of the copper neutrals to the copper ions incident on the trench

b) the ratio of the copper ions to the argon ions incident on the trench

c) the energy and angular distribution of the incident flux for each species:

    1) metal ions

    2) metal neutrals

    3) gas ions

    4) gas neutrals : gas neutrals would play a role in the fill evolution

        a) if the gas neutrals possess enough energy to sputter the deposited copper (possible if there is a significant energy exchange between the ions and the neutrals) ; for our plasma, the neutral gas energy is $sub-eV$, well below the sputtering threshold of $\approx 30eV$

        b) if the mean-free path for collisions is of the order of the trench size ($1\mu m$), which is not the case for our plasma

$$\left(\mathrm{Pr}_{gas} \approx 1mtorr \Rightarrow \lambda_{mfp} \approx 5cm\right).$$

These plasma surface parameters are themselves determined by the source geometry, the substrate bias, the method for igniting the plasma (ECR, DC discharge, Inductively coupled plasmas (ICP), helicons,....), and the plasma bulk properties (such as electron temperature and density profiles), which are also partly a function of the source geometry and the method of ignition. Once the method of ignition and the geometry of the source have been established, the remaining variables that can alter the plasma

properties are the process parameters such as gas pressure and microwave power, and the magnetic flux profile (which is controlled by the electromagnet currents) . A thorough understanding of the metallization process requires coupling together

A) a model that describes the particle-surface interactions, and particle diffusion at the surface

B) a model that relates the plasma surface parameters to the plasma bulk parameters

C) a model that describes the influence of the process parameters, the source geometry, and the method of power absorption on the plasma bulk parameters.

1.1: PHYSICS OF METALLIZATION:

Before an attempt is made to understand in detail the plasma physics and its relation to the fill evolution, an understanding of the plasma surface interactions is needed.

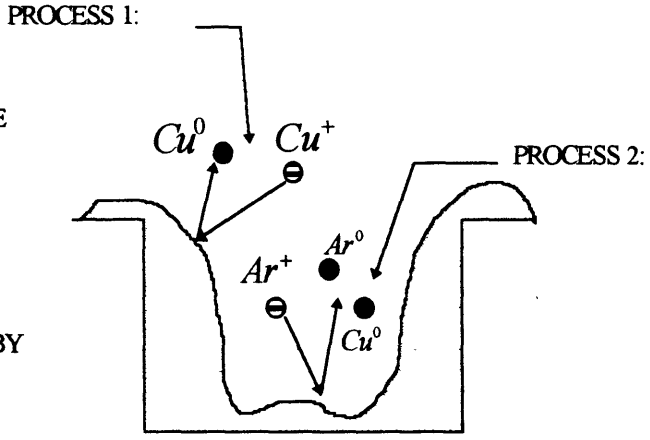

FIGURE 1.1-1:
POSSIBLE INTERACTIONS OF THE INCIDENT PARTICLES WITH THE METAL SURFACE

1. REFLECTION OF THE INCIDENT COPPER ATOMS AND IONS.
2. SPUTTERING OF THE DEPOSITED COPPER BY COPPER AND ARGON IONS

As shown in figure 1.1-1, the incident particles can have a few possible interactions with the surface:

A) the particle can be reflected (either upon impact or after diffusion along the surface)

B) the particle can "stick" to the surface via physio-sorption (physical incorporation of the atom into the surface lattice) or via chemi-sorption (chemical interaction with the surface atoms)

C) the particle can sputter other surface atoms (the ejection of the surface atoms via the energy gained from the incident particle)

The physics of sputtering, reflection, and surface diffusion is quite complicated and not completely understood, and although the understanding is crucial for obtaining the preferential interactions that will lead to a successful fill, it is not needed for a discussion about the reasons for the preferences. So exactly what are the preferred interactions?

Clearly, to fill a trench, the pathway to the bottom of the trench can not be obstructed; therefore, accumulation on the trench corners, which will eventually close the trench entrance (shown in figure1.1-2), leaving a void inside (the phenomenon known as pinch-off), must be avoided.

FIGURE1.1-2: A SCHEMATIC OF THE EVOLUTION OF A 'PINCH-OFF',RESULTING FROM CORNER DEPOSITION
T1<T2<T3

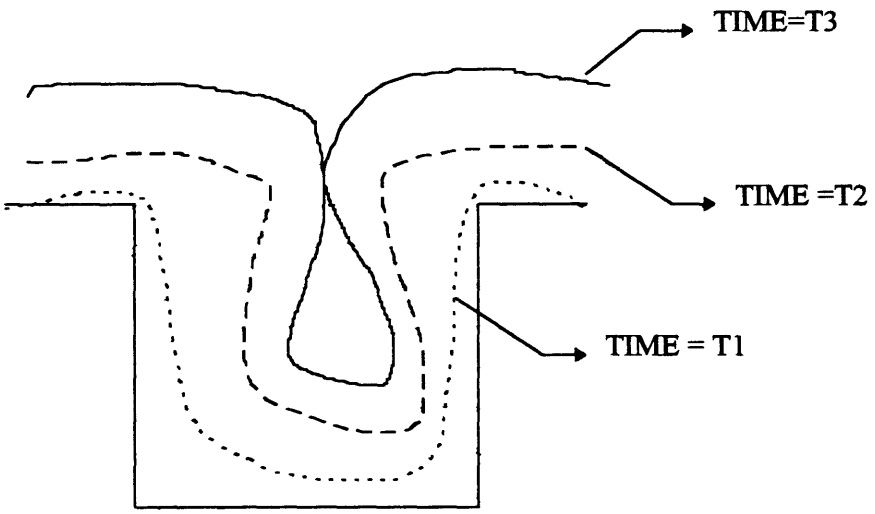

To avoid deposition on the corners,

A) the impinging metal flux must be directed normal to the surface [non-directionality will lead to an impending metal flux at the top of the side-walls (the corners).

B) if there is an impinging metal flux at the corners, the interaction of the metal atoms with the surface must lead to a large probability of reflection (a large reflection coefficient is equivalent to a small sticking coefficient); if the oncoming metal particles have a small probability of sticking at the corners, the accumulation at the corners will be little.

C) if the metal flux does arrive to the corners and sticks upon impact, then it must be removed via sputtering by subsequent particles.

To obtain these preferred interactions through control of the process parameters requires knowledge of the plasma surface parameters as well as the physics of the surface interactions (which as mentioned before is not well understood). Because the theories are not adequately established , the route to understanding the surface interactions has become purely experimental with some aid from numerical simulations (note that the simulations are as accurate as the physics on which they are based; the physics of the surface interactions are controlled by a few microscopic parameters such as the differential sputtering coefficient, coefficients that must be determined **experimentally**).

The experimental approach at the beginning had been based on trial and error: the ECR sputter source (figure 1.0-3) would be run at various process conditions:

a) microwave power : 2 to 5 kW

b) argon pressure : 0.5 to 3 *mtorr*

c) target: aluminum, copper

d) target voltage : 500V to 1200V

e) electromagnet currents (top/bottom): 150A/150A to 230A/180A,

f) substrate bias : no bias $\Rightarrow$ 'floating' ; DC (direct current) bias; RF (radio-frequency) $\Rightarrow$ AC (alternating current) bias; pulsed-DC $\equiv$ RF-bias with 'shaping'

and the fill profiles for the different run conditions would be examined. The experiments that employed the different substrate biasing techniques and the biasing techniques themselves will be discussed later; **for now, the discussion will concentrate on the experiments that employed no substrate bias (substrate floating). We will also limit**

our discussion to the deposition of copper (copper target) only. The results for the aluminum and copper deposition were quite similar; however, there are differences in the properties of copper and aluminum films that influence the success of filling sub-micron features (through their control of surface diffusion, surface tension, and relative etch rates from the side and the bottom of the trench) such as sputtering yields (greater for copper) and melting temperature (greater for aluminum). The fill profiles were examined both qualitatively and quantitatively. The quantitative observations were made as follows: the fill of features with a height of $(h = 1.2\mu m)$ and varying aspect ratios $[A \equiv (h/w)]$, $1/2 \le A \le 4$, was characterized by two parameters, illustrated in figure 1.1-3:

FIGURE 1.1-3:
CHARACTERIZATION OF THE TRENCH

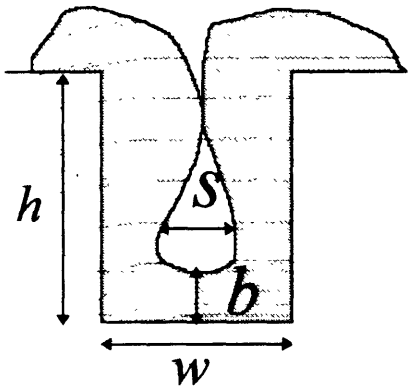

's' IS TAKEN TO BE THE 'MEAN' WIDTH OF THE VOID

'b' IS THE DISTANCE FROM THE BOTTOM OF THE TRENCH TO THE BOTTOM OF THE VOID

a) percent fill (also known as bottom coverage) $B \equiv 100\%\left(\frac{b}{h}\right)$

b) side-wall coverage $S \equiv 100\%\left(\frac{w-s}{w}\right)$

(a successful fill requires that both of the quantities S and $B = 100\%$).

Unfortunately, the results of measuring these two parameters for the different process conditions were quite discouraging.

FIGURE 1.1-4: VARIATION OF THE FILL QUALITY WITH PRESSURE AND POWER

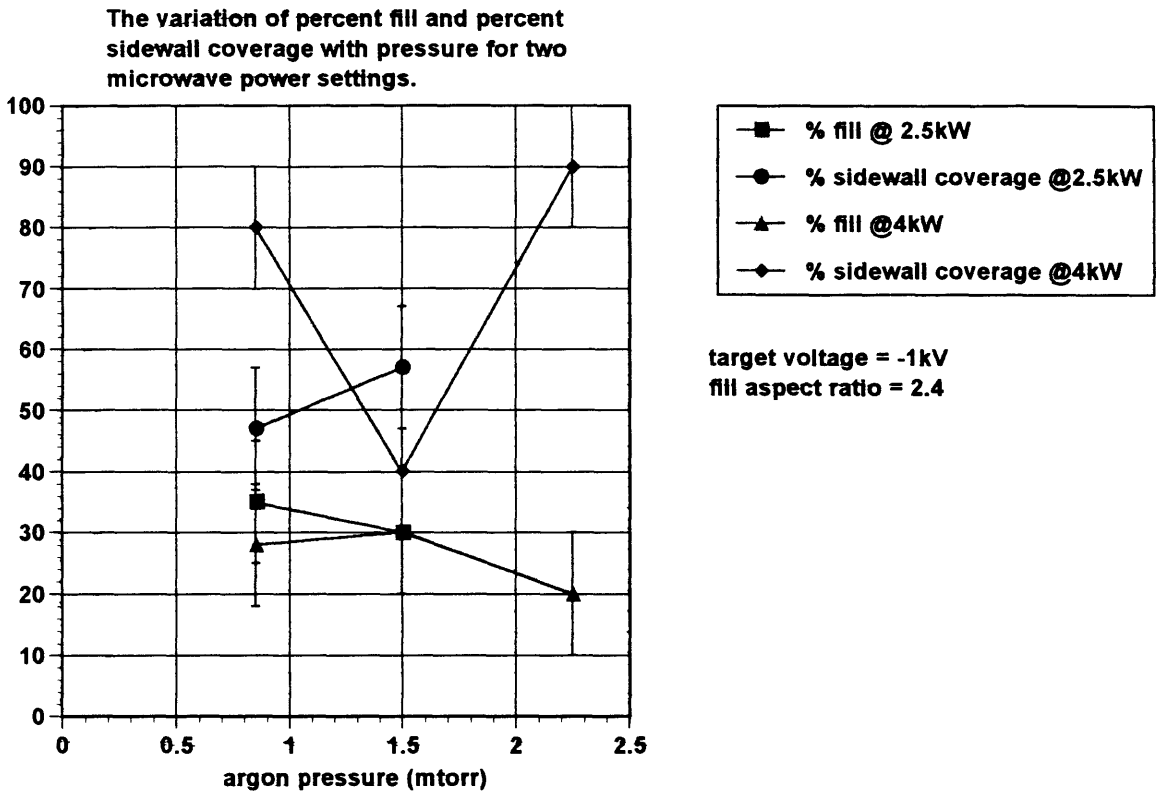

As illustrated in figure 1.1-4, no successful fills were observed for an aspect ratio $(A = 2.4)$, in fact, no successful fills were observed for $(A \geq 2.4)$. Furthermore, no correlation of the fill quality with the process parameters (power, pressure, and magnet current) was found.

This discouraging result served as motivation to understand the influence of the process parameters on the plasma bulk parameters such as:

a) T_e : the electron temperature

b) T_{Cu^+} : the copper ion temperature

c) $n_{Cu^0}, n_{Cu^+}, n_{Ar^+}, n_{Ar^0}$: the copper and the argon ,(neutral and ion), bulk densities

d) η_{Cu^+}, η_{Cu^0}; the transport efficiency of the copper ions and neutrals from the target to the substrate, defined as $\eta_{Cu^j} \equiv \frac{\Gamma_{Cu^j}}{\Gamma_{target}}$, where

1) 'j' corresponds to neutral or ion

2) Γ_{Cu^j} denotes the neutral or ion copper flux at the **substrate**

3) $$\Gamma_{target} = \left[S_{Cu/Cu} f^{target}_{Cu^+/Ar^+} + S_{Cu/Ar}(1 - f^{target}_{Cu^+/Ar^+}) \right] \left(\frac{I_{Cu^+} + I_{Ar^+}}{eA_{target}} \right)$$

$$I_{target} = (1 + \gamma^{Cu}_{se}) I_{Cu^+} + (1 + \gamma^{Ar}_{se}) I_{Ar^+}$$

is the copper flux leaving the target, where

I. I_{target} is the target current

II. A_{target} is the target area

III. e is the electron charge

IV. $S_{Cu/Cu}, S_{Cu/Ar}$ denotes the sputtering coefficient of copper by copper and of copper by argon at normal incidence

V. $f^{target}_{Cu^+/Ar^+}$ is the fraction of the ion flux to the target that is copper

VI. $\gamma^{Cu}_{se}, \gamma^{Ar}_{se}$ are the secondary electron emission coefficients for the incident copper and argon ions respectively

e) magnetic flux geometry and magnetic field strength

and their effect on the plasma surface parameters because, after all, these are the parameters that ultimately influence the fill. These plasma surface parameters are:

a) $\left\langle \theta_{Cu}^{inc} \right\rangle$: the average angle of incidence of the copper flux

b) $\left\langle E_{Ar^+}^{inc} \right\rangle, \left\langle E_{Cu^+}^{inc} \right\rangle$: the average incident energy of the argon and copper ions

c) f_{Cu^+/Ar^+}^{sub} : (the copper-to-argon ion flux fraction at the substrate):

$$\equiv \frac{\Gamma_{Cu^+}}{\Gamma_{Cu^+} + \Gamma_{Ar^+}}$$

d) f_{Cu^+/Cu^0}^{sub} : (the copper ion-to-neutral flux fraction at the substrate):

$$\equiv \frac{\Gamma_{Cu^+}}{\Gamma_{Cu^+} + \Gamma_{Cu^0}} .$$

There are a few other plasma surface parameters ,which are equally influential in influencing the fill evolution: they are

d) $f_E(E)$:the energy distribution function (EDF) of the copper ions, argon ions, and copper neutrals

e) $\left(dS/dEd\Omega\right)_{Ar/Cu}, \left(dS/dEd\Omega\right)_{Cu/Cu}$: (the double differential sputtering cross-sections for argon on copper and for copper on copper) defined such that $\left(\frac{dS}{dEd\Omega}\right)dEd\Omega$ is equal to the ratio of

1) the number of particles leaving the surface with energy between E and $E + dE$ and with angle between (θ, ϕ) and $(\theta + d\theta, \phi + d\phi)$ with respect to the surface normal

2) to the number of particles incident with energy E_{inc} and angle $(\theta_{inc}, \phi_{inc})$ with respect to the surface normal

f) $T_{surface}$: the metal surface temperature.

Obtaining information about the latter plasma surface parameters (d,e,f) is essential in the detailed understanding of the fill evolution; but as can be expected, these parameters are extremely difficult to diagnose.

The motivation for obtaining measurements of the first three above mentioned plasma surface parameters requires an understanding of the influence of these parameters on the fill evolution. As previously mentioned, deposition on the corners must be avoided to fill a trench. As illustrated in figure 1.1-5, deposition on the corners can occur via

a) direct deposition by incident metal flux

b) indirect deposition from sputtered metal from the bottom and the side of the trench

FIGURE 1.1-5: AN ILLUSTRATION OF THE DIFFERENT DEPOSITION MECHANISMS.

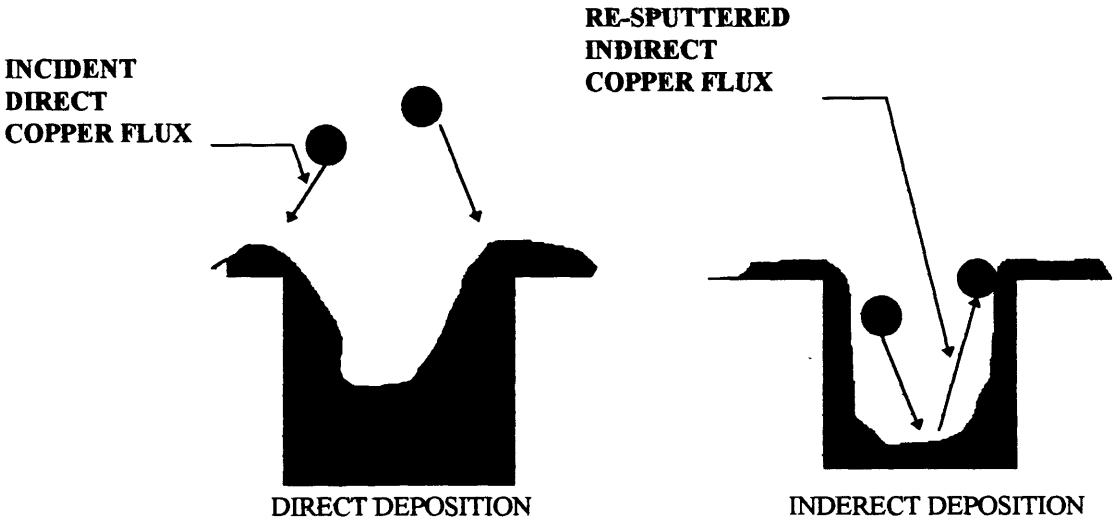

How do the first four plasma surface parameters influence corner deposition?

1) $\langle \theta_{Cu}^{inc} \rangle$: **directionality of the copper metal flux**

FIGURE 1.1-6: THE IMPORTANCE OF DIRECTIONALITY

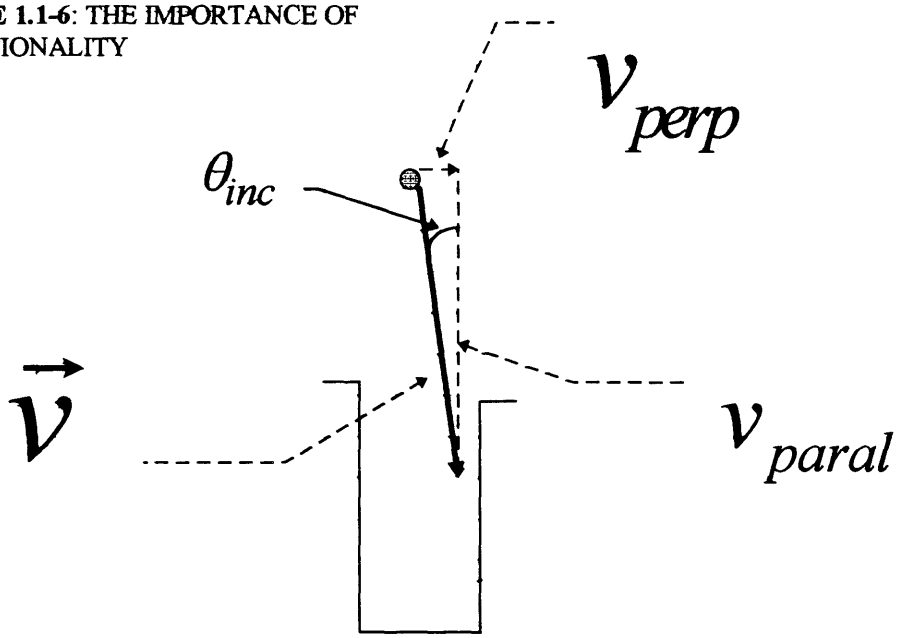

The directionality of the copper metal flux determines direct corner deposition. As illustrated in figure1.1-6, a highly directional flux is required to avoid corner deposition.

2) : $\langle E_{Ar}^{inc} \rangle, \langle E_{Cu}^{inc} \rangle$ **the average incident energy of the copper and argon particles (ions and neutrals)**

The incident energy of the particles influences the indirect corner deposition via the sputtering of the deposited copper from the trench bottom (or from reflection off the trench bottom). The sputtered (or reflected) copper particle can subsequently redeposit on the trench corner . The incident energy of the particle also influences the direct removal of any deposition at the trench corners.

3) f_{Cu^+/Ar^+}^{sub} **: (the copper-to-argon ion fraction at the substrate):**

$$\equiv \frac{\Gamma_{Cu^+}}{\Gamma_{Cu^+} + \Gamma_{Ar^+}}$$

The copper-to argon ion fraction becomes an influential parameter once surface biasing techniques are employed. If the substrate is floating, the maximum energy of the ions striking the surface, which will be demonstrated in a following calculation, is about $30eV$. The sputtering threshold for argon and copper ions striking a copper surface is also about $30eV$; therefore, for the experiments performed with a floating substrate, neither the argon nor the copper ions contribute significantly to indirect deposition at the corners via the sputtering of the deposited copper from the trench bottom (or to direct removal of the deposited copper at the corners via sputtering). Furthermore, the mean-free path for the argon-copper elastic collisions is, as stated previously, about $5cm$, which is much greater than the trench size of $1\mu m$; hence, the expected number of scattering collisions of the directed copper flux (to the trench bottom) near the trench, which could lead to an increase in the direct copper deposition at the corners, is negligible. However, once the surface is biased to increase the directionality of the impinging ion flux, the incident ion energy increases above the sputtering threshold, thereby increasing the contribution to the indirect corner deposition from the re-sputtered copper flux from the trench bottom as well as direct removal via sputtering at the corners; (note from figure1.1-6, that the angle of incidence $\theta_{inc} = \left[\frac{\pi}{2} - a\tan\left(\frac{v_{paral}}{v_{perp}}\right)\right]$, and by biasing the surface negative with respect to the ground voltage,

$$e\left(V_p - V_{surface}\right) = e\left[(V_p - V_f) + (V_f - V_{ground}) + (V_{ground} - V_{surface})\right]$$

and as will be shown in the discussion about the influence of the electron temperature:

$$\frac{v_{paral}}{v_{perp}} \approx \sqrt{\frac{30eV + eV_{gs}}{5eV}}$$

where $V_{gs} \equiv V_{ground} - V_{surface} > 0$, $V_f - V_{ground} \approx 0$, and the $30eV$ essentially comes from $V_p - V_f \cong 3T_e$ (see section 1.2). Therefore, the result of the bias is an increase in $\frac{v_{paral}}{v_{perp}} \Rightarrow$ an increase in the directionality of the incident flux). Hence, there is a compromise between increasing the copper ion energy to increase the directionality of the incident flux (to avoid **direct** corner deposition) and decreasing the argon and copper ion incident energy at the trench bottom (to avoid **indirect** corner deposition from the re-sputtered copper flux from the trench bottom). Of course there is also, as previously stated, direct sputtering at the corners as well, which aids in the removal of corner deposition; however, the flux of atoms sputtered from the corners is preferentially directed towards the opposite side, thereby reducing the benefit of corner sputtering. To minimize the indirect corner deposition while attempting to increase the incident copper ion directionality via substrate biasing, f_{Cu^+/Ar^+} must be maximized. Of course, even if $f_{Cu^+/Ar^+} = 1$, increasing the substrate bias (to obtain directionality) will still result in

indirect corner deposition from the re-sputtered copper flux from the trench bottom, sputtered by the energetic incident copper ion flux.

4) f_{Cu^+/Cu^0} **: (the copper ion-to-neutral fraction):** $\equiv \frac{\Gamma_{Cu^+}}{\Gamma_{Cu^+} + \Gamma_{Cu^0}}$

So far, we have been talking about the directionality of the copper ion flux and have said nothing about the influence of the impinging copper neutral flux. In fact, if most of the copper flux is neutral, the voltage drop across the sheath will be ineffective in enhancing the directionality or controlling the energy of the incoming copper particles. Hence, to reap the benefit of using a plasma, (the natural potential drop that is created across the sheath), f_{Cu^+/Cu^0} must be maximized.

Before proceeding with our discussion, it is worth noting the logic behind it. Remember that we only have control over what we have called the process parameters (gas pressure, microwave power,...); and to understand the influence of these parameters on the fill quality, we need to understand the hierarchy of influence:

process parameters $\Rightarrow$ **plasma bulk parameters** $\Rightarrow$ **plasma surface parameters**

Now that we have some understanding of the influence of the four plasma surface parameters on the fill quality, we will investigate the bulk plasma parameters influence on these surface parameters.

1.2: THE INFLUENCE OF THE ELECTRON AND ION TEMPERATURES

T_e, T_{Cu^+} : the electron and ion temperatures

The global model presented demonstrates that T_e is virtually independent of the input power and very sensitive to the process gas, the gas pressure, and the source geometry. For our source with a plasma volume of $0.03m^3$ and argon gas pressure of $1mtorr$, a typical electron temperature is of order $5eV$. As previously described, the electron temperature and the electron energy distribution function indirectly control the ion energy gained (normal to the surface) through the sheath by determining $\left(V_p - V_f\right)$, the potential difference between the plasma and the floating surface. Of course if the surface is electrically biased the contribution of the bias to the ion energy will have to be considered.

Before discussing the ramification of the electron temperature's influence on the incident ion energy, one peculiarity of the $V_p - V_f$ in our plasma should be noted: As previously stated, for a Maxwellian electron energy distribution in an argon plasma, $V_p - V_f$ is approximately $5T_e$; however, for our plasma the observed $V_p - V_f$ is about $3T_e$. The discrepancy is the result of the assumption of a Maxwellian electron energy distribution. For weakly ionized plasmas, ($n_i \approx n_e << n_g$; for our plasma $\frac{n_e}{n_g} \approx 10\%$), the high-energy tail of the electron distribution function is depleted because the electrons in this energy range have a larger probability of having excitation and ionization collisions (because these interactions have energy thresholds) with the background gas atoms; these excitation and ionization collisions are the dominant energy loss channels for the electron

population as compared to electron-neutral elastic collisions, which have a reduced efficiency for energy exchange of order the mass ratio of the electron to the gas atom $\frac{m_e}{m_g} << 1$. Because of the depletion of the more energetic electrons, the requirement on the retarding potential hill for the electrons $(V_p - V_f)$, which is created to balance the electron and ion flux to the plasma boundaries, is less; hence, $V_p - V_f$ is less than the predicted value assuming a Maxwellian distribution (which has electrons in the high-energy tail).

This potential difference between the plasma and the surface accelerates the incident ions normal to the surface. To estimate the average angle (with respect to the surface normal) with which the ions impinge on the surface, we need an estimate of the ion energy (parallel and perpendicular to the surface normal) prior to its acceleration through the sheath. The metal ions originate at the metal target from which they are sputtered as neutrals that subsequently ionize. The sputtered metal distribution[1] is shown in figure 1.2-1:

[1] H. Oechsner, Appl. Phys. **8**, pp.185-198 (1975)

FIGURE 1.2-1: THE ENERGY DISTRIBUTION OF SPUTTERED PARTICLES

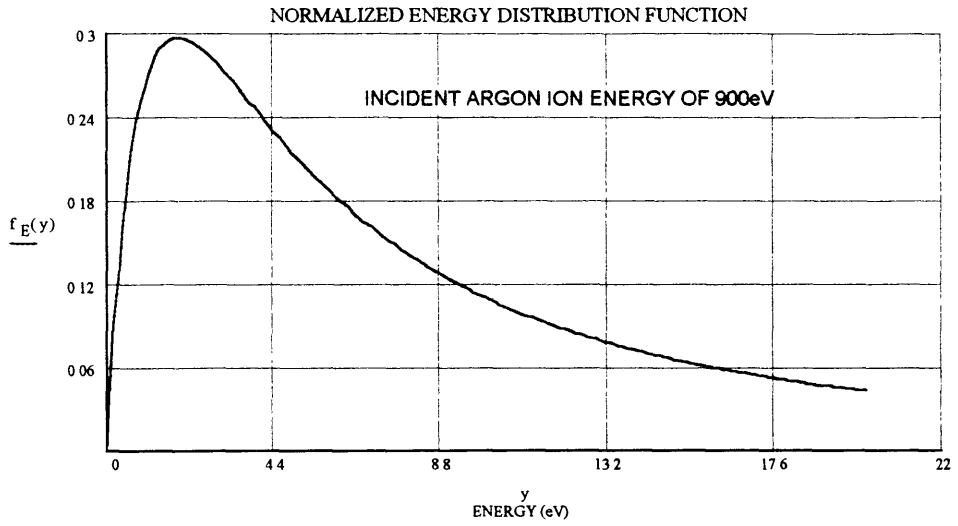

This distribution has a high-energy tail and an average energy of $\approx 3.7eV$. The dominant energy loss channel for the sputtered metal atoms is the collision energy loss with the gas atoms $\left(m_{metal} \approx m_{gas} \Rightarrow \overline{\Delta E}/collision \approx \frac{1}{2}E\right)$. The mean free path for collisions with the background neutral gas (gas pressure of $1mtorr$) is of order $5cm$ and the target to substrate distance is approximately $10'' \approx 25cm$; therefore, the sputtered metal atoms will experience about five elastic collisions before they reach the substrate, which reduces their initial average energy of $3.7eV$ to sub-eV levels, characteristic of the ion temperature in our plasma $T_{ion} \leq 1eV$. Now, once the metal atom is ionized on its path to the substrate, $\left(E_{metal} \approx 3eV; n_e \approx 10^{12} cm^{-3}; T_e \approx 5eV \Rightarrow \lambda_{ionization} \approx 2cm\right)$, the metal ion can gain energy from established electric fields within the plasma and also experience coulomb collisions with the background gas ions and electrons (the long range

of the coulomb interactions render the energy loss from the coulomb collisions with the gas ions comparable to the energy loss from the collisions with the gas atoms , even though the gas atom density is ten times the gas ion density : $\frac{\nu_{i/n}}{\nu_{i/i}} \approx 1$,where ν is the collision frequency for energy loss $\approx$ the collision frequency for momentum loss). Such energy gain from established electric fields in the plasma occurs within the pre-sheath. The pre-sheath will accelerate the ion's parallel velocity to the speed at the sheath, $U \equiv \left(\left(T_e + (1/2)T_{ion}\right)/m_i\right)^{1/2}$, the ion sound speed. Now, the pre-sheath thickness can be of order or greater than a collision length; therefore, a fraction of the ion's parallel energy gain through the pre-sheath can be transferred to its perpendicular energy via collisions with the background gas atoms. Hence, the ion perpendicular energy at the sheath can be of the same order as its parallel energy: $\frac{T_e + (1/2)T_{ion}}{2}$, which is considerably greater than the initial ion energy $\approx T_{ion}$. For a collision-less sheath, (which is typical of the sheaths in our plasma: the sheath thickness for $T_e \approx 5eV$ and $n_e \approx 10^{12}/cm^3$ is of order $20\mu m$ and with bias it could grow to $\approx 100\mu m$, which is still much less than the collision mean-free-path of $5cm$), the perpendicular energy of the ions traversing the sheath will remain the same, and the parallel energy will increase approximately by

$$e\left(V_{sheath} - V_f\right) \approx 2.5T_e \approx 25eV$$, where

$$V_{sheath} \cong V_p - (1/2)T_e : [1.2 - 1]$$

Therefore, the ratio of the parallel to the perpendicular energy of the metal ion at the surface is $\frac{E_{paral}}{E_{perp}} \approx \frac{3T_e + \frac{1}{4}T_{ion}}{\frac{1}{2}T_e + \frac{1}{4}T_{ion}} \approx 6$ and the corresponding velocity ratio is $\frac{v_{paral}}{v_{perp}} \approx \sqrt{6} = 2.5$. Looking at figure 1.1-6, we can see that the average angle of incidence of the metal ions with respect to the surface normal is small $\left[\theta_{inc} = \frac{\pi}{2} - a\tan\left(\frac{v_{paral}}{v_{perp}}\right) \approx .38rad = 22^\circ\right]$, which is equivalent to stating that we have some directionality with room for improvement.

There are also electric fields perpendicular to the surface at the trench created by the side-walls, (which we have not included in our calculation of the directionality), but most of the energy gain occurs far from the trench where the electric field is essentially parallel to the surface (the trench height $h \approx 1.2\mu m$ whereas the sheath thickness as previously noted is of the order $20 - 100\mu m$).

In summary, for the case of no substrate bias, the **increase in the electron temperature increases the directionality** of the ion flux, which decreases corner deposition.

From the above analysis, one might conclude that increasing T_e will improve the fill; not necessarily. To obtain a complete picture of T_e's influence on the fill quality, we need to account for T_e's influence on the remaining plasma surface parameters. How does T_e affect f_{Cu^+/Cu^0} and f_{Cu^+/Ar^+} ? An increase in T_e leads to a preferential ionization of the argon neutrals (the ionization energy for argon is about $16eV$ as

compared to $8eV$ for copper). To demonstrate this, we will analyze the reaction rate for ionization[2]:

$$\langle \sigma v \rangle_{ionization} \propto \frac{T_e^{1/2}}{E_{iz}^2} \exp(-\frac{E_{iz}}{T_e}) cm^3/\sec \text{, where}$$

E_{iz} is the ionization energy of the particular atom: ($E_{iz}^{Cu} \cong 8eV, E_{iz}^{Ar} \cong 16eV$)[3]

Now, the ratio of the ionization reactivities for copper and argon is

$$\frac{\langle \sigma v \rangle_{Cu}}{\langle \sigma v \rangle_{Ar}} \propto \exp\left\{-\left(\frac{E_{iz}^{Cu} - E_{iz}^{Ar}}{T_e}\right)\right\} \cong \exp\left(\frac{8eV}{T_e}\right) : [1.2 - 2];$$

therefore, an increase in the electron temperature will result in a greater increase in the ionization of argon relative to the ionization of copper. This preferential ionization of the argon atoms results in the increase of n_{Ar^+} (the argon ion bulk density) relative to n_{Cu^+} (the copper ion bulk density), thereby, decreasing f_{Cu^+/Ar^+} at the substrate, which as discussed results in enhanced corner deposition. **Hence, even though an increase in T_e can enhance the fill quality via the increase in the metal ion flux directionality and the increase in the copper ionization (which will enhance f_{Cu^+/Cu^0} at the substrate), it can also degrade the fill quality via the resulting decrease in f_{Cu^+/Ar^+}.**

[2] NRL Plasma Formulary , p. 54 (1994)

[3] CRC Handbook of Chemistry and Physics, 73^{rd} edition, 10-211 (1992-3)

1.3: THE INFLUENCE OF THE ARGON GAS ATOM DENSITY

n_{Ar}^{0}: the gas (argon) atom density

The discussion about the electron temperature has hopefully illustrated the indirect influence (via changes in other bulk parameters) as well as the direct influence a plasma bulk parameter can have on the fill quality. This indirect influence will also manifest in our discussion of the gas atom density, but first we will discuss its lack of direct influence. There are three reasons for the gas atoms' benign nature with regard to direct influence on the fill evolution:

1. (no *direct* contribution to deposition):argon is an inert gas; therefore, it does not react chemically with the deposited copper
2. (no *direct* contribution to sputtering):the gas atoms gain their energy from the elastic collisions with the ions (they can't be accelerated by electric fields because they are neutral); the ions have energies of at most an eV; therefore, the gas atoms can't gain enough energy to sputter the deposited copper (the energy threshold for sputtering is about $30eV$).
3. (no *direct* contribution to the directionality of the incoming copper flux):our process pressure is of order a *mtorr*, yielding a mean-free-path for copper-argon elastic collisions of order $5cm$, which is much greater than the characteristic dimensions of the sheath$\left(50\mu m\right)$; therefore, scattering of the incoming copper flux within the sheath is negligible.

Does the argon atom density have an indirect influence on the fill quality? Eq.1.0-11 from the energy and particle conservation model shows that the electron temperature is

essentially inversely proportional to the atom density. Of course, the atom density has to include the contribution from the copper atoms as well as the argon gas atoms, but as mentioned before, the copper atom density is about 10% of the argon gas atom density, and the energy loss per electron-copper ion pair created (Ec) is comparable to the Ec for electron-argon ion pair production; therefore, the dominant influence will be from the argon atoms. Hence, a decrease in the argon atom density will result in an increase in the electron temperature ($n_{Ar^0}\downarrow \Rightarrow$ electron-neutral ionization rate will decrease with respect to the rate of loss of electrons to the boundary for a given input power$\Rightarrow T_e \uparrow$ to increase the ionization rate constant). We have already discussed the effect of an increase in T_e on the other plasma bulk parameters and their subsequent influence on the plasma surface parameters: an increase in the copper ion density and an even greater increase in the argon ion density, resulting in the increase of $f^{bulk}_{Cu^+/Cu^0}$ and in the decrease of $f^{bulk}_{Cu^+/Ar^0}$. Now, in our discussion about the electron temperature, we assumed that the modifications in the bulk parameters result in the same modifications in the surface parameters: $f^{bulk}_{Cu^+/Cu^0}\uparrow \Rightarrow f^{sub}_{Cu^+/Cu^0}\uparrow$ and $f^{bulk}_{Cu^+/Ar^+}\downarrow \Rightarrow f^{sub}_{Cu^+/Ar^+}\downarrow$. However, a modification in these plasma surface parameters comprises two events:

1. a modification in $f^{bulk}_{Cu^+/Cu^0}$ and $f^{bulk}_{Cu^+/Ar^+}$
2. the subsequent transport of the copper particles to the substrate (argon is distributed everywhere in the chamber; whereas, the copper is sputtered from the target and needs to be transported to the substrate).

In our discussion about the electron temperature, we did not mention T_e's influence on the transport of the copper particles to the substrate; however, T_e has a subtle influence on the transport as well. The increase in $\langle \sigma v \rangle_{ionization}$ for copper, resulting from the increase in the electron temperature, decreases the mean-free-path of ionization: $\lambda_{mfp}^{iz} \equiv \frac{u_{drift}^{Cu}}{n_e \langle \sigma v \rangle_{ionization}}$, u_{drift}^{Cu} is the drift speed of the copper atoms . The decrease in λ_{mfp}^{iz} not only increases f_{Cu^+/Cu^0}^{bulk}, it also increases the number of copper atoms that are ionized near the target; once ionized, the copper ions are radially confined by the axial magnetic field created by the electromagnets. This 'early' confinement increases the copper ion transport efficiency, η_{Cu^+}; therefore, we not only have a greater copper ionized fraction within the bulk, but we trap a greater number of the copper atoms (via ionization) leaving the target. The enhanced transport efficiency increases f_{Cu^+/Cu^0}^{sub} by complementing the increase in f_{Cu^+/Cu^0}^{bulk}, but it **reduces** the decrease in f_{Cu^+/Ar^+}^{sub}, resulting from the decrease in f_{Cu^+/Ar^+}^{bulk}. Therefore, the increase in the electron temperature forces η_{Cu^+} and f_{Cu^+/Ar^+}^{bulk} to compete in determining the outcome of f_{Cu^+/Ar^+}^{sub}.

To demonstrate the copper ion confinement by the magnetic field, we will compare the radial diffusion of the copper neutrals to the diffusion of the copper ions. The diffusion coefficient is generally defined as the product of the collision frequency with the square of the average step size between collisions: $D \equiv \nu_{collision}(stepsize)^2$, where

$\nu_{collision} \equiv n_{background} \langle \sigma v_{relative} \rangle_{collision}$ is the product of the background atom density with the collision cross-section averaged with the relative velocity of the colliding species over the velocity distribution function of the background species. The copper ions are forced to gyrate in the plane perpendicular to the field lines with a gyro-radius (Larmor radius) equal to the ratio of their perpendicular speed to the gyro-radian-frequency:

$r_{larmor} \equiv \frac{v_{perp}}{\Omega}; v_{perp} = \sqrt{\left(\frac{2E_{perp}^{Cu^+}}{m_{Cu}}\right)}; \Omega \equiv \frac{Ze\|B\|}{m_{Cu}}$, where $\|B\|$ is the magnitude of the magnetic field, $E_{perp}^{Cu^+}$ is the copper energy perpendicular to the magnetic field direction, and $Z = 1$ for singly ionized copper. If the ions are 'magnetized'(which is equivalent to $\frac{\nu_{collision}}{\Omega} << 1$; for argon pressure of $1\,mtorr$, $\|B\| \approx 800 Gauss$ near the target, $E_{perp}^{Cu^+} \approx 1eV$, and $\sigma \cong \pi R_{Ar+Cu}^2 \approx 9*10^{-15} cm^2$: $\frac{\nu_{collision}}{\Omega} \approx \frac{\nu_{perp} n_{Ar} \sigma}{\Omega} \cong 0.4$), then their average step size is this Larmor radius. For the copper neutrals, the average step size is the mean-free-path for collisions with the background argon gas atoms $\lambda_{mfp} \cong \frac{1}{n_{Ar}\sigma}$.

The collision frequency is essentially the same for both the copper neutral and ion. Hence, the ratio of the diffusion coefficients for the copper neutral and ion yields

$$\frac{D_{Cu^+}}{D_{Cu^0}} \equiv \frac{\nu_{Cu^+}\left(r_{larmor}\right)^2}{\nu_{Cu^0}\left(\lambda_{mfp}\right)^2} \approx \frac{\left(r_{larmor}\right)^2}{\left(\lambda_{mfp}\right)^2} = \frac{\left(\nu_{collision}^{Cu^+}\right)^2}{\Omega_{ion}^2} = \left(n_{Ar}\sigma\right)^2 \left(\frac{2E_{Cu^+}^{perp} m_{Cu}}{e^2 B^2}\right) \approx .17:[1.3-1]$$

thereby demonstrating the better confinement of the copper ions.

We have illustrated that a decrease in the argon atom density will increase the electron temperature, and that the increase in T_e will result in an increase in η_{Cu^+}, but we have not addressed the direct influence that the argon density will have on η_{Cu^+} and η_{Cu^0}, the copper ion and neutral transport efficiency. The direct influence of the argon density is manifest in its control of the collision frequency ($\propto n_{Ar}$) and the mean-free-path of collision ($\propto \frac{1}{n_{Ar}}$). As stated above, the radial diffusion of the copper particles is dependent on the collision frequency and the step size between collisions; the decrease in the argon density will have two ramifications:

1. the decrease in the ion diffusion coefficient ($\propto \nu_{collision}$) accommodated by a decrease in the neutral diffusion coefficient ($\propto \lambda_{mfp}$)
2. the increase in the magnetization of the ions (magnetized ions $\equiv \left(\frac{\Omega_{ion}}{\nu_{collision}} >> 1 \right)$: for the ions to be considered 'magnetized', the ratio of the ion cyclotron frequency to the collision frequency needs to be much greater than one; the ion can not be considered magnetized if it can not complete at least one gyro-orbit without experiencing a collision).

Now, remember that ascribing the step size of the ion to be its Larmor radius is only valid if the ion can be considered magnetized; a significant reduction in the ion magnetization ($\frac{\Omega_{ion}}{\nu_{collision}} \leq 1$) will drive the ion step size towards the neutral step size

($\equiv \lambda_{mfp}$), which will render the ratio of the diffusion coefficients equal ($\frac{D_{Cu^+}}{D_{Cu^0}} \to 1$). To obtain a preferential 'filtering' of the neutral copper, we must have:

$$\left[\frac{D_{Cu^+}}{D_{Cu^0}} < 1\right] \Rightarrow \left[\frac{\Omega_{ion}}{\nu_{collision}} > 1\right] \Rightarrow \left[\frac{\sqrt{\left(T_{Cu^+}/eV\right)}\left(n_{Ar}/10^{13}\,cm^{-3}\right)}{\left(\|B\|/kGauss\right)} < 13\right]$$

where we have taken $T_{Cu^0} \approx T_{Cu^+}$;hence, for $T_{Cu^+} \le 1eV$ and $\|B\| \approx 0.5kGauss$,

$n_{Ar} < n_{Ar}^{\max} = 7*10^{13}cm^{-3}$.

The above analysis has not accounted for coulomb collisions of the copper ions with the background argon ions (the coulomb collisions with the background electrons is neglected because the electron-ion momentum transfer is much less efficient by the factor $\sqrt{\frac{m_e}{m_{Cu}}} \approx 3*10^{-3} << 1$; copper ion-ion collisions do not contribute to copper ion diffusion). The addition of the effect of coulomb collisions will decrease the copper ion diffusion in the limit that the copper ion can be considered 'unmagnetized'; but before we account for the ion-ion interactions, we should justify its addition. The justification requires the demonstration that the copper ion-argon ion collision frequency is comparable to the copper ion-argon neutral collision frequency: $\frac{\nu_{collision}^{ion/ion}}{\nu_{collision}^{ion/neutral}} \ge 1$. The ion-ion collision frequency has the same generic formula as the ion-neutral:

$$\nu_{collision}^{Cu^+/Ar^+} \equiv n_{Ar^+}\langle\sigma v\rangle_{coulomb} \cong n_{Ar^+}\sigma_{coulomb}v_T;$$

$$v_T \equiv \sqrt{\frac{T_{ion}}{m_r}};\ m_r \equiv \frac{m_{Cu}m_{Ar}}{m_{Cu}+m_{Ar}}$$

However, the coulomb cross-section is not simply the area of the interacting atoms $\left(\pi R_{Cu+Ar}^2\right)$. The coulomb force extends well over the characteristic size of the atom to about the penetration distance of the electric field in a plasma, which as previously stated is the Debye length : $\lambda_D \equiv \sqrt{\frac{\varepsilon_0 T_e}{e^2 n_e}}$. The coulomb cross-section is equal to the cross-section for a collision that will result in a 90 degree deflection amplified by the coulomb logarithm ($\ln(\Lambda) \approx 10$), which accounts for the accumulation of the small angle collisions that occur at large distances (compared to the characteristic radius of the atom) resulting from the nature of the coulomb force ($\propto \frac{1}{r^2}$). The cross-section for a 90 degree collision is

$$\sigma_{90} \equiv \pi b_{90}^2;$$

where b_{90} is the distance at which the potential energy $\left(\frac{e^2}{4\pi\varepsilon_0 b_{90}}\right)$ of the interacting ions equals their kinetic energy in the center of mass frame $\left(\approx T_{ion}\right)$.

Thus, the coulomb collision frequency becomes:

$$\nu_{collision}^{ion/ion} \cong 4.8*10^{-8}\,\mu^{-1/2}\ln(\Lambda)\left(n_{Ar^+}/cm^{-3}\right)T_{ion}^{-3/2}\ \sec^{-1};\ \text{where}\ \mu \equiv \frac{m_r}{m_{proton}};$$

and noting that the ion-neutral collision frequency is about the same as the neutral-neutral collision frequency, the ratio of the two collision frequencies becomes:

$$\frac{\nu_{collision}^{ion/ion}}{\nu_{collision}^{ion/neutral}} \approx 69\left(\frac{n_{Ar^+}}{n_{Ar^0}}\right)\left(T_{ion}/eV\right)^{-2}:[1.3-2];$$

with $n_{Ar^+} \approx 0.8*10^{12} cm^{-3}, n_{Ar^0} \approx 3*10^{13} cm^{-3}$, and $T_{ion} \equiv T_{Cu^+} \approx T_{Cu^0} \approx 1eV$, the ratio is

$$\frac{\nu_{collision}^{ion/ion}}{\nu_{collision}^{ion/neutral}} \approx 5/3.$$

Therefore, the collision frequency for the copper ions will have to account for the interactions with both the argon neutrals and ions, and the total collision frequency becomes the sum of the two. The increase in the collision frequency for the copper ions further restricts the limit on the argon neutral density

$(n_{Ar^0} \le n_{Ar}^{\max}\left[1-\frac{n_{Ar^+}}{n_{Ar}^{\max}}\frac{\sigma_{coulomb}}{\sigma_{neutral}}\right] \cong 0.2*n_{Ar}^{\max} \approx 1.5*10^{13} cm^{-3})$: the limit that is set to keep the copper ions 'magnetized'. If the copper ion can be considered magnetized, then its step size remains the gyro-radius, but its diffusion coefficient increases because of the increase in the collision frequency. However, for the typical argon pressure of $1mtorr \Rightarrow n_{Ar^0} \cong 3*10^{13} cm^{-3}$, the copper ion can not be considered 'magnetized', and the step size approaches the copper ion mean-free-path $\equiv \frac{v_T}{\nu_{collision}^{ion/ion+ion/neutral}}$. Therefore, the ratio of the copper ion to the copper neutral diffusion coefficient approaches:

$$\frac{D_{Cu^+}}{D_{Cu^0}} \to \frac{\nu_{Cu^+}\left(\lambda_{mfp}^{Cu^+}\right)^2}{\nu_{Cu^0}\left(\lambda_{mfp}^{Cu^0}\right)^2} \approx \frac{\nu_{Cu^0}}{\nu_{Cu^+}}$$

$$\frac{\nu_{Cu^0}}{\nu_{Cu^+}} \equiv \frac{\nu^{neut/neut}}{\nu^{ion/neut}+\nu^{ion/ion}} \cong \frac{1}{\left(1+\frac{\lambda_{mfp}^{ion/ion}}{\lambda_{mfp}^{neut/neut}}\right)} \cong \frac{1}{1+69\left(\frac{n_{Ar^+}}{n_{Ar^0}}\right)\left[T_{ion}/eV\right]^{-2}}$$

For the densities and the ion temperature stated above,

$$\frac{D_{Cu^+}}{D_{Cu^0}} \to \frac{3}{8}$$

A heuristic derivation of the diffusion coefficient that will link the transition from a 'magnetized' ion to an 'unmagnetized' ion is given by solving the copper ion fluid momentum equation for the radial fluid velocity (the axial direction being the direction of the magnetic field), assuming

a) a negligible inertial term (or steady state)

b) 'slow' moving flows $\Rightarrow$ negligible viscosity:

$$\left|\frac{\mu \nabla_{perp}{}^2 u_{perp}}{\nabla_{perp} p}\right| \approx \left(\frac{u_{perp}}{v_{th}^{ion}}\right)\left(\frac{\nu_{collision}^{ion/neutral}}{\omega_{ci}}\right)\left(\frac{\rho_{larmor}^{ion}}{R}\right) \cong \left(\frac{u_{perp}}{v_{th}^{ion}}\right)(0.25)(.1) << 1$$

$$\Rightarrow \left(\frac{u_{perp}}{v_{th}^{ion}}\right) << 50$$

c) negligible radial electric field (good approximation near the chamber center)

d) negligible radial temperature gradient field (good approximation near the chamber center)

e) a velocity distribution function for the ions that is nearly

Maxwellian (true if $\frac{u}{v_{th}^{ion}} << 1$).

With these assumptions, the copper ion momentum fluid equation becomes:

$$\vec{u} \times \vec{B} - T\nabla n + mn\vec{u}\,\nu = 0 \quad [1.3-3];$$

where $\nu \equiv \nu_{Cu^+}$ is the copper ion collision frequency. Of course, to obtain the correct collision frequency, we must first solve for the velocity distribution function using both the

Boltzmann and the Folker-Plank operators to model both the elastic scattering by the argon neutrals and the coulomb interaction with the argon ions; but to simplify the analysis tremendously, we have used the Krook operator (which does not model coulomb collisions) to model the collisions:

$$\left(\frac{\partial f}{\partial t}\right)_{Krook}^{collision} \equiv \nu\left(f_M - f\right); [1.3-4];$$

where f_M denotes a Maxwellian ion distribution.

In deriving the above fluid equation, we have also assumed (to simplify the analysis further) that the collision frequency is independent of the relative speed of the colliding particles (an assumption that is satisfied for ion-neutral collisions at small speeds: $speed << \sqrt{\frac{T_{Cu}}{m_{Cu}}}$). Again, **this derivation is heuristic**, and its purpose is to elucidate qualitatively the variation of the copper ion diffusion coefficient with its degree of magnetization: $\equiv \left(\frac{\Omega}{\nu}\right)$.

The parallel component in the fluid equation (the component along the magnetic field (z)) is uncoupled from the perpendicular components (the azimuthal (θ) and the radial (r)), and we are only concerned with radial diffusion. Therefore, we write the equations for the perpendicular components only:

$$u_\theta = \frac{\Omega}{\nu} u_r$$

$$nu_r = \frac{T/m}{\nu}\frac{\partial n}{\partial r} - \frac{\Omega}{\nu} nu_\theta$$

$$\Rightarrow nu_r \equiv -D\frac{\partial n}{\partial r} = \left(\frac{\nu^2}{\nu^2 + \Omega^2}\frac{T/m}{\nu}\right)\frac{\partial n}{\partial r} : [1.3-5]$$

$$\Rightarrow D_{Cu^+} = \left(\frac{\nu_{Cu^+}^2}{\nu_{Cu^+}^2 + \Omega_{Cu^+}^2}\frac{T_{Cu^+}/m_{Cu}}{\nu_{Cu^+}}\right)$$

where $\Omega_{Cu^+} \equiv \frac{e\|B\|}{m_{Cu}}$ is the copper ion gyro-radian frequency.

For the copper neutrals, the momentum equation reduces to

$$-T\nabla n + mn\vec{u}\nu = 0$$

$$\Rightarrow mu_r \equiv -D\frac{\partial n}{\partial r} = -\left(\frac{T/m}{\nu}\right)\frac{\partial n}{\partial r} : [1.3-6],$$

$$\Rightarrow D_{Cu^0} = \left(\frac{T_{Cu^0}/m_{Cu}}{\nu_{Cu^0}}\right)$$

and the ratio of the two diffusion coefficients becomes

$$\frac{D_{Cu^+}}{D_{Cu^0}} \cong \left(\frac{\nu_{Cu^+}^2}{\nu_{Cu^+}^2 + \Omega_{Cu^+}^2}\frac{\nu_{Cu^0}}{\nu_{Cu^+}}\right).$$

$$\nu_{Cu^+} = \nu_{Cu^0} + \nu_{coulomb}$$

If we write the ratio as a function of the densities and the magnetic field strength, we obtain:

$$\frac{D_{Cu^+}}{D_{Cu^0}} = \left(1 + \left(\frac{\nu_{Cu^0}}{\nu_{Cu^+}}\right)^2\left(162\frac{(\|B\|/kGauss)^2}{\left(n_{Ar^0}/10^{13}\,cm^{-3}\right)^2(T_{Cu}/eV)}\right)\right)^{-1}\left(\frac{\nu_{Cu^0}}{\nu_{Cu^+}}\right) : [1.3-7]$$

$$\frac{\nu_{Cu^0}}{\nu_{Cu^+}} \cong \frac{1}{1+69\left(\frac{n_{Ar^+}}{n_{Ar^0}}\right)\left[T_{ion}/eV\right]^{-2}}$$

where again we have taken $T_{Cu^0} \approx T_{Cu^+}$. The ratio of the diffusion coefficients reveals that a **decrease in the argon atom density** $\left(n_{Ar^0} \downarrow\right)$ **will enhance the radial confinement of the copper ion relative to the confinement of the copper neutral** $\left(\frac{D_{Cu^+}}{D_{Cu^0}} \downarrow\right)$.

Therefore, the argon atom density affects the fill evolution via its direct and indirect influences on the argon ion, the copper ion, and the copper neutral bulk densities and the copper ion and neutral transport efficiencies, which are controlled by the electron temperature (which determines the mean-free-path of ionization of copper as well as the relative ionization rate between the copper and the argon atoms) and the collision frequency (which influences the cross-field diffusion of the copper ion and the copper neutral). In particular, a decrease in the argon density will increase the electron temperature, which

a) increases the ionization rate for both copper and argon (thereby increasing $f^{bulk}_{Cu^+/Cu^0}$),

b) enhances the ionization of the argon atoms relative to the copper atoms (thereby decreasing $f^{bulk}_{Cu^+/Ar^+}$),

c) decreases the mean-free-path of ionization of copper, thereby

1) trapping more of the copper as ions as they are sputtered from the target, which improves η_{Cu^+} ; and

2) ionizing more of the copper before it reaches the substrate, which enhances η_{Cu^+} and lessens η_{Cu^0} .

The decrease in the argon atom density also decreases the copper ion-argon neutral (approximately the same as the copper neutral-argon neutral) collision frequency, decreasing the cross-field diffusion of the copper ion relative to the copper neutral (thereby enhancing η_{Cu^+} relative to η_{Cu^0}).

The arguments above conclude that a decrease in the argon atom density will increase $f^{sub}_{Cu^+/Cu^0}$, but do not determine the change in $f^{sub}_{Cu^+/Ar^+}$ because of the competing effects of the decrease in $f^{bulk}_{Cu^+/Ar^+}$ and the increase in η_{Cu^+} .

1.4: THE INFLUENCE OF THE MAGNETIC GEOMETRY

Magnetic flux geometry and magnetic field strength:

The magnetic field geometry and strength, like the other two plasma parameters, also affects the surface parameters in multiple ways by influencing the location of microwave power absorption, ion radial (cross-field) diffusion, and ion axial (along-field) flow. We will first examine microwave power absorption (much of the following derivations were either influenced by or taken from class notes[1] and Liebermann's book[2]) .

As previously mentioned, one purpose of the axial magnetic field created by the electromagnets is to drive the electron cyclotron motion (the circular orbit of the electrons perpendicular to the direction of the magnetic field) to which the perpendicular component of the microwave electric field couples. How is this cyclotron motion created? We have talked about the cyclotron motion in some detail when we were discussing the ion cross-field diffusion; now we shall discuss its origin: The equation for the motion of a charged particle in a magnetic field is

$$\vec{F} = m\frac{d\vec{v}}{dt} = q\vec{v} \times \vec{B} : [1.4-1] \; ; \; \vec{F} \text{ denotes the force on the particle with charge } q \, .$$

For the electron $q = -e$. By defining $\omega_{ce} \equiv \frac{e\|B\|}{m}$, and breaking the equation of motion into the separate components, we obtain

$$\begin{aligned} \dot{v}_x &= -\omega_{ce} v_y \\ \dot{v}_y &= \omega_{ce} v_x \quad :[1.4-2] \\ \dot{v}_z &= 0 \end{aligned}$$

---

[1] MIT courses 22,601,22.602, 22.611, 22.612

[2] Liebermann and Lichtenberg, Principles of Plasma Discharges and Materials Processing, 1994, Chp. 13

where the dot represents differentiation with respect to time. The equation for the parallel velocity is not very interesting: the parallel velocity remains constant in time. The solution for the perpendicular velocity components is

$$\begin{aligned} v_x &= -v_{perp}\cos(\omega_{ce}t+\varphi) \\ v_y &= v_{perp}\sin(\omega_{ce}t+\varphi) \\ \vec{v}(t=0) &= v_{perp}\left(-\cos(\varphi)\hat{x},\sin(\varphi)\hat{y}\right) \end{aligned} \qquad :[1.4-3]$$

and the electron's perpendicular position as a function of time is given by

$$\begin{aligned} \vec{r}_{perp}(t) &= \vec{r}_g - \rho\left(\sin(\omega_{ce}t+\varphi),\cos(\omega_{ce}t+\varphi)\right) \\ \vec{r}_g &= \left(x(t=o)-\rho\sin(\varphi),y(t=0)-\rho\cos(\varphi)\right) \\ \rho &= \frac{v_{perp}}{\omega_{ce}} \\ \left\|\vec{r}(t)-\vec{r}_g\right\| &= \rho \end{aligned} \qquad :[1.4-4]$$

These equations represent a circular orbit centered at $\vec{r}_g$; a schematic of the electron's orbit is shown in figure 1.4-1:

FIGURE 1.4-1: A SCHEMATIC OF THE ELECTRON CYCLOTRON ORBIT

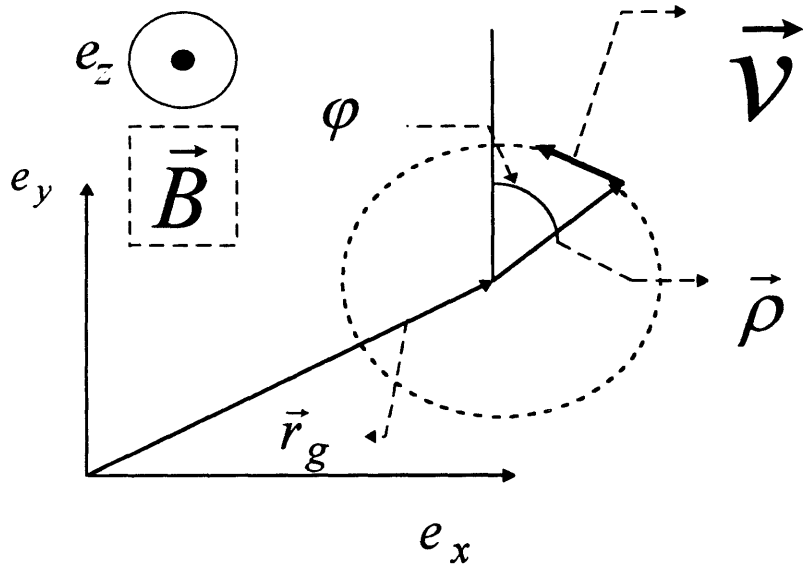

As shown in the schematic, the field is pointing out of the page, and the electron is rotating clock-wise (≡ right hand circular; RH), looking into the direction of the field (out of the page). The particular direction of rotation is the result of the diamagnetic nature of a charged particle: the electron's motion creates a current in the counter-clock-wise direction (again, looking into the direction of the magnetic field), which produces a magnetic field in to the page, which is in the opposite direction of the field that created the motion. The frequency of rotation is the electron cyclotron frequency:

$$f_e = \frac{\omega_{ce}}{2\pi} = \frac{e\|B\|}{2\pi m_e} = 2.8\left(\|B\|/kgauss\right)Ghz$$

Now, to impart energy to the electron, the microwave electric field (in the electron's reference frame) also needs to rotate with the same frequency and in the same direction. To determine the frequency at which the resonance will occur, we need to determine the relationship between the electric field in the lab frame and the field in the electron's reference frame. The problem is in one dimension (the direction parallel to the magnetic field: e_z); therefore, we don't need to account for the electron's perpendicular gyro-motion. We will examine the case of the electric field propagating in the direction of the magnetic field (out of the page); the electric field in the lab frame will have the space and time dependence:

$$E_{wave}(z,t) \propto \exp\left(i\left(k_z z - \omega t\right)\right) = \exp\left(-i\left(\omega t - k_z z\right)\right); [1.4-5];$$

where k_z and ω are the parallel wave number and radian frequency of the wave, respectively. For the wave to be in resonance with the electron, the rate of change of the phase of the field (in the electron's reference frame) must equal to the electron cyclotron radian-frequency:

$$\omega_{ce} \equiv \frac{d}{dt}(\omega t - k_z z) = \omega - k_z \left(\frac{dz}{dt}\right)_{ref.frame}^{electron} :[1.4-6]$$

$$\left(\frac{dz}{dt}\right)_{ref.frame}^{electron} = w_z$$

where w_z is the parallel velocity of the electron. In our experiment, the microwave power source runs at a standard frequency of $f = \frac{\omega}{2\pi} = 2.45Ghz$, and the axial magnetic field varies from a value of 2000 *Gauss* at the target to a field of 400 *Gauss* at the substrate; therefore, we expect the resonance to occur at a position where

$$\omega_{ce}(z) = \frac{eB(z)}{m_e} = \omega - k_z(z) w_z :[1.4-7]$$

If we neglect the electron's parallel motion, then the resonance would occur at a magnetic field of $(0.875kGauss = 875Gauss)$. However, the electron's fluid velocity will shift the location of the resonance region, and a finite electron temperature (which is a measure of the spread in the speed of the electrons about their fluid speed) will impart to the resonance region a finite width. For small drift speeds, the resonance region will then be centered near the field of $875Gauss$ with a spread of order $\pm 50Gauss$ for $T_e \approx 10eV$. The need for a field this large renders the operation of an ECR source expensive because the source requires electromagnets that can produce currents of order $60kA - turns \approx (400amps)(150turns)$.

To understand wave propagation in the plasma once it is launched from behind the target, we will need information about the spatial variation (radial and axial; no azimuthal variation because of the symmetry of the cylindrical geometry) of the radial and the axial components of the magnetic field (the electro-magnets do not produce an azimuthal

component, and we are neglecting the azimuthal field produced by the axial component of the plasma current). Figure1.4-2 shows a typical axial profile for the z-component of the magnetic field at the center of the chamber ($r = 0$)for two different values of the current for the top and bottom electro-magnets. The calculation was done analytically (by taking advantage of the symmetry at $r = 0$) using the Biot-Savart law

$$d\vec{B} = \frac{\mu_0 I}{4\pi} \frac{d\vec{l} \times \vec{R}}{R^3} : [1.4-8];$$

where $d\vec{l}$ is the differential length of the current that is producing the field, and $\vec{R}$ is the vector connecting the position of the differential current element to the position where the field is being calculated.

FIGURE 1.4-2: The field profile resulting from one circular shaped electromagnet situated on top of another both having a thickness of 4 inches, an inner radius of 3 inches, and an outer radius of 6 inches. Z=0 denotes the axial position between the two electromagnets.

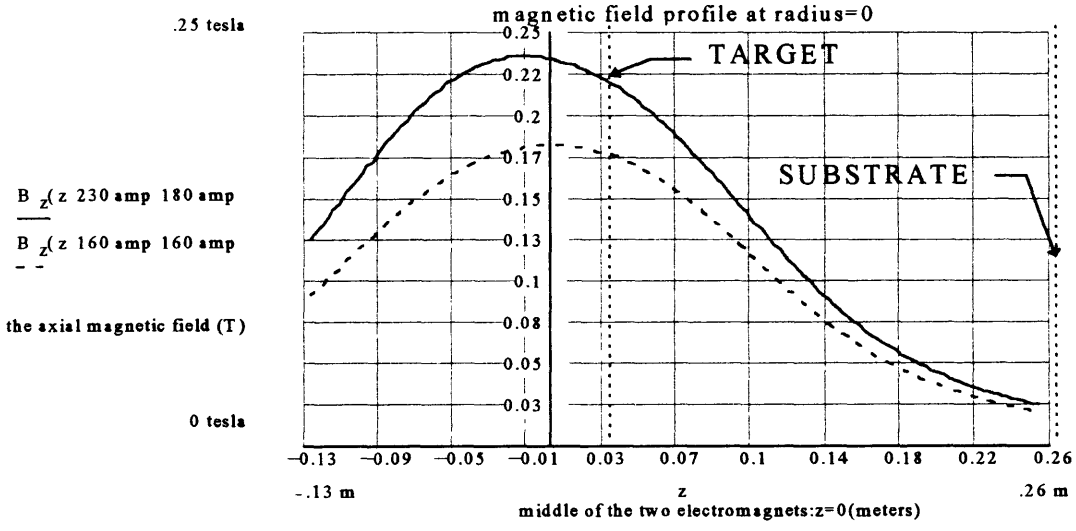

Of course, an axial variation in the z-component of the field will lead to a radial variation in the radial component at finite radial positions ($r \neq 0$), determined through the relation

$$\nabla \cdot \vec{B} = 0 \Rightarrow \frac{1}{r}\frac{\partial}{\partial r}(rB_r) + \frac{\partial}{\partial z}B_z = 0 : [1.4-9]$$

but to simplify the analysis, we will consider a purely axial magnetic with variation in one dimension only: the z-direction. Before, we analyze the wave propagation, we should discuss the characteristics required of the wave's electric field vector to couple to the cyclotron motion of the electrons. Matching the wave frequency with the cyclotron frequency is not the sole requirement for resonance, the electric field vector must have a component with the correct polarization; it must be right hand circularly polarized (RHCP) to rotate in the same direction as the electron in the axial field:

$$\begin{aligned} E_x(z,t) &= \cos(k_z z - \omega t) \\ E_y(z,t) &= -\sin(k_z z - \omega t) \end{aligned} : [1.4-10]$$

To show that this combination of the field components has the correct polarization, we will impose the requirement for resonance on the wave frequency:

$$\begin{aligned} z &= w_z t \\ \omega_{ce} &= \omega - k_z w_z \end{aligned} \Rightarrow \begin{aligned} E_x(z,t) &= \cos(-\omega_{ce} t) = \cos(\omega_{ce} t) \\ E_y(z,t) &= -\sin(-\omega_{ce} t) = \sin(\omega_{ce} t) \end{aligned}$$

FIGURE 1.4-3: Demonstration of the resonance between the clock-wise rotation of the electric field in the electron's reference frame and the perpendicular electron velocity

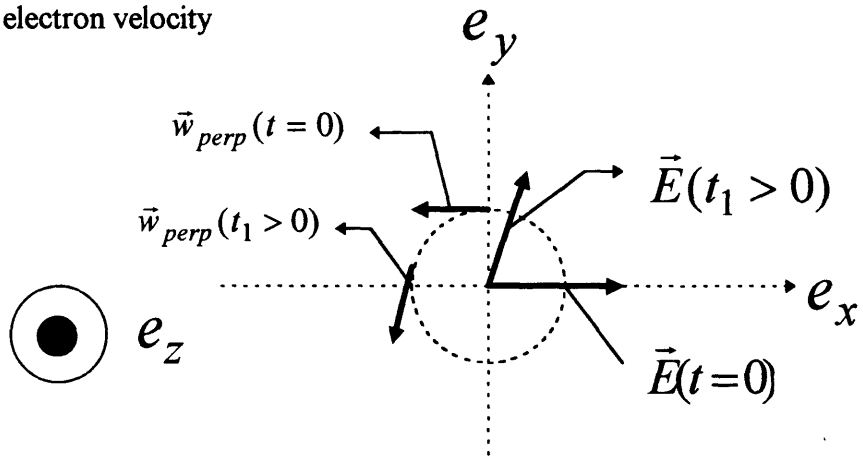

As demonstrated in figure 1.4-3, the field at $t = 0$ in the electron reference frame is in the x-direction, and as time progresses, the field gains a component in the y-direction, thereby demonstrating the clock-wise rotation of the field (looking into the direction of the magnetic field: e_z). It is also useful to examine the complex representation of the electric field of a right hand circularly polarized wave (traveling in the z-direction) because we will be working with the complex form when we analyze wave propagation. The complex representation of the electric field is given by the relation:

$$\tilde{\vec{E}}(k_z,\omega) \equiv \iint \exp\left(-i\left(k_z z-\omega t\right)\right)\vec{E}(z,t)dzdt : [1.4-11]$$

If we define two new unit vectors

$$\begin{aligned} e_R &\equiv \frac{1}{\sqrt{2}}\left(e_x + ie_y\right) \\ e_L &\equiv \frac{1}{\sqrt{2}}\left(e_x - ie_y\right) \end{aligned} : [1.4-12],$$

then

$$\tilde{\vec{E}} = \tilde{E}_x e_x + \tilde{E}_y e_y = \tilde{E}_R e_R + \tilde{E}_L e_L$$
$$\tilde{E}_R = \frac{1}{\sqrt{2}}\left(\tilde{E}_x - i\tilde{E}_y\right) \qquad :[1.4-13].$$
$$\tilde{E}_L = \frac{1}{\sqrt{2}}\left(\tilde{E}_x + i\tilde{E}_y\right)$$

Now, remember that for the wave to interact with the electron, it must be rotating in the same direction as the electron (RHCP). If we observe the form of this wave, we will notice that

$$\dot{E}_x(t) = -\omega E_y(t) \rightarrow -i\omega\tilde{E}_x = -\omega\tilde{E}_y$$

and

$$\begin{matrix}\tilde{E}_R = \sqrt{2}\tilde{E}_x \\ \tilde{E}_L = 0\end{matrix} :[1.4-14].$$

Hence, when we analyze wave propagation, we will only consider the component of the wave that will interact with the electron: $\left(\tilde{E}_R\right)$.

One could argue that the electron can also loose energy to the electric field if the initial velocity of the electron is parallel to the electric field at $t = 0$:

$$\vec{v}\cdot\left[m\frac{d\vec{v}}{dt} \propto -e(\vec{E} + \vec{v}\times\vec{B})\right] \Rightarrow \frac{d}{dt}\left(\frac{1}{2}mv^2\right) = -(\vec{v}\cdot\vec{E})$$
$$\Rightarrow (\vec{v}\cdot\vec{E}) > 0 \rightarrow \frac{d}{dt}\left(\frac{1}{2}mv^2\right) < 0 \qquad :[1.4-15].$$

Therefore, for a distribution of perpendicular velocities that is independent of the initial phase of the electron, relative to the electric field, (phase: $\varphi = \cos^{-1}\left(\hat{v}\cdot\hat{E}\right)$), for example a Maxwellian distribution function (which is a function of the magnitude of the perpendicular velocity only), one would expect that the gain in energy by the electrons that are out of phase ($\cos(\varphi) < 0$) with the electric field will be negated by the loss in

energy by the electrons that are in phase ($\cos(\varphi) > 0$) with the electric field; this expectation is not correct. The gain in energy by the electrons that are out of phase with the field outweighs the loss in energy by the electrons that are in phase with the electric field; hence there is a net energy transfer from the electric field to the electrons. The proof of this net transfer of energy lies in the time evolution of the electron velocity:

$$\begin{aligned} &m\dot{\vec{v}} = -e(\vec{E} + \vec{v} \times \vec{B}) \\ &\vec{E} = \vec{E}_1; \\ &\vec{B} = B_0 e_z + \vec{B}_1(z,t) \quad :[1.4-16]. \\ &\nabla \times \vec{E}_1 = -\frac{\partial}{\partial t}\vec{B}_1 \end{aligned}$$

With

$$\vec{E}_1 = E\left[\cos(k_z z - \omega t)e_x - \sin(k_z z - \omega t)e_y\right]:[1.4-17],$$

a right hand circularly polarized wave. Now, the contribution of the wave's magnetic field relative to its electric field will be of the order

$$\begin{aligned} &\frac{\left\|\vec{v} \times \vec{B}_1\right\|}{\left\|\vec{E}_1\right\|} = \frac{\left\|\vec{v} \times \frac{1}{\omega}\left(k_z \times \vec{E}_1\right)\right\|}{\left\|\vec{E}_1\right\|} \approx \frac{v_{th}}{v_p} \quad :[1.4-18]. \\ &v_p \equiv \frac{\omega}{k_z}; v_{th} \equiv \sqrt{\left(\frac{2T_e}{m_e}\right)} \end{aligned}$$

We will later show that $k_z \approx 4\frac{\omega}{c}$ and increases as $\omega \to \omega_{ce}$, where c is the speed of light; therefore, for $T_e \approx 10eV$, $\frac{v_{th}}{v_p} \approx 4\frac{v_{th}}{c} \approx 0.03 << 1$. Hence, we will ignore the contribution of the wave's magnetic field. With this approximation, the differential equation of motion for the electron becomes

$$\ddot{\vec{v}}_{perp} + \omega_{ce}^2 \vec{v}_{perp} = \left(\frac{\partial}{\partial t} + \omega_{ce} e_z \times \right) \vec{\xi}$$
$$\dot{v}_z = 0 \qquad :[1.4-19].$$
$$\omega_{ce} \equiv \frac{eB_0}{m_e}; \vec{\xi} \equiv \frac{e}{m_e} \vec{E}_1$$

By making a non-relativistic coordinate transformation (which is valid because

$\beta \equiv \frac{v_{th}}{c} << 1$) to move into the electron's reference frame

$$z_{ref} = z - v_z t_{ref}$$
$$t_{ref} = t \qquad :[1.4-20],$$

the electric field in the electron's reference frame becomes

$$\vec{E}_1 = E\left[\cos\left(k_z z_{ref} - \omega_{ref} t\right) e_x - \sin\left(k_z z_{ref} - \omega_{ref} t\right) e_y\right] :[1.4-21]$$
$$\omega_{ref} \equiv \omega - k_z v_z$$

with the electron's axial position denoted by $z_r = 0$. The solution to the differential equation for the perpendicular velocities with the initial conditions

$$v_x(0) = v_0 \cos(\varphi)$$
$$v_y(0) = v_0 \sin(\varphi)$$

is given by

$$v_x(t) = v_0 \cos\left(\omega_{ce} t + \varphi\right) - \frac{2}{\omega_{ref} - \omega_{ce}} \xi \sin\left(\frac{\omega_{ref} - \omega_{ce}}{2} t\right) \cos\left(\frac{\omega_{ref} + \omega_{ce}}{2} t\right)$$
$$v_y(t) = v_0 \sin\left(\omega_{ce} t + \varphi\right) - \frac{2}{\omega_{ref} - \omega_{ce}} \xi \sin\left(\frac{\omega_{ref} - \omega_{ce}}{2} t\right) \sin\left(\frac{\omega_{ref} + \omega_{ce}}{2} t\right) :[1.4-22],$$
$$\xi \equiv \frac{e}{m_e} \left\| \vec{E}_1 \right\|$$

and the perpendicular energy gain is

$$\Delta U_{perp}(t) = \frac{1}{2} m_e \left(v_{perp}^2(t) - v_{perp}^2(0) \right) \Rightarrow$$

$$\frac{2m_e}{\left(\omega_{ref} - \omega_{ce}\right)^2} \xi^2 \sin^2\left(\frac{\omega_{ref} - \omega_{ce}}{2} t\right) - \frac{2m_e}{\left(\omega_{ref} - \omega_{ce}\right)} v_0 \xi \sin\left(\frac{\omega_{ref} - \omega_{ce}}{2} t\right) \cos\left(\frac{\omega_{ref} - \omega_{ce}}{2} t - \varphi\right) : [1.4-23].$$

The electric field in the electron's reference frame was chosen to be initially pointing in the x-direction and φ determines the initial direction of the electron's velocity relative to the electric field. We will consider two cases near resonance:

1. $\varphi = \pi; \Rightarrow \vec{v}_{perp}(0) = -v_0 e_x$; where the initial velocity is anti-parallel to the E-field: **the electron will gain energy**.
2. $\varphi = 0; \Rightarrow \vec{v}_{perp}(0) = v_0 e_x$; where the initial velocity is parallel to the E-field: **the electron will lose energy for a short time such that** $\delta \equiv \frac{4v_0}{t\xi} > 1$. For $\delta < 1$, the electron will gain energy. Why? If the electric field is large or if the electron feels the field for a long time, its velocity will decrease to zero at which point it will begin to gain energy from the field, eventually gaining beyond what it had lost. Of course, the magnitude of the electric field will also be changing with time (because of the energy lost to the electrons($U_{\vec{E}} = \frac{1}{4}\varepsilon_0 \|E\|^2$); therefore the product of $t\xi \rightarrow \int dt\xi(t)$.

If we take the ratio of the change in the energy for the two cases near resonance where $\omega_r \rightarrow \omega_{ce}$, we find that (for the case of $\delta > 1$: a short time)

$$\frac{\left|\Delta U_{perp}^{loss}\right|}{\left|\Delta U_{perp}^{gain}\right|} \cong \frac{\delta - 1}{\delta + 1} < 1 : [1.4-24].$$

Hence, for a velocity distribution function that is independent of the direction of the electron's perpendicular velocity, the term in the equation for the energy change that contains φ will average to zero (over the normalized perpendicular velocity distribution function), and the net result is the transfer of energy from the E-field to the electrons

$$\left\langle \Delta U_{perp}(t) \right\rangle_{perp} \equiv \iint_{w_{perp},\varphi} d\varphi dw_{perp} w_{perp} \hat{f}_{perp}\left(w_{perp}^2\right) \Delta U_{perp}(t)$$

$$= \frac{2m_e}{\left(\omega_{ref} - \omega_{ce}\right)^2} \xi^2 \sin^2\left(\frac{\omega_{ref} - \omega_{ce}}{2} t\right) \geq 0 \qquad :[1.4-25].$$

To obtain the energy gain per unit volume, we must integrate the energy gain over the parallel distribution function:

$$\left(\Delta U/Vol\right) = \int_{-\infty}^{\infty} dw_z f_{paral}\left(w_z\right) \left[\frac{2m_e}{\left(\omega_{ref}\left(w_z\right) - \omega_{ce}\right)^2} \xi^2 \sin^2\left(\frac{\omega_{ref}\left(w_z\right) - \omega_{ce}}{2} t \right) \right] :[1.4-26]$$

$$\omega_{ref}\left(w_z\right) = \omega - k_z w_z$$

which becomes

$$x \equiv \frac{t}{2}\left(\omega - \omega_{ce} - k_z w_z\right)$$

$$\left(\Delta U/Vol\right) = \frac{m_e \xi^2 t}{k_z} \int_{-\infty}^{\infty} dx \frac{\sin^2(x)}{x^2} f_{paral}\left(\frac{\omega - \omega_{ce} - \frac{2x}{t}}{k_z} \right) \Rightarrow :[1.4-27].$$

$$\left(\Delta U/Vol\right) = \frac{m_e \xi^2 t \pi}{k_z} f_{paral}\left(\frac{\omega - \omega_{ce}}{k_z} \right)$$

Hence, absorbed power per unit volume is

$$P/Vol = \frac{m_e \xi^2 \pi}{k_z} f_{paral}\left(\frac{\omega - \omega_{ce}}{k_z} \right) :[1.4-28].$$

$$\xi = e\left\|\vec{E}_{RHCP}\right\|/m_e$$

For a drifting (fluid speed $u \neq 0$) Maxwellian parallel distribution function, the absorbed power density becomes

$$P/Vol = \frac{e^2 \pi^{1/2} n_e}{m_e k_z v_{th}} \left\| \vec{E}_{RHCP} \right\|^2 \exp\left(-\left(\frac{\omega - \omega_{ce} - k_z u}{k_z v_{th}} \right)^2 \right) : [1.4-29].$$

The equation for power absorption demonstrates that the wave's (RHCP) component of the electric field can transfer energy to the electrons near the resonance region where (for a small drift speed)

$$\omega_{ce}(z) = \frac{e}{m_e} B_0(z) \rightarrow \omega = 2\pi f_{microwave}$$
$$f_{microwave} = 2.45GHz$$

Now we must analyze the wave's ability to propagate to the resonance region. As is apparent in figure 1.4-2, the magnetic field does vary significantly in the z-direction; however, because of the large electron mobility along the field lines, no significant gradients in temperature or density are present. To simplify the analysis, we will consider a one dimensional model (spatial variation in the z-direction only) with wave propagation along the magnetic field line ($\vec{k}_{perp} = 0$). We are looking for the solution for the propagation of a RHCP wave with a particular frequency (the frequency of the launched wave: 2.45GHz); hence, the E-M fields have the time dependence

$$\begin{aligned} E(t) &= \mathrm{Re}\left(\tilde{E}(\omega) \exp(-i\omega t) \right) \\ H(t) &= \mathrm{Re}\left(\tilde{H}(\omega) \exp(-i\omega t) \right) \end{aligned} : [1.4-30]$$

with $E_z = H_z = 0$;

With this time dependence, the RHCP component of the electric field becomes

$$\vec{E}_{RHCP}(t) = \mathrm{Re}\left(\left[\frac{1}{\sqrt{2}}\left(\tilde{\vec{E}}_x - i\tilde{\vec{E}}_y\right)\left(\frac{e_x + ie_y}{\sqrt{2}}\right)\right]\exp(-i\omega t)\right);$$

$$\tilde{\vec{E}}_y = i\tilde{\vec{E}}_x = iE_0 \Rightarrow \qquad :[1.4-31]$$

$$\vec{E}_{RHCP}(t) = E_0\,\mathrm{Re}\left(\left(e_x + ie_y\right)\exp(-i\omega t)\right) = E_0\left(\cos(\omega t)e_x + \sin(\omega t)e_y\right)$$

which is what we expected. The governing equations for E-M waves is, of course, Maxwell's equations; with $\frac{\partial}{\partial t}\left(\vec{E}_1, \vec{H}_1\right) \rightarrow -i\omega\left(\tilde{\vec{E}}, \tilde{\vec{H}}\right)$ and $\nabla \rightarrow e_z\frac{\partial}{\partial z}$, and the subscript '1' denoting that the field is a first order quantity (the fields associated with the wave), thereby, much smaller than any stationary established field in the plasma. Maxwell's equations for the first order fields becomes:

$$\begin{aligned}
&\nabla \times \tilde{\vec{E}} = i\omega\tilde{\vec{B}} \\
&\nabla \times \tilde{\vec{H}} = \tilde{\vec{J}}_{free} - i\omega\tilde{\vec{D}} \\
&\tilde{\vec{B}} = \mu_0\tilde{\vec{H}} \\
&\tilde{\vec{D}} = \vec{\vec{\varepsilon}} \cdot \tilde{\vec{E}}
\end{aligned} \qquad :[1.4-32].$$

We are solving Maxwell's equations by using an ordering scheme; therefore, the zero order equations are solved separately. In our treatment, we consider the plasma to be a dielectric with a permitivity (which is usually a tensor) relating the response of the plasma to the wave's time varying electric field (which we have assumed to be linear: this assumption is valid for small perturbations). The 'free' current is associated with a time-varying response of the plasma to an external source (we will analyze the case of no external source: $\tilde{\vec{J}}_{free} = 0$). Combing the two equations to eliminate the magnetic field, we obtain

$$\nabla\times\left(\nabla\times\tilde{\vec{E}}\right)=\nabla\left(\nabla\cdot\tilde{\vec{E}}\right)-\nabla^2\tilde{\vec{E}}=i\omega\nabla\times\tilde{\vec{B}}=\frac{\omega^2}{c^2}\vec{K}\cdot\tilde{\vec{E}}$$
$$\vec{\varepsilon}\equiv\varepsilon_0\vec{K} \qquad :[1.4-33].$$
$$c^2=(\mu_0\varepsilon_0)^{-1}$$

Now, we note that the gradient is only in the z-direction and that the z-component of the electric field is zero; therefore, the divergence term is zero. Hence, the equation reduces to

$$\left(\tilde{\vec{E}}\right)''+k_0^2\vec{K}\cdot\tilde{\vec{E}}=0 \qquad :[1.4-34],$$
$$k_0\equiv\frac{\omega}{c}$$

where the prime denotes differentiation with respect to 'z'. To relate $\vec{K}$ to the plasma quantities, we have to specify our model:

$\tilde{\vec{D}}=\varepsilon_0\tilde{\vec{E}}+\tilde{\vec{P}}$: the displacement vector is a composition of the field's electric field and the polarization vector, which is the response of the medium to the electric field.

$$\tilde{\vec{P}}=\varepsilon_0\vec{\chi}\cdot\tilde{\vec{E}}\Rightarrow$$
$$\tilde{\vec{D}}=\varepsilon_0\left(\vec{I}+\vec{\chi}\right)\cdot\tilde{\vec{E}}\Rightarrow \qquad :[1.4-35],$$
$$\vec{K}\equiv\vec{I}+\vec{\chi}$$

here, we have used the assumption of the linear response.

To determine $\vec{\chi}$, we use the relation

$\tilde{\vec{J}}_{response}=\vec{\sigma}\cdot\tilde{\vec{E}}$:[1.4 – 36]; (where $\vec{\sigma}$ is the plasma conductivity tensor)

together with the second Maxwell's equation (with no 'free' current)

$$\nabla \times \tilde{\tilde{H}} = -i\omega\tilde{\tilde{D}} = -i\omega\varepsilon_0\left(\tilde{\tilde{E}} + \tilde{\tilde{P}}\right) \equiv -i\omega\varepsilon_0\tilde{\tilde{E}} + \tilde{\tilde{J}}_{reponse} \Rightarrow$$

$$\tilde{\tilde{P}} = \frac{\ddot{\sigma}}{-i\omega\varepsilon_0} \cdot \tilde{\tilde{E}} \Rightarrow$$

$$\ddot{\chi} = \frac{\ddot{\sigma}}{-i\omega\varepsilon_0} \Rightarrow \qquad :[1.4-37].$$

$$\ddot{K} = \ddot{I} + \frac{\ddot{\sigma}}{-i\omega\varepsilon_0}$$

Hence, the governing equation for the wave's electric field becomes:

$$\left(\tilde{\tilde{E}}\right)'' - k_0^2\left(\ddot{I} + \frac{\ddot{\sigma}}{-i\omega\varepsilon_0}\right) \cdot \tilde{\tilde{E}} = 0 \qquad :[1.4-38],$$

$$k_0 \equiv \frac{\omega}{c}$$

and the equation for the RHCP and the LHCP components become:

$$\left(\tilde{E}_R\right)'' + k_0^2\left(\tilde{E}_R + \frac{1}{2}\frac{\left[\left(\sigma_{xx}+\sigma_{yy}\right)+i\left(\sigma_{xy}-\sigma_{yx}\right)\right]\tilde{E}_R + \left[\left(\sigma_{xx}-\sigma_{yy}\right)+i\left(\sigma_{xy}+\sigma_{yx}\right)\right]\tilde{E}_L}{-i\omega\varepsilon_0}\right) = 0$$

$$\left(\tilde{E}_L\right)'' + k_0^2\left(\tilde{E}_L + \frac{1}{2}\frac{\left[\left(\sigma_{xx}+\sigma_{yy}\right)-i\left(\sigma_{xy}-\sigma_{yx}\right)\right]\tilde{E}_L + \left[\left(\sigma_{xx}-\sigma_{yy}\right)+i\left(\sigma_{xy}+\sigma_{yx}\right)\right]\tilde{E}_R}{-i\omega\varepsilon_0}\right) = 0 \qquad :[1.4-39].$$

$$\tilde{E}_R = \sqrt{2}\tilde{E}_{RHCP} = \tilde{E}_x - i\tilde{E}_y$$

$$\tilde{E}_L = \sqrt{2}\tilde{E}_{LHCP} = \tilde{E}_x + i\tilde{E}_y$$

To solve for the axial variation of the electric field, we will need information about the plasma conductivity tensor's axial variation. We obtain this information by relating the 'response' current to the plasma species' velocity distribution functions and then relating the species' distribution functions to the electric field:

$\tilde{\tilde{J}}_{response}(\omega,z) \equiv \sum_{species\,i} q_i \int dw \vec{w} \tilde{f}_{1i}(\vec{w},\omega,z)$:[1.4 – 40]; where q_i is the charge of the species 'i' (electron, ion) and $\tilde{f}_{1i}(\vec{w},\omega,z)$ is the first order perturbation to the

velocity distribution function of the particular charged species, the perturbation resulting from its interaction with the wave's E-M field.

To relate the perturbed distribution function to the electric field, we will need to solve the kinetic equation for each species:

$$\frac{\partial}{\partial t} f_i + \vec{w} \cdot \nabla_r f_i + \frac{q_i}{m_i}\left(\vec{E} + \vec{w} \times \vec{B}\right) \cdot \nabla_w f_i = \left(\frac{\partial}{\partial t} f_i\right)_{collision} :[1.4-41].$$

We solve this equation by a perturbation expansion,

$$f \cong f_0 + f_1 + \ldots\ldots :[1.4-42]; \text{ where } \frac{f_1}{f_0} \approx \delta \approx .1 << 1$$

$$\vec{B} = \vec{B}_0 + \vec{B}_1 = B_0 e_z + \vec{B}_1$$
$$\vec{E} = \vec{E}_{1perp} \qquad :[1.4-43]$$
$$E_{1z} = 0$$

$$\nabla \times \vec{E}_1 = -\frac{\partial}{\partial t}\vec{B}_1 :[1.4-44]$$

$$f_0 = f_{Maxwellian}^{drifting}(\vec{w}) = \frac{n}{\pi^{3/2} v_{th}^3} \exp\left(-\frac{\left\|\vec{w} - u e_z\right\|^2}{v_{th}^2}\right) =$$

$$\frac{n}{\pi^{3/2} v_{th}^3} \exp\left(-\frac{w^2 - 2uw_z + u^2}{v_{th}^2}\right) \Rightarrow \qquad :[1.4-45]$$
$$f_0(\vec{w}) = f_0\left(w^2, w_z\right)$$

$$v_{th}^2 = 2v_T^2 = 2\frac{T}{m}$$

solving the equation order by order, which requires an estimate of the magnitude of each term:

$$\frac{\nu_{collision}^{electron}}{\omega} \approx \frac{5 \cdot 10^6 \sec^{-1}}{2\pi(2.45GHz)} \approx 10^{-4} \approx \delta^4 <<< 1; \frac{\nu_{collision}^{ion}}{\omega} \approx 10^{-5} \approx \delta^5 <<< 1$$

$$\frac{\omega_{ce}}{\omega} \approx 1; \frac{\omega_{ci}}{\omega} \approx \frac{m_{electron}}{m_{ion}} \frac{\omega_{ce}}{\omega} \approx 10^{-5} <<< 1$$

$$\frac{\partial}{\partial t} \approx \omega$$

$$\nabla \approx k_z + \frac{1}{L}; k_z \approx \frac{\omega}{v_p} \approx 100 m^{-1}; L \approx .25m$$

$$v_p \equiv \frac{\omega}{k_z} \leq \frac{1}{4}c; v_g \equiv \frac{\partial \omega}{\partial k_z} \leq \frac{1}{2}c$$

$$T_{electron} \approx 10 T_{ion} \approx 10eV$$

$$v_{th}^{electron} \approx 10^6 \, m/\sec; v_{th}^{ion} \approx 10^3 \, m/\sec; \frac{u}{v_{th}} \approx \delta$$

$$\left\| \frac{\partial}{\partial t} \vec{B}_1 \right\| \approx \omega B_1; \left\| \nabla \times \vec{E}_1 \right\| \approx k_z E_1 \Rightarrow B_1 \approx \frac{1}{v_p} E_1$$

$$v_g \frac{\varepsilon_0 E_1^2}{2} \approx \frac{4kW}{100cm^2} \Rightarrow E_1 \approx 8 kV/m$$

$$\left\| \frac{\partial}{\partial t} f_0 \right\| = 0$$

$$\left\| \frac{\partial}{\partial t} f_1 \right\| \approx \omega f_1 \rightarrow \delta^1$$

$$\left\| \vec{w} \cdot \nabla f_0 \right\| = 0$$

$$\left\| \vec{w} \cdot \nabla f_1 \right\| \approx \frac{v_{th}}{L} f_1 + v_{th} k_z f_1 \rightarrow \left(\frac{v_{th}}{L\omega} + \frac{v_{th}}{v_p} \right) \delta^1 \rightarrow \left(\left(\sqrt{\frac{m_e}{m}} \right) \delta^4 + \frac{v_{th}}{v_p} \right) \delta^1$$

$$\nabla_w f_0 = -\frac{\vec{w} - u e_z}{v_T^2} f_0 \rightarrow \left\| w \times \left(\vec{B}_0 \right) \cdot \nabla_w f_0 \right\| \propto \left\| \vec{w} \times \left(\vec{B}_0 \right) \cdot \left(\vec{w} - u e_z \right) f_0 \right\| = 0$$

$$\left\| \frac{q}{m} w \times \left(\vec{B}_1 \right) \cdot \nabla_w f_0 \right\| = \left\| \frac{q}{m} \vec{w} \times \left(\vec{B}_1 \right) \cdot \frac{\left(\vec{w} - u e_z \right)}{v_T^2} f_0 \right\| \Rightarrow$$

$$\left\| \frac{q}{m} \vec{w} \times \left(\vec{B}_1 \right) \cdot \left(\frac{u}{v_T^2} e_z \right) f_0 \right\| \approx \frac{e}{m} \frac{u}{v_{th}} B_1 f_0 \Rightarrow$$

$$\frac{e}{m} \frac{u}{v_{th}} B_1 f_0 \approx \frac{e}{m} \frac{u}{v_{th} v_p} E_1 f_0 \rightarrow \left(\frac{eE_1}{m v_{th} \omega} \frac{f_0}{f_1} \frac{u}{v_{th}} \right) \delta^1 \rightarrow \left(\sqrt{\frac{m_e}{m}} \right) \frac{u}{v_{th}} \delta^1$$

$$\left\| \frac{q\vec{E}_1}{m} \cdot \nabla_w f_0 \right\| \approx \frac{eE_1}{m v_{th}} f_0 \rightarrow \left(\frac{eE_1}{m v_{th} \omega} \frac{f_0}{f_1} \right) \delta^1 \rightarrow \left(\sqrt{\frac{m_e}{m}} \right) \delta^1$$

$$\left\| \frac{q}{m} \vec{w} \times \vec{B}_0 \cdot \nabla_w f_1 \right\| \approx \omega_c f_1 \approx \frac{m_e}{m} \omega f_1 \rightarrow \frac{m_e}{m} \delta^1$$

$$\left(\frac{\partial}{\partial t} f \right)_{collision} \approx \nu_{vollision} f \rightarrow \delta^5, \delta^6 \rightarrow negligible$$

The above ordering deserves some explanation:

1. The assumptions about the phase and group velocity of the wave will be justified once we calculate the wave's dispersion relation ($k_z = k_z(\omega, z)$).
2. Because of the axial variation of the magnetic field ($B_0(z)$), the gradient will comprise two terms: one that describes the variation on the scale of the wave's wave-length (k_z), and one that describes the variation on the scale of the plasma source length (L).
3. The term containing the drift speed is obviously smaller (by the factor u/v_p) than the other terms that we will be keeping in the first order kinetic equation; however, near the resonance region, the wave's phase velocity will approach zero, and the term containing the drift speed will become comparable. By the same argument, we will keep the contribution of the spatial gradient that varies on the scale of k_z because its magnitude is $\propto v_{th}/v_p$.
4. The collision term is negligible.
5. Because of the ion's large mass, to first order, there is no perturbation to the ion's velocity distribution function $f_{1ion} = 0$.

With the above ordering, the zero and first order kinetic equations for the electron become

1. $\vec{w} \times \vec{B}_0 \cdot \nabla_w f_0 = 0$:[1.4 – 46]; trivially satisfied

2. $$\frac{\partial}{\partial t} f_1 + w_z \frac{\partial}{\partial z} f_1 - \frac{f_0}{v_T^2} \vec{\xi}_1 \cdot \vec{w} + \Omega_0 \left(\vec{w} \times e_z\right) \cdot \nabla_w f_1 + \frac{f_0 u}{v_T^2} \left(\vec{w} \times \vec{\Omega}_1\right) \cdot e_z = 0 \quad :[1.4-47]$$

with $\vec{\Omega} \equiv \frac{q_e}{m_e}\vec{B}; \vec{\xi} \equiv \frac{q_e}{m_e}\vec{E}; q_e = -e$ and $\left(e_z \frac{\partial}{\partial z}\right) \times \vec{\xi}_1 = -\frac{\partial}{\partial t}\Omega_1$

The time dependence for f_1 is of course $f_1(z,t) = \mathrm{Re}\left(\tilde{f}_1 \exp(-i\omega t)\right)$. To analyze the space dependence without having to solve the above equation in the general case, we will examine the differential equation for the spatial variation of the complex electric field to obtain a clue. This differential equation has a form that is very similar to

$$\left(\tilde{E}\right)'' + k^2 \tilde{E} = 0$$

which has the solution : $\tilde{E} \propto \exp(ikz)$ for $k \neq k(z)$. However, for the case of $k = k(z)$, there is no general analytic solution. If, however, k is not a 'strong' function of 'z', which is equivalent to the requirement that the wave's wave-length ($\lambda = \frac{2\pi}{k}$) does not change substantially on the scale of the wave-length

$$\frac{1}{\lambda}|\delta\lambda| = \frac{1}{\lambda}\left|\left(\frac{d\lambda}{dz}\right)\lambda\right| = \left|\left(\frac{d\lambda}{dz}\right)\right| << 1 \Rightarrow \left|\frac{dk}{dz}\right| << k^2,$$

an approximate solution (known as the WKB approximate solution) can be implemented. The approximation uses the fact that the solution must approach the solution for $k \neq k(z)$ in the limit that the spatial variation vanishes. Hence, the solution must be of the form

$$\tilde{E} \cong A\exp(iS(z)) \quad [1.4-48]$$

substituting this form into the differential equation yields

$$iS'' - (S')^2 + k^2(z) = 0 \quad [1.4-49].$$

Now, we take advantage of the slow spatial variation and solve the equation by an order expansion in S

$$S \cong S_0 + S_1 + \ldots; \left|\frac{S_1}{S_0}\right| \approx \delta << 1 \text{ and } \left|\frac{S''}{(S')^2}\right| \approx \left|\frac{k'}{k^2}\right| \approx \delta .$$

Using the above order, the zero and first order equations for S become

$$\begin{matrix} (S_0')^2 = k^2(z) \\ iS_0'' - 2S_0'S_1' = 0 \end{matrix} :[1.4-50].$$

The zeroth order equation yields the solution

$$S_0(z) = \pm\int_{z_0}^{z} k(x)dx:[1.4-51];$$

where we will only keep the '+' sign (wave traveling in the +z-direction). Using this solution, the first order equation becomes

$$ik' - 2kS_1' = 0:[1.4-52],$$

which has the solution

$$S_1(z) = \frac{i}{2}\ln\left(\frac{k(z)}{k(z_0)}\right):[1.4-53].$$

Inserting the above relations for S into the form for the complex electric field yields

$$\begin{matrix} \tilde{E}(z) = \tilde{E}_0 \exp\left(-\frac{1}{2}\ln\left(\frac{k(z)}{k_0}\right) + i\int_{z_0}^{z} k(x)dx\right) = \\ \tilde{E}_0\sqrt{\left(\frac{k_0}{k(z)}\right)}\exp\left(i\int_{z_0}^{z} k(x)dx\right) \end{matrix} :[1.4-54].$$

where $k_0 = k(z_0)$.

If we examine the field's spatial variation, we find that

$$\tilde{E}' = \left(-\frac{1}{2k}k' + ik\right)\tilde{E}$$

and the ratio of the two components of the derivative is

$$\left|\frac{k'}{2k^2}\right| \approx \frac{1}{2}\delta << 1.$$

Hence, we will neglect the weaker contribution to the spatial derivative:

$$\Rightarrow \nabla \approx ik_z e_z .$$

With this approximation for the spatial variation, we can now easily solve for the first order perturbation to the distribution function. Before we continue, we should note that the approximation to the gradient is valid if the WKB approximation is satisfied; however, to validate the approximation, we will need $k(z) = F(\vec{\sigma}(z))$ (where $\vec{\sigma}$ is the plasma conductivity tensor), which requires the solution of the perturbed distribution function. Hence, we are making an ad-hoc assumption about the spatial dependence of the perturbed distribution function, an assumption that must be validated upon the inspection of the spatial profile of $k(z)$.

We now have the form for f_1's spatial and temporal dependence:

$$f_1(z,t,\vec{w}) = \mathrm{Re}\left(\tilde{f}_1(z,\omega,\vec{w})\exp\left(i\left(\int k dz - \omega t\right)\right)\right) : [1.4-55]$$

and

$$\nabla \approx ik_z e_z : [1.4-56] .$$

With this approximation for the spatial dependence, the equation for $\tilde{f}_1$ becomes:

$$-i\omega_{ref}\tilde{f}_1+\Omega_0\left(\vec{w}\times e_z\right)\cdot\nabla_w\tilde{f}_1=\left(\tilde{\tilde{\xi}}\cdot\vec{w}-ue_z\cdot\left(\vec{w}\times\tilde{\tilde{\Omega}}_1\right)\right)\frac{f_0}{v_T^2}$$

$$\tilde{\tilde{\Omega}}_1=\frac{1}{v_p}e_z\times\tilde{\tilde{\xi}} \qquad :[1.4-57].$$

$$\omega_{ref}\left(w_z\right)=\omega-k_z w_z;v_p=\frac{\omega}{k_z}$$

By eliminating $\tilde{\tilde{\Omega}}_1$, we have

$$-i\omega_{ref}\tilde{f}_1+\Omega_0\left(\vec{w}\times e_z\right)\cdot\nabla_w\tilde{f}_1=\left(1-\frac{u}{v_p}\right)\frac{f_0}{v_T^2}\tilde{\tilde{\xi}}\cdot\vec{w}:[1.4-58].$$

Noticing that $f_0=f_0\left(w^2,w_z\right)$, we will represent $\tilde{f}_1$ as

$$\tilde{f}_1(\vec{w})=C\left(w^2,w_z\right)w_x+D\left(w^2,w_z\right)w_y:[1.4-59]$$

and use polar coordinates to evaluate the second term in equation 1.4-58:

$$w_x=w\cos(\theta)$$
$$w_y=w\sin(\theta)$$
$$\left(\vec{w}\times e_z\right)\cdot\nabla_w\tilde{f}_1\rightarrow -we_\theta\cdot\left(e_w\frac{\partial}{\partial w}+\frac{e_\theta}{w}\frac{\partial}{\partial\theta}\right)\tilde{f}_1=-\frac{\partial}{\partial\theta}\tilde{f}_1\Rightarrow \qquad :[1.4-60].$$
$$-Cw\sin(\theta)+Dw\cos(\theta)=-Cw_y+Dw_x$$

Combining equations 1.4-58,59,60, we obtain

$$\left[i\omega_{ref}C+\Omega_0 D+\left(1-\frac{u}{v_p}\right)\frac{f_0}{v_T^2}\tilde{\xi}_x\right]w_x+\left[i\omega_{ref}D-\Omega_0 C+\left(1-\frac{u}{v_p}\right)\frac{f_0}{v_T^2}\tilde{\xi}_y\right]w_y=0:[1.4-61].$$

The coefficients of the two velocity components must vanish separately, yielding two equations and two unknowns: C and D; note that the solutions for C and D will be functions of w^2 and w_z only, satisfying the requirement for our construction of $\tilde{f}_1$.

Solving for C and D, and inserting the solutions into the expression for $\tilde{f}_1$ yields

$$\tilde{f}_1(\vec{w}) = \left(\frac{\left(1 - \frac{u}{v_p}\right)}{\omega_{ref}^2 - \Omega_0^2} \frac{f_0}{v_T^2} \right) \left(i\omega_{ref} \left(\xi_x + i \frac{\Omega_0}{\omega_{ref}} \xi_y \right) w_x + \Omega_0 \left(\xi_x + i \frac{\omega_{ref}}{\Omega_0} \xi_y \right) w_y \right) : [1.4-62].$$

Now, we are ready to solve for the conductivity tensor:

$$\tilde{\vec{J}} = \vec{\vec{\sigma}} \cdot \tilde{\vec{E}} = q_e \int d^3 w \vec{w} \tilde{f}_1(\vec{w}).$$

We first notice that $\tilde{f}_1$ is an odd function of w_x and w_y; therefore,

$$\tilde{J}_z \propto \int d^3 w w_z \tilde{f}_1(\vec{w}) = \int dw_z w_z \iint_{w_x, w_y} dw_x dw_y \tilde{f}_1 = 0$$

as expected, and the other two components reduce to

$$\begin{aligned} \tilde{J}_x &= q_e i \left(1 - \frac{u}{v_p}\right) \int dw_z \left(\frac{\omega_{ref}}{\omega_{ref}^2 - \Omega_0^2} \right) \left(\xi_x + i \frac{\Omega_0}{\omega_{ref}} \xi_y \right) \left(\int dw_x dw_y \frac{f_0}{v_T^2} w_x^2 \right) \\ \tilde{J}_y &= q_e \left(1 - \frac{u}{v_p}\right) \int dw_z \left(\frac{\Omega_0}{\omega_{ref}^2 - \Omega_0^2} \right) \left(\xi_x + i \frac{\omega_{ref}}{\Omega_0} \xi_y \right) \left(\int dw_x dw_y \frac{f_0}{v_T^2} w_y^2 \right) \end{aligned} : [1.4-63].$$

Because of the symmetry of the Maxwellian distribution function (in the perpendicular direction), the integrals over the perpendicular velocity components for the two components of the current density are identical:

$$f_0^{paral}(w_z) = \int dw_x dw_y \frac{f_0}{v_T^2} w_x^2 = \int dw_x dw_y \frac{f_0}{v_T^2} w_y^2 = \frac{n}{\pi^{1/2} v_{th}} \exp\left(- \frac{(w_z - u)^2}{v_{th}^2} \right).$$

The components of the conductivity tensor then become (remember that $\tilde{\xi} = \frac{q_e}{m_e} \tilde{E}$):

$$\sigma_{xx} = \sigma_{yy} = \frac{q_e^2}{m_e} i\left(1 - \frac{u}{v_p}\right)\int dw_z \left(\frac{\omega_{ref}}{\omega_{ref}^2 - \Omega_0^2}\right) f_0^{paral}(w_z)$$

$$\sigma_{xy} = -\sigma_{yx} = -\frac{q_e^2}{m_e}\left(1 - \frac{u}{v_p}\right)\int dw_z \left(\frac{\Omega_0}{\omega_{ref}^2 - \Omega_0^2}\right) f_0^{paral}(w_z) \quad :[1.4-64].$$

By inserting the relations between the components of the conductivity tensor into the coupled differential equations for the RHCP and the LHCP electric fields, we see that the equations become de-coupled:

$$\left(\widetilde{E}_R\right)'' + k_0^2\left(1 + \frac{\left[\sigma_{xx} + i\sigma_{xy}\right]}{-i\omega\varepsilon_0}\right)\widetilde{E}_R = 0$$

$$\left(\widetilde{E}_L\right)'' + k_0^2\left(1 + \frac{\left[\sigma_{xx} - i\sigma_{xy}\right]}{-i\omega\varepsilon_0}\right)\widetilde{E}_L = 0 \quad :[1.4-65].$$

$$\widetilde{E}_R = \sqrt{2}\widetilde{E}_{RHCP} = \widetilde{E}_x - i\widetilde{E}_y$$

$$\widetilde{E}_L = \sqrt{2}\widetilde{E}_{LHCP} = \widetilde{E}_x + i\widetilde{E}_y$$

From previous arguments, we know that the LHCP component can interact only with the ions (if the wave frequency is near the ion cyclotron frequency; this is not the case for our plasma). Therefore, because the LHCP and the RHCP components are de-coupled, we only need to examine the RHCP component. Hence,

$$k_z^2 \equiv k_0^2\left(1 + \frac{\sigma_R}{-i\omega\varepsilon_0}\right), \text{ where: } \sigma_R \equiv \sigma_{xx} + i\sigma_{xy},$$

and the equation for the RHCP component becomes

$$\left(\widetilde{E}_R\right)'' + k_z^2\widetilde{E}_R = 0$$

$$k_z^2 = \left(\frac{\omega}{c}\right)^2\left(1-\frac{q_e^2}{\omega\varepsilon_0 m_e}\left(1-\frac{u}{v_p}\right)\int dw_z\left(\frac{\omega_{ref}-\Omega_0}{\omega_{ref}^2-\Omega_0^2}\right)f_0^{paral}(w_z)\right)\Rightarrow$$

$$k_z^2 = \left(\frac{\omega}{c}\right)^2\left(1-\frac{\omega_{pe}^2}{\omega}\left(1-\frac{u}{v_p}\right)[Int]\right) \qquad :[1.4-66]$$

$$q_e = -e;\omega_{ce} = \frac{eB_0}{m_e};\omega_{pe}^2 = \frac{e^2 n_e}{\varepsilon_0 m_e}$$

$$n_e \approx 10^{18} m^{-3} \Rightarrow \frac{\omega_{pe}^2}{\omega^2} \approx 13.4$$

where

$$Int = \left(\frac{1}{\pi^{1/2} v_{th}}\right)\int dw_z\left(\frac{1}{(\omega-\omega_{ce})-k_z w_z}\right)\exp\left(-\left(\frac{w_z-u}{v_{th}}\right)^2\right)$$

$$\Rightarrow\left(\frac{1}{\pi^{1/2} v_{th} k_z}\right)\int_{-\infty}^{\infty} dw_z\left(\frac{-1}{w_z-\left(\frac{\omega-\omega_{ce}}{k_z}\right)}\right)\exp\left(-\left(\frac{w_z-u}{v_{th}}\right)^2\right) \qquad :[1.4-67].$$

Now, remember that we have neglected the initial conditions for the complex $\tilde{f}_1$. This neglect is equivalent to the assumption that the initial transients will 'die out'. However, the contribution to $\tilde{f}_1$ from the particles that are initially in resonance with the field will not 'die out'; therefore, if we are to include the resonant interaction, we must evaluate the integral using the Landau prescription:

As stated above, our analysis is only valid if

$$f_1(t_{initial}) = f_1(t=-\infty) = 0,$$

but

$$f_1(t) = \mathrm{Re}\left(\tilde{f}_1 \exp(-i\omega t)\right) = \mathrm{Re}\left(\tilde{f}_1 \exp\left(-i\omega_r t + \omega_i t\right)\right)$$

and as $t \to -\infty$

$$\left\| f_1(t \to -\infty) \right\| \propto \left(\left\| \tilde{f}_1 \right\| \exp\left(-\omega_i (t \to \infty) \right) \right)$$

and would approach zero if $\omega_i > 0$. Hence our analysis is valid for $\omega_i > 0$. However, the wave-particle resonance will result in energy transfer from the field to the electrons, requiring a decrease in the wave's energy with time, thereby requiring that $\omega_i < 0$:

$$U_{wave}(t) \propto E^2(t) \propto \exp(2\omega_i t) \Rightarrow \frac{dU}{dt} < 0 \text{ if } \omega_i < 0.$$

What is the implication of the above statements in the evaluation of the integral? The integral has a pole at

$$w_z = \frac{\left((\omega_r + i\omega_i) - \omega_{ce} \right)}{k_r}, \left(\mathrm{Im}(k_z) = 0 \Rightarrow \text{no spatial decay} \right)$$

which is in the upper half of the complex w-plane. However, as previously stated, we are interested in the case of a wave that is temporally decaying $\Rightarrow \omega_i < 0$, which requires that we analytically continue our solution to the lower half of the complex w-plane as shown in figure 1.4-4:

FIGURE 1.4-4: AN ILLUSTRATION OF THE CONTOUR INTEGRATION

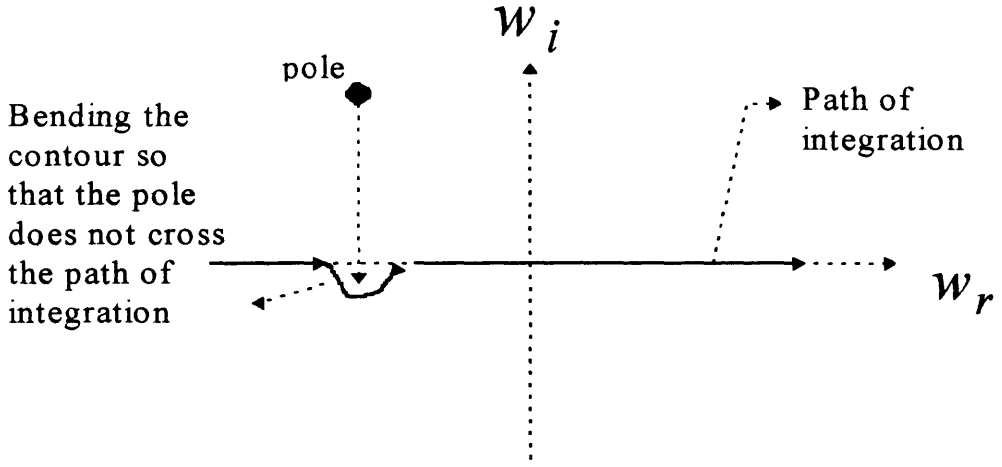

In the limit that $\omega_i \to 0^-$ (weak dampening), the integral will have two components:

1. The principal part : $P \Rightarrow \left(\int_{-\infty}^{w^*-\delta} dw_z + \int_{w^*+\delta}^{\infty} dw_z \right)_{\delta \to 0}$ where $w^* \equiv \left(\frac{\omega_r - \omega_{ce}}{k_r} \right)$,

   which is the 'real' component of the pole.

2. The counter clock-wise infinitesimal semi-circular path that is taken to avoid the pole : $= i\pi \operatorname{Res}\left(w = w^*\right)$, where the residue of an integral , $Int = \int dx F(x)$, for a single pole is defined as

$$\operatorname{Res}\left(x = x^*\right) \equiv \left(\left(x - x^*\right) F(x) \right)_{x \to x^*}$$

Hence equation 1.4-67 becomes:

$$Int = \left[\frac{1}{\pi^{1/2} v_{th} k_r} P \int_{-\infty}^{\infty} dw_z \frac{-1}{w_z - v_p^*} \exp\left(-\left(\frac{w_z - u}{v_{th}} \right)^2 \right) \right] - i \frac{\pi^{1/2}}{v_{th} k_r} \exp\left(-\left(\frac{v_p^* - u}{v_{th}} \right)^2 \right) : [1.4-68].$$

$$k_r \equiv \operatorname{Re}\left(k_z\right); \operatorname{Im}\left(k_z\right) = 0; v_p^* \equiv w^* \equiv \frac{\omega_r - \omega_{ce}}{k_r}$$

Far from the resonance region, for a 'cold' plasma $\equiv \frac{w}{v_p^*} \approx \frac{v_{th}}{v_p^*} << 1$, we can evaluate the principal value by the approximation

$$\frac{-1}{w - v_p^*} = \frac{1}{v_p^*} \frac{1}{1 - \frac{w}{v_p^*}} \approx \frac{1}{v_p^*} \left(1 + \frac{w}{v_p^*} + \left(\frac{w}{v_p^*} \right)^2 \right),$$

and the integral becomes

$$Int = \frac{1}{\omega - \omega_{ce}} \left(1 + \frac{u}{v_p^*} + \frac{1}{\left(v_p^* \right)^2} \left(v_T^2 + u^2 \right) \right) - i \frac{\pi^{1/2}}{v_{th} k_r} \exp\left(- \left(\frac{v_p^* - u}{v_{th}} \right)^2 \right) :[1.4-69].$$

$$k_r \equiv \mathrm{Re}\left(k_z \right); v_p^* \equiv w^* \equiv \frac{\omega_r - \omega_{ce}}{k_r}$$

With the expression for the integral, we finally have the expression for the wave-number

$$k_z^2 = \left(\frac{\omega}{c} \right)^2 \left(1 - \frac{\omega_{pe}^2}{\omega} \left(1 - \frac{u}{v_p} \right) \left[\begin{array}{l} \frac{1}{\omega - \omega_{ce}} \left(1 + \frac{u}{v_p^*} + \frac{1}{\left(v_p^* \right)^2} \left(v_T^2 + u^2 \right) \right) \\ - i \frac{\pi^{1/2}}{v_{th} k_r} \exp\left(- \left(\frac{v_p^* - u}{v_{th}} \right)^2 \right) \end{array} \right] \right) :[1.4-70].$$

$$k_r \equiv \mathrm{Re}\left(k_z \right); v_p = \frac{\omega}{k_r}; v_p^* \equiv w^* \equiv \frac{\omega_r - \omega_{ce}}{k_r}$$

The finite drift and electron temperature will become important near resonance ($\omega \to \omega_{ce}$) where (as we will show), $k_r \to \infty \Rightarrow v_p, v_p^* \to 0$, but our approximation of a 'cold' plasma is valid far from resonance; furthermore, our analysis is only valid in the region where the WKB approximation is satisfied, which (as we will show) is again far from the resonance. Therefore, to simplify the analysis, we will drop the terms that include the finite temperature and drift effects; the simplification yields:

$$k_z^2 = \left(\frac{\omega}{c}\right)^2 \left(\left(1 + \frac{\omega_{pe}^2}{\omega(\omega_{ce} - \omega)}\right) + i\left(\frac{\pi^{1/2}\omega_{pe}^2}{\omega v_{th} k_r} \exp\left(-\left(\frac{v_p^* - u}{v_{th}}\right)^2\right)\right)\right)$$

$$\omega = \omega_r + i\omega_i \qquad :[1.4-71].$$

$$k_z = k_r$$

Now, the ratio of the real to the imaginary term scales as

$$\frac{\omega_{pe}^2}{\omega^2}\frac{v_p}{v_{th}} \exp\left(-\left(\frac{v_p^* - u}{v_{th}}\right)^2\right) \approx 500\exp\left(-10^3\right) \approx 0.$$

Therefore, we expect that $\frac{\omega_i}{\omega_r} << 1$, and the solution for the complex frequency can be approximated (far from resonance: $\frac{\omega_i^2}{(\omega_{ce} - \omega_r)^2} << 1$) as

$$k_z^2 \cong \left(\frac{\omega_r}{c}\right)^2 \left(1 + \frac{\omega_{pe}^2}{\omega_r(\omega_{ce} - \omega_r)}\right) :[1.4-72]$$

$$\frac{\omega_i}{\omega_r} \cong -\frac{\pi^{1/2}}{2} \frac{\left(\frac{\omega_{pe}^2}{k_z v_{th} \omega_r}\right) \exp\left(-\left(\frac{\frac{\omega_r - \omega_{ce}}{k_z} - u}{v_{th}}\right)^2\right)}{\left(1 + \frac{\omega_{ce}}{2\omega_r}\frac{\omega_{pe}^2}{(\omega_{ce} - \omega_r)^2}\right)} :[1.4-73].$$

With the above expressions, we are in the position to verify the WKB approximation: $\left|\frac{dk}{dz}\right| << k^2$. The expression for the wave-number shows that the wave-number is a function of the electron cyclotron frequency, which has an axial dependence

that is depicted in figure 1.4-2. To find the region of validity, we will graph

$$\alpha(z) \equiv \frac{1}{k_z^2}\left\|\frac{dk_z}{dz}\right\| :$$

FIGURE 1.4-5: THE ILLUSTRATION OF THE REGION OF VALIDITY FOR THE WKB APPROXIMATION

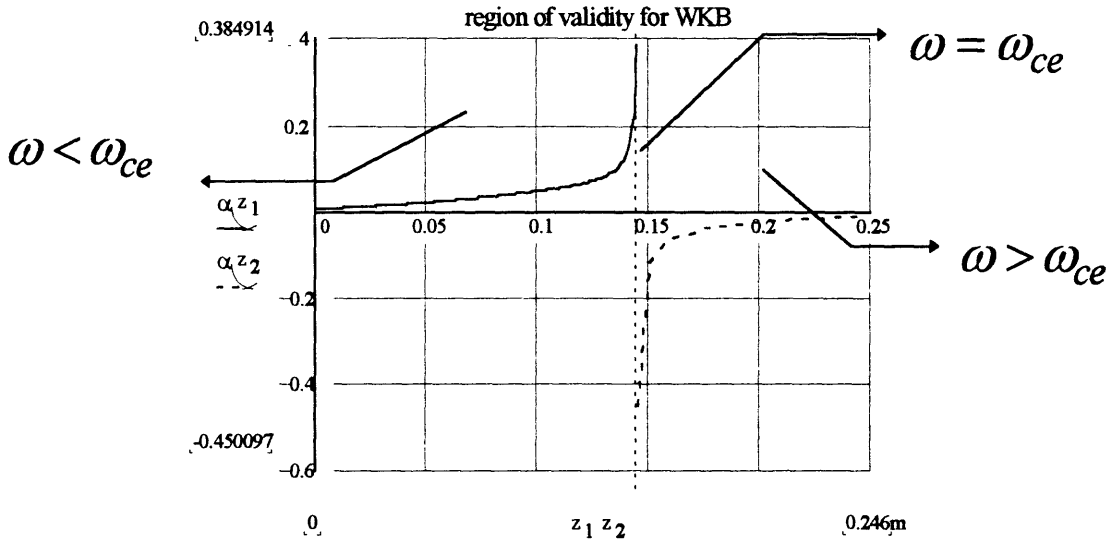

The figure shows that the WKB approximation is valid except within $\approx 1cm$ of the region of resonance. Incidentally, the figure also shows that the wave is evanescent for $\omega > \omega_{ce}$ (wave-number becomes imaginary), implying that the wave can not propagate to the resonance region if it is launched from the low-field side.

With the expression 1.4-72, we can also validate our approximations of the phase and group velocity:

$$\frac{v_p}{c} \equiv \frac{\omega_r}{ck_r} = \frac{1}{\sqrt{1+\dfrac{\omega_{pe}^2}{\omega_r(\omega_{ce}-\omega_r)}}} :[1.4-74], \text{ and}$$

$$\frac{v_g}{c} \equiv \frac{1}{c}\frac{d\omega_r}{dk_r} = \frac{2(\omega_{ce}-\omega_r)^2\omega_r}{2\omega_r(\omega_{ce}-\omega_r)^2+\omega_{pe}^2\omega_{ce}}\sqrt{\left(1+\frac{\omega_{pe}^2}{\omega_r(\omega_{ce}-\omega_r)}\right)} :[1.4-75].$$

Far from the resonance region, where $\left(\omega_{ce}-\omega_r\right)\approx\omega_r$,

$\frac{v_p}{c}\approx\frac{1}{4}$, and $\frac{v_g}{c}\approx\frac{1}{2}$; (the same numbers used in our approximations).

To determine the importance of power absorption that results from $\mathrm{Im}(\omega)$, we need to estimate the quantity: $\exp\left(-\omega_i\tau\right)$, where $\tau\equiv\int_0^{z_{res}}\frac{dz}{v_g(z)}$ is the wave's residence time. Far from resonance $\omega_i\tau\cong 10^{-500}=0$; therefore, in this region, ω_i's contribution to power absorption is negligible.

By neglecting ω_i's contribution, the expression for the time averaged power flux density (averaged over $\frac{2\pi}{\omega_r}$) will be shown to be a constant: independent of the axial position, implying that there is no power absorption in the non-resonant region:

$$\theta(z,t)=\int k_r(z)dz-\omega_r t$$

$$\left\langle\vec{P}\right\rangle_{time}\equiv\frac{\omega_r}{2\pi}\int_0^{\frac{2\pi}{\omega_r}}dt\left[\mathrm{Re}\left(\tilde{\tilde{E}}(z,\omega_r)\exp\left(i\theta(z,t)\right)\right)\right]\times\left[\mathrm{Re}\left(\tilde{\tilde{H}}(z,\omega_r)\exp\left(i\theta(z,t)\right)\right)\right]\Rightarrow$$

$$\frac{\omega_r}{2\pi}\int_0^{\frac{2\pi}{\omega_r}}dt\left[\left(\tilde{\tilde{E}}_r\cos\left(\theta(z,t)\right)\right)-\left(\tilde{\tilde{E}}_i\sin\left(\theta(z,t)\right)\right)\right]\times\left[\left(\tilde{\tilde{H}}_r\cos\left(\theta(z,t)\right)\right)-\left(\tilde{\tilde{H}}_i\sin\left(\theta(z,t)\right)\right)\right]\Rightarrow$$

$$\frac{\omega_r}{2\pi}\int_0^{\frac{2\pi}{\omega_r}}dt\left[\begin{array}{l}\left(\tilde{\tilde{E}}_r\times\tilde{\tilde{H}}_r\cos^2\left(\theta(z,t)\right)+\tilde{\tilde{E}}_i\times\tilde{\tilde{H}}_i\sin^2\left(\theta(z,t)\right)\right)\\-\left(\tilde{\tilde{E}}_r\times\tilde{\tilde{H}}_i+\tilde{\tilde{E}}_i\times\tilde{\tilde{H}}_r\right)\sin\left(\theta(z,t)\right)\cos\left(\theta(z,t)\right)\end{array}\right]\Rightarrow$$

$$\frac{1}{2}\left(\tilde{\tilde{E}}_r\times\tilde{\tilde{H}}_r+\tilde{\tilde{E}}_i\times\tilde{\tilde{H}}_i\right)=\frac{1}{2}\mathrm{Re}\left(\tilde{\tilde{E}}\times\tilde{\tilde{H}}^*\right)$$

$$\nabla \times \tilde{\vec{E}} \exp(i\theta(z,t)) = i\omega_r \mu_0 \tilde{\vec{H}} \exp(i\theta(z,t)).$$

We are only concerned with the RHCP-component of the electric field; hence, using the result of the WKB derivation for the electric field,

$$\tilde{\vec{H}} \exp(i\theta) = \frac{1}{i\omega_r \mu_0} \nabla \times \left(\tilde{E}_{RHCP}(z) e_R \exp(i\theta) \right) \Rightarrow$$

$$\tilde{\vec{H}} = \frac{1}{i\omega_r \mu_0} \left(ik_r + \frac{1}{2k_z} \frac{dk_r}{dz} \right) e_z \times \tilde{E}_{RHCP}(z) e_R$$

$$= \frac{1}{i\omega_r \mu_0} \left(ik_r + \frac{1}{2k_z} \frac{dk_r}{dz} \right) \left(-i\tilde{E}_{RHCP}(z) e_R \right) =$$

$$\frac{-1}{\omega_r \mu_0} \left(ik_r + \frac{1}{2k_z} \frac{dk_r}{dz} \right) \left(\tilde{E}_{RHCP}(z) e_R \right)$$

With the expression for $\tilde{\vec{H}}$,

$$\tilde{\vec{E}} \times \tilde{\vec{H}}^* = \frac{\left\| \tilde{E}_{RHCP} \right\|^2}{-\omega_r \mu_0} \left(-ik_r + \frac{1}{2k_z} \frac{dk_r}{dz} \right) \left(e_R \times e_R^* \right) =$$

$$\frac{\left\| \tilde{E}_{RHCP} \right\|^2}{-\omega_r \mu_0} \left(-ik_r + \frac{1}{2k_z} \frac{dk_r}{dz} \right) \left(-ie_z \right)$$

and

$$\langle \vec{P} \rangle = \frac{1}{2} \mathrm{Re} \left(\tilde{\vec{E}} \times \tilde{\vec{H}} \right) = \frac{\left\| \tilde{E}_{RHCP}(z) \right\|^2}{2\omega_r \mu_0} k_r e_z$$

Now, note that $\tilde{E}_{RHCP}(z) = \tilde{E}_0 \sqrt{\frac{k_0}{k_r(z)}}$, where $k_0 = \frac{\omega_r}{c}$; hence

$$\langle \vec{P} \rangle = \frac{1}{2} \mathrm{Re} \left(\tilde{\vec{E}} \times \tilde{\vec{H}} \right) = \frac{\left\| \tilde{E}_0 \right\|^2}{2c\mu_0} e_z = \frac{\varepsilon_0 \left\| \tilde{E}_0 \right\|^2}{2} c e_z : [1.4 - 76] : \text{independent of 'z'}.$$

This derivation suggests that most of the power will be absorbed within the resonance region, which has a width of order $\leq 1cm$, and for a typical electro-magnet current setting, is located $\approx 15cm$ from the target.

What does the localized nature of the power absorption imply about the influence of the magnetic field strength and flux geometry? The absorbed power will increase the perpendicular electron temperature; therefore, its localized nature results in an axial peak in the electron temperature, where the location of the peak is controlled by the electro-magnet current settings. We have already discussed the influence of the electron temperature. Based on that discussion, we can state that a local peak in the electron temperature will result in the local increase of copper and argon ions; therefore, by 'moving' the resonance region closer to the target, we can enhance the trapping efficiency of the copper atoms leaving the target (via enhanced ionization near the target) and simultaneously increase the ion flux (argon and copper) to the target, which will increase the number of sputtered copper atoms. The increase in the number of sputtered copper atoms will 'cool' the plasma (decrease the electron temperature), and this decrease as discussed in a previous section has ramifications for the fate of the plasma surface parameters. But is the peak significant? In other words, what is $\frac{\delta T_e^{peak}}{T_e}$? To answer this question, we will need to analyze the electron energy equation. The energy equation balances convective and conductive heat transport, and frictional energy loss (energy loss to the ions for example) with external source heating. We will make the most conservative assumptions (to determine the maximum temperature peak) by neglecting most terms, terms that include the effects of

1. fluid flow : slow $\Rightarrow \frac{u}{v_T} << 1$

2. convection: small with respect to conduction

$$\Rightarrow \frac{nTu/L_{paral}}{\kappa T/L_{paral}^2} \approx \frac{nTuL_{paral}}{(nT/mv_{coll}^e)T} = \frac{mv_{coll}^e uL_{paral}}{T} =$$

$$\frac{v_{coll}^e L_{paral}}{v_T}\frac{u}{v_T} \approx \frac{L_{paral}}{\lambda_{mfp}^e}\frac{u}{v_T} \approx \frac{u}{v_T} << 1$$

3. viscosity: weak gradients and slow flows

4. frictional heating:

$$\frac{v_{coll}^e mnu^2}{\kappa T/L_{paral}^2} \approx \frac{v_{coll}^e mnu^2}{\left(nT/v_{coll}^e m\right)T/L_{paral}^2} =$$

$$\frac{L_{paral}^2\left(v_{coll}^e\right)^2 u^2}{v_T^4} = \left(\frac{L_{paral}}{\lambda_{mfp}^e}\right)^2\left(\frac{u}{v_T}\right)^2 \approx \left(\frac{u}{v_T}\right)^2 << 1$$

5. and perpendicular heat transport: small because the electrons are 'highly' magnetized: $\frac{v_{collision}^{energy}}{\omega_{ce}} \approx \frac{m_e}{m_{Ar}}\frac{v_{collision}^{elastic}}{\omega_{ce}} << 1$; we note that anomalous transport will increase the perpendicular heat transport which will reduce the peak in the temperature; hence, neglecting it will result in a conservative estimate of the temperature peak.

The physics that remains is the removal of the heat provided by the external source by parallel conduction.

$$-\frac{\partial}{\partial z}\left(\kappa_{paral}^e \frac{\partial}{\partial z} T_{eV}\right) = P_{watts/cm^3}^{ext} : [1.4-77].$$

We know that most of the power is absorbed within $\cong 1cm$ of the resonance region. Now the parallel electron conductivity is approximately[3]

$$\kappa^{e}_{paral} \cong 2.9 \cdot 10^{-3} T_{eV}^{5/2} \cdot watts/cm^{3} .$$

Hence the energy equation for the region, which has a volume of order $cm \times 100cm^{2}$, that absorbs the power, which is of order $4kW$, becomes

$$\left(T^{5/2} T'\right)' = -\eta$$
$$\eta = 4 \frac{(eV)^{7/2}}{cm^{2}} \quad :[1.4-78] .$$
$$(\,)' \equiv \frac{\partial}{\partial z}$$

The solution to this equation with the assumption of symmetry with respect to the center of the region yields

$$\Delta T \equiv T(0) - T(z) = T(0) - \left[T^{7/2}(0) - \frac{7}{4} \eta(z)^{2} \right]^{2/7} \Rightarrow$$
$$\Delta T \cong T(0) \left[1 - \left(1 - \frac{2}{7} \frac{7}{4} \frac{\eta(z)^{2}}{T^{7/2}(0)} \right) \right] = \frac{\eta}{2} z^{2} \frac{1}{T^{5/2}(0)} \quad :[1.4-79] .$$

For $z \cong .5cm$,

$$\frac{\Delta T}{T} \cong \frac{0.5}{T_{eV}^{7/2}(0)} \approx \frac{0.5}{(5)^{7/2}} \cong 10^{-3} << 1$$

Hence, the peak is negligible, and the preceding discussion about the electro-magnets' control of the bulk plasma parameters through its control of the axial location of the resonance region is invalid.

[3] NRL Plasma Formulary, 1994, pp. 37-8

Yet, it has been experimentally demonstrated (figure 1.4-6) that a change in the electro-magnet currents (from 230A/180A to 160A/160A) results in a substantial increase in the target current.

FIGURE 1.4-6: EXPERIMENTAL MEASUREMENT OF AN INCREASE IN TARGET CURRENT WITH CHANGING ELECTRO-MAGNET SETTINGS.

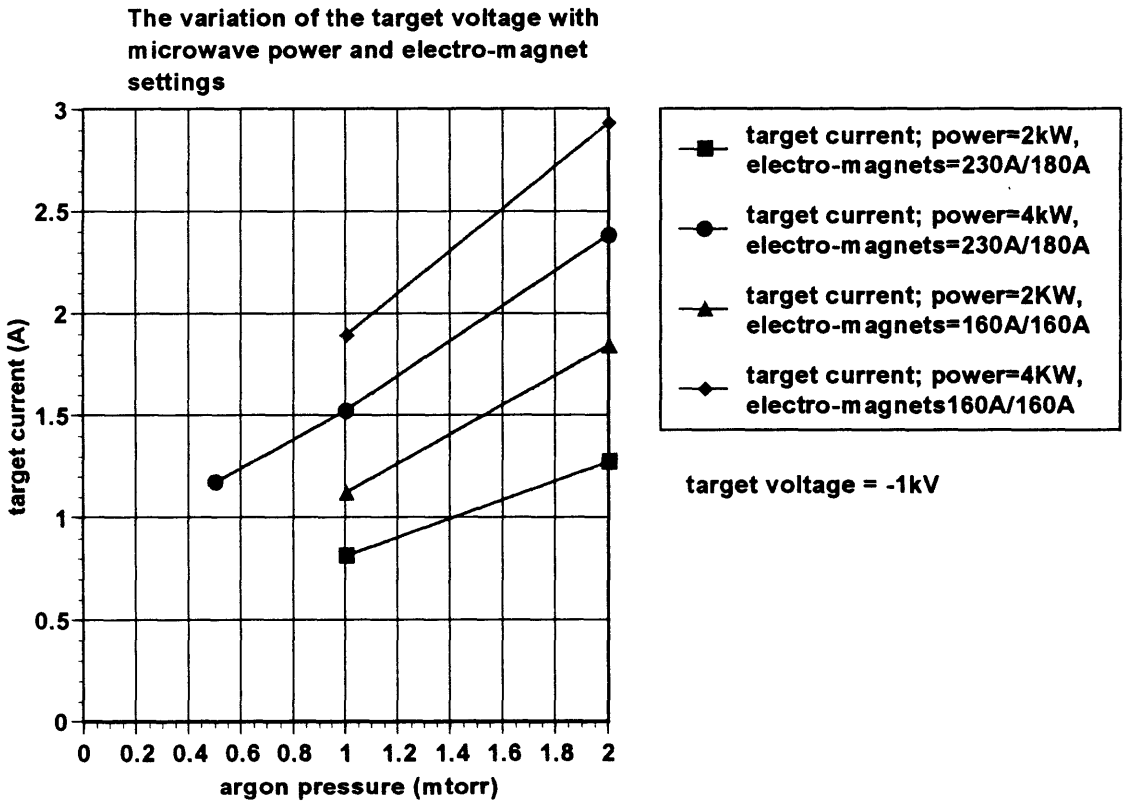

A significant peak in the electron temperature would have explained the increase in the target current; however, we just demonstrated that the peak is negligible. So what does cause this increase? One explanation is the mirror force. The mirror force exists when the magnetic field has a spatial variation along its direction. The force is directed along the field in the direction of decreasing magnetic field. Therefore, charged species moving towards the target (in the direction of increasing field) will experience a retarding force

that can prevent them from reaching the target. We will demonstrate this mirror force by examining single particle motion as well as macroscopic fluid motion. The single particle motion of a particle in an axially varying magnetic field is represented, as before, by

$$\begin{aligned} &\frac{\partial}{\partial t}\vec{v} = \vec{v} \times \vec{\Omega}(r,z) \\ &\vec{\Omega}(r,z) \equiv \frac{q}{m}\vec{B}(r,z) \end{aligned} \quad :[1.4-80]$$

To make the calculation tractable, we will

1. neglect the temporal evolution of the fields: $\frac{\partial}{\partial t}\vec{B},\vec{E} \approx 0$: the fast time scale ($\approx \frac{2\pi}{\omega} \cong 0.4n\,\text{sec}$) corresponds to the small perturbations from the fields of the microwave, which will add an elliptic component to the circular orbit and an azimuthal drift but will not influence the particle orbit on the longer time scales.
2. assume a spatially 'slowly' varying field, (marginally satisfied):

$$\left\|\frac{\nabla B}{B}\right\|\left(v_z \frac{2\pi}{\Omega}\right) \approx \frac{.5T/m}{.1T}\left(10^3\, m/s\right)\frac{2\pi}{1.5\cdot 10^5 s^{-1}} \approx .2 < 1$$

3. use the 'long-thin' approximation $\left|\frac{B_r}{B_z}\right| << 1$, (satisfied near the axis $r \approx 0$):

$$\begin{aligned} &\nabla \cdot \vec{B} = 0 \Rightarrow \frac{1}{r}\frac{\partial}{\partial r}\left(rB_r\right) + \frac{\partial}{\partial z}B_z = 0 \\ &B_z(r,z) \cong B_z(0,z) + \left[\frac{\partial}{\partial r}B_z(0,z)\right]r \approx B_z(0,z) \\ &rB_r \approx -\int dr r \frac{\partial}{\partial z}B_z(0,z) \Rightarrow B_r \approx -\frac{r}{2}\frac{\partial}{\partial z}B_z(0,z) \Rightarrow \\ &\left|\frac{B_r}{B_z}\right| \approx \frac{r}{2}\left|\frac{1}{B_z}\frac{\partial}{\partial z}B_z(0,z)\right| \approx \frac{r}{2L_{B_z}} \approx \frac{r}{2(.1m)} \approx \frac{r_{larmor}}{20cm} \cong \frac{1cm}{20cm} << 1 \end{aligned} \quad :[1.4-81]$$

4. assume that the fields generated by the plasma current are negligible compared to the field created by the electro-magnets:

$$\frac{\|\nabla \times \vec{B}\| R_{plasma}}{B} \approx \frac{B_\theta}{B} = \frac{R_{plasma}\mu_0 J_z}{B} \approx \frac{R_{plasma}\mu_0 \dfrac{I_{target}}{A_{target}}}{B} \Rightarrow$$

$$\frac{\mu_0(10cm)\left(.03\,A/cm^2\right)}{.1T} \cong 10^{-4} << 1$$

5. neglect the effects of any electric field (as implied by the equation): the established electric field in the plasma is negligible because the plasma potential profile in nearly flat : $E_0 \approx \|\nabla\Phi\| < \frac{1V}{.1m} \Rightarrow \frac{E_0}{\|\vec{v} \times \vec{B}_o\|} \approx .1 << 1$

6. neglect collisions: $\frac{\nu_{collision}}{\Omega} \approx 1$, (not a well satisfied assumption)

The only assumption that could invalidate the following analysis is the neglect of collisions, but we will continue the analysis under the above assumptions and discuss later the ramifications of not satisfying assumption #6.

We will solve the equation of motion by a perturbation expansion, justified by assumptions #2 and #3:

$$\vec{v} \cong \vec{v}_0 + \vec{v}_1; \frac{v_1}{v_0} << 1$$
$$\vec{\Omega}(r,z) \cong \Omega_0(0,z(t=0))e_z + \vec{\Omega}_1(r,z);$$
$$\vec{\Omega}_1(r,z) = \Omega_{1z}(z)e_z + \Omega_r(r,z(0))e_r;$$
$$\Omega_r(r,z(0)) = -\frac{r}{2}\left(\frac{\partial}{\partial z}\Omega_0(0,z(0))\right); \qquad :[1.4-82].$$
$$\Omega_{1z}(z) = \left(\frac{\partial}{\partial z}\Omega_0(0,z(t=0))\right)(z - z(t=0))$$
$$\left|\frac{\Omega_1}{\Omega_0}\right| << 1; \frac{\partial}{\partial r}\Omega_0(0,z) = 0$$

With this expansion, the equation of motion becomes:

$$\dot{\vec{v}}_0 = \left[\Omega_0(0,z(0))\right](\vec{v}_0 \times e_z)$$
$$\dot{\vec{v}}_1 = \left[\Omega_0(0,z(0))\right](\vec{v}_1 \times e_z) + \vec{a}_1(r,z); \quad :[1.4-83].$$
$$\vec{a}_1(r,z) = \vec{v}_0 \times \vec{\Omega}_1(r,z)$$

The zero order equation was solved previously for the electron, and the solution can be easily modified for the ion:

$$\dot{\varphi} = -\Omega_0(r=0,z(0)) = -\frac{q}{m}B_0(r=0,z(0))$$
$$v_\varphi(t) = v_\varphi(0) = \rho\dot{\varphi}$$
$$v_z(t) = v_z(0)$$
$$\varphi(t) = \varphi(0) - \Omega_0 t \qquad :[1.4-84].$$
$$\vec{R}(t) = \vec{r}(t) + \vec{z}(t) =$$
$$\vec{r}_g + \rho\left(\cos(\varphi(t))e_x + \sin(\varphi(t))e_y\right) + \left(z(0) + v_z t\right)e_z;$$
$$\rho = \left|\frac{v_\varphi(0)}{\Omega_0(r=0,z(0))}\right|$$

FIGURE 1.4-7: THE ZERO ORDER 'PERPENDICULAR' MOTION OF AN ION IN A 'SLOWLY' SPATIALLY VARYING MAGNETIC FIELD

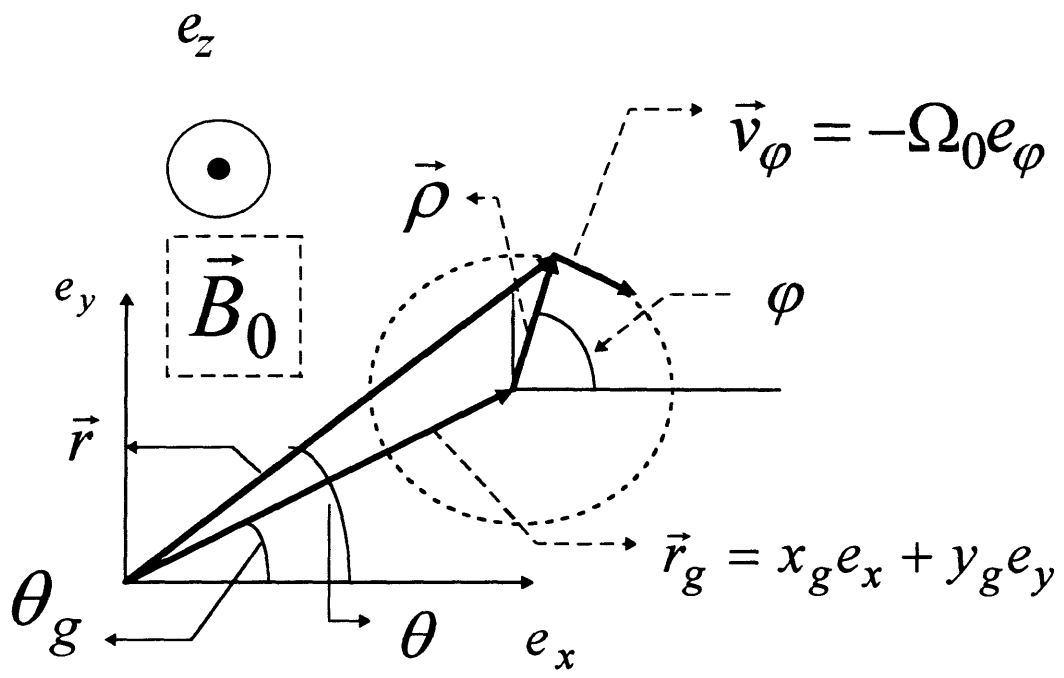

The first order correction has three parts:

1. the addition of an elliptic component to the circular orbit: this correction is not significant to our analysis, and we will show that this correction will disappear when we examine the 'long' time (long with respect to the ion-cyclotron period) consequence of the correction.
2. the addition of a drift that will force the particle to move along the field line.
3. the mirror force, which acts to retard the ion's parallel motion (with respect to the zero order magnetic field) when the ion is moving towards a region of increasing magnetic field strength.

These corrections result from the acceleration term:

$$\vec{a}_1(r(t),z(t)) = \vec{v}_0(t) \times \vec{\Omega}_1(r(t),z(t)) \Rightarrow$$
$$v_\varphi \left[e_\varphi(t) \times \left(\Omega_{1z}(z(t)) e_z + \Omega_r(r(t),z(0)) e_r(t) \right) \right] + v_z \Omega_r(r(t),z(0)) \left(e_z \times e_r(t) \right) =$$
$$v_\varphi \left[\Omega_{1z}(z(t)) e_\rho(t) + \Omega_r(r(t),z(0)) \left(e_\varphi(t) \times e_r(t) \right) \right] + v_z \Omega_r(r(t),z(0)) \left(e_z \times e_r(t) \right) =$$
$$v_\varphi \left[\begin{array}{l} \left(\frac{\partial}{\partial z} \Omega_0(r=0,z(0)) \right) (v_z t) e_\rho(t) \\ -\frac{1}{2} \left[\frac{\partial}{\partial z} \Omega_0(r=0,z(0)) \right] \left(\left[e_\varphi(t) + \frac{v_z}{v_\varphi} e_z \right] \times \vec{r}(t) \right) \end{array} \right] \quad :[1.4-85].$$

With

$$e_\rho(t) = \left[\cos(\varphi(t)) e_x + \sin(\varphi(t)) e_y \right]$$
$$e_\varphi(t) = \left[-\sin(\varphi(t)) e_x + \cos(\varphi(t)) e_y \right]$$
$$\vec{r}(t) = \vec{r}_g + \vec{\rho}(t) = \left[\left(x_g + \rho \cos(\varphi(t)) \right) e_x + \left(y_g + \rho \sin(\varphi(t)) \right) e_y \right] \quad :[1.4-86]$$
$$e_\varphi(t) \times \vec{r}(t) = -\left[\cos(\Omega_0 t) x_g + \sin(-\Omega_0 t) y_g + \rho \right] e_z$$
$$e_z \times \vec{r}(t) = \left[\left(x_g + \rho \cos(\varphi(t)) \right) e_y - \left(y_g + \rho \sin(\varphi(t)) \right) e_x \right] \Rightarrow$$
$$r(t) e_\theta(t) = r_g e_{\theta_g} + \rho e_\varphi(t)$$

we can average over one cyclotron period to eliminate the 'elliptic' correction:

$$\langle F(t) \rangle \equiv \frac{|\Omega_0|}{2\pi} \int_0^{\frac{2\pi}{|\Omega_0|}} dt F(t) \Rightarrow$$

$$\langle t e_\rho(t) \rangle = \langle t \cos(\Omega_0 t) \rangle e_x + \langle t \sin(-\Omega_0 t) \rangle e_y = \vec{0}$$
$$\langle e_\varphi(t) \times \vec{r}(t) \rangle = -\rho e_z \quad :[1.4-87],$$
$$\langle e_z \times \vec{r}(t) \rangle = r_g e_{\theta_g}$$

and the first order equation for the motion of the particle on the 'longer' time scale becomes:

$$\left\langle \dot{\vec{v}}_1 \right\rangle = \left[\Omega_0(0,z(0))\right]\left(\left\langle \vec{v}_1 \right\rangle \times e_z\right) + \left\langle \vec{a}_1(r,z) \right\rangle$$

$$\left\langle \vec{a}_1(r,z) \right\rangle = v_\varphi \left[-\frac{1}{2}\left[\frac{\partial}{\partial z}\Omega_0(r=0,z(0))\right]\left[-\rho e_z + \frac{v_z}{v_\varphi} r_g e_{\theta_g} \right]\right] : [1.4-88].$$

The averaged acceleration term, as stated above, will yield a drift and the mirror force.

The drift is determined by setting $\left\langle \dot{\vec{v}}_1 \right\rangle = 0$:

$$0 = \left[\Omega_0(0,z(0))\right]\left(\left\langle \vec{v}_{Drfit} \right\rangle \times e_z\right) + \left\langle \vec{a}_1(r,z) \right\rangle \Rightarrow$$

$$\left\langle \vec{v}^{Drift} \right\rangle = \frac{-e_z \times \left\langle \vec{a}_1(r,z) \right\rangle}{\left[\Omega_0(0,z(0))\right]} = \frac{v_z\left(-\frac{1}{2}\left[\frac{\partial}{\partial z}\Omega_0(r=0,z(0))r_g\right]\right)e_{r_g}}{\left[\Omega_0(r=0,z(0))\right]} \Rightarrow : [1.4-89].$$

$$\frac{\left\langle v_{r_g}^{Drift} \right\rangle}{v_z} = \frac{\Omega_r(r_g,z(0))}{\Omega_0(r=0,z(0))} = \frac{B_r(r_g,z(0))}{B_z(0,z(0))}$$

Note that to first order $B(0,z) = B(r_g,0)$ because $\frac{\partial}{\partial r}B(0,z) = 0$; therefore,

$$\frac{\left\langle v_{r_g}^{Drift} \right\rangle}{v_z} = \left(\frac{dr}{dz}\right) = \frac{B_r(r_g,z(0))}{B_z(r_g,z(0))} : [1.4-90].$$

Equation 1.4-90, as we claimed, states that the ion's drift trajectory is along the field line. Now, we are left with the z-component of the acceleration term, which will yield the mirror force. From equation 1.4-88,

$$\left\langle a_{1z}(r_g,z_g)\right\rangle = -\rho v_\varphi\left[-\frac{1}{2}\left[\frac{\partial}{\partial z}\Omega_0(r_g,z_g)\right]\right] = \left\langle \dot{v}_{1z}\right\rangle \equiv \frac{d}{dt_{long}}v_z$$

$$F_z = m\frac{d}{dt_{long}}v_z = +m\Omega_0\rho^2\left[-\frac{1}{2}\left[\frac{\partial}{\partial z}\Omega_0(r_g,z_g)\right]\right] \Rightarrow$$

$$F_z = -\frac{1}{2}\frac{mv_\varphi^2}{\Omega_0(r_g,z_g)}\frac{\partial}{\partial z}\Omega_0(r_g,z_g) = -\mu_{mirror}\nabla_z B_0(r_g,z_g) \quad :[1.4-91]$$

$$\mu_{mirror} = \frac{\frac{1}{2}mv_\varphi^2(r_g,z_g)}{B_0(r_g,z_g)} = \frac{E_{perp}(r_g,z_g)}{B_0(r_g,z_g)}$$

with all components evaluated at the guiding center position. To demonstrate the influence of the mirror force, we will examine the case where collisions are negligible (this case is not representative of the ions in our plasma). If collisions and established electric fields can be neglected then the ion's total energy will remain constant:

$$\vec{v}\cdot\left(m\frac{d\vec{v}}{dt} = q\vec{v}\times\vec{B}\right) \Rightarrow$$

$$\frac{d}{dt}\left(\frac{1}{2}mv^2\right) = \frac{d}{dt}(E) = q\vec{v}\cdot\left(\vec{v}\times\vec{B}\right) = 0 \quad :[1.4-92].$$

Therefore,

$$\frac{d}{dt}\left(E_{perp}+E_z\right) = 0 :[1.4-93],$$

and

$$v_z e_z\cdot\left(e_z m\frac{d}{dt}v_z = -\mu_{mirror}\nabla_z B_0(z)\right) =$$

$$\frac{d}{dt}\left(\frac{1}{2}mv_z^2\right) = \frac{d}{dt}E_z = -\mu_{mirror}v_z e_z\cdot\nabla_z B_0(z) = -\mu_{mirror}\frac{d}{dt}B_0(z(t)) \Rightarrow :[1.4-94];$$

$$\frac{d}{dt}\left(E_z+\mu_{mirror}B_0\right) = -B_0\frac{d}{dt}\mu_{mirror}$$

but from equation 1.4-91,

$$\mu_{mirror} B_0 = E_{perp};$$

therefore,

$$\frac{d}{dt}\mu_{mirror} = \frac{-1}{B_0}\frac{d}{dt}\left(E_z + E_{perp}\right) = 0 : [1.4-95]$$

implying that $\mu_{mirror} = \frac{E_{perp}}{B_0}$ is constant along the particles trajectory; hence, if the ion is moving towards the direction of increasing magnetic field, its perpendicular energy will also increase; because the total energy is conserved, the increase in the perpendicular energy is accommodated by a decrease in the parallel energy, resulting in a decrease in the parallel velocity.

To establish the 'macroscopic' influence of the mirror force, we will examine its effect on the ion fluid velocity. Before we begin, we will establish a convenient coordinate system, illustrated in figure1.4-8

FIGURE 1.4-8: ILLUSTRATION OF THE MAGNETIC FLUX GEOMETRY

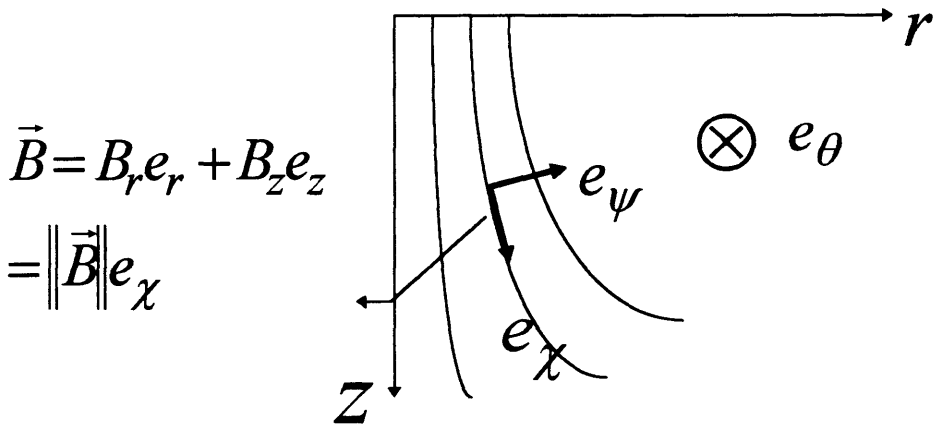

To isolate the influence of the magnetic field geometry on the ion flow velocity, we will make the following approximations:

1. cross-field diffusion is negligible compared to the flows along the field and in the azimuthal direction: $u_\psi << u_\chi, u_\theta$

2.neglect viscosity

3.neglect neutral flow velocity

4. neglect electron inertia : $\frac{u_e}{u_i} \approx \sqrt{\frac{m_i}{m_e}} \approx 300 \Rightarrow \frac{m_e u_e}{m_i u_i} \approx \sqrt{\frac{m_e}{m_i}} << 1$

5.quasi-neutrality: $n_e \approx n_i$

6. $\frac{\partial}{\partial \theta}(scalar) = 0$; because of symmetry

With these assumptions, we will add the momentum equations for the electron, ion and neutral species to eliminate the collision terms to obtain:

$$\begin{aligned} & m_e n_e \vec{u}_e \cdot \nabla \vec{u}_e + m_i n_i \vec{u}_i \cdot \nabla \vec{u}_i = e(n_i - n_e)\vec{E} + \vec{J} \times \vec{B} - \nabla p \Rightarrow \\ & m_i n_i \vec{u}_i \cdot \nabla \vec{u}_i = \vec{J} \times \vec{B} - \nabla p \\ & p = n_e T_e + n_i T_i + n_n T_n \\ & \vec{J} = e(n_i \vec{u}_i - n_e \vec{u}_e); J_\psi \approx 0 \\ & \vec{u}_i \cong u_\theta e_\theta + u_\chi e_\chi \end{aligned} \quad :[1.4-96].$$

Note that

$$\begin{aligned} & \nabla \equiv \frac{1}{h_\psi}\frac{\partial}{\partial \psi} + \frac{1}{h_\chi}\frac{\partial}{\partial \chi} + \frac{1}{h_\theta}\frac{\partial}{\partial \theta} \\ & h_\lambda \equiv \left\| \frac{\partial}{\partial \lambda}(r e_r + z e_z) \right\| \end{aligned} \quad :[1.4-97],$$

and

$$\begin{aligned} & \vec{u} \cdot \nabla \vec{u} \cong (u_\theta e_\theta + u_\chi e_\chi) \cdot \nabla (u_\theta e_\theta + u_\chi e_\chi) \Rightarrow \\ & \frac{u_\theta}{h_\theta}\left(u_\chi \frac{\partial}{\partial \theta} e_\chi + u_\theta \frac{\partial}{\partial \theta} e_\theta\right) + \frac{u_\chi}{h_\chi}\left(e_\chi \frac{\partial}{\partial \chi} u_\chi + u_\chi \frac{\partial}{\partial \chi} e_\chi + e_\theta \frac{\partial}{\partial \chi} u_\theta + u_\theta \frac{\partial}{\partial \chi} e_\theta\right) \end{aligned} \quad :[1.4-98]$$

with

$$
\begin{aligned}
&e_\psi = e_\theta \times e_\chi = \frac{\left(B_z e_r - B_r e_z\right)}{B} = \left(b_z e_r - b_r e_z\right) \\
&\frac{\partial}{\partial \chi} e_\theta, e_r = 0 \\
&\frac{\partial}{\partial \theta} e_\theta = -e_r \qquad :[1.4-99]. \\
&\frac{\partial}{\partial \theta} e_\chi = \frac{\partial}{\partial \theta}\frac{\vec{B}}{B} = \frac{\partial}{\partial \theta}\left(b_r e_r + b_z e_z\right) = b_r e_\theta \\
&\frac{\partial}{\partial \chi} e_\chi = \frac{\partial}{\partial \chi}\left(\frac{B_r e_r + B_z e_z}{B}\right) = \frac{1}{B^2}\left(B_z \frac{\partial}{\partial \chi} B_r - B_r \frac{\partial}{\partial \chi} B_z\right) e_\psi
\end{aligned}
$$

We will examine the θ and χ components of the momentum equation (1.4-96):

$$
\begin{aligned}
&\frac{1}{u_\theta}\frac{\partial}{\partial \theta} u_\theta = -\frac{h_\chi}{r} b_r \\
&\frac{1}{2h_\chi}\frac{\partial}{\partial \chi} u_\chi^2 = \frac{u_\theta^2}{r} b_r - \frac{1}{n_i m_i}\frac{\partial}{\partial \chi} p
\end{aligned}
\qquad :[1.4-100]
$$

and make the additional assumption that the parallel gradient in the density and temperature are negligible because of the large magnitude of the parallel diffusion and thermal conductivity coefficients; this assumption may not be well satisfied if the strengths of the parallel diffusion and thermal conduction can not overcome the mirror force, which acts to retard the parallel motion of the charged particles in the direction of increasing magnetic field. But we will make this assumption to simplify the analysis: $\frac{\partial}{\partial \chi} p \approx 0$. We will now solve equation 1.4-100 for the azimuthal fluid velocity to obtain:

$$
u_\theta = u_{0\theta} \exp\left(-\int d\chi \frac{h_\chi}{r(\chi)} b_r(\chi)\right) :[1.4-101].
$$

To simplify this further, we will limit the analysis to the particles that are near the axis($r \approx 0$). Near the axis, the field lines are approximately in the z-direction; therefore,

$$e_\chi \approx e_z \Rightarrow h_\chi \approx h_z = 1,$$

and

$$b_r(\chi) = \frac{B_r(\chi)}{B(\chi)} \approx \frac{B_r(r,z)}{B_z(z)} \cong -\frac{r}{2}\frac{1}{B_z(z)}\frac{\partial}{\partial z}B_z(0,z).$$

Hence,

$$u_\theta = u_{0\theta}\exp\left(\frac{1}{2}\int dz \frac{1}{B_z(z)}\frac{\partial}{\partial z}B_z(0,z)\right) = u_{0\theta}\exp\left(\frac{1}{2}\ln\left(\frac{B_z(z)}{B_z(z_0)}\right)\right) \Rightarrow$$
$$u_\theta = u_{0\theta}\sqrt{\frac{B_z(z)}{B_z(z_0)}} \qquad :[1.4-102].$$

With the expression 1.4-102 for u_θ, the equation for u_χ becomes

$$\frac{1}{2h_\chi}\frac{\partial}{\partial \chi}u_\chi^2 \approx \frac{1}{2}\frac{\partial}{\partial z}u_z^2 \approx \frac{u_\theta^2}{r}b_r \approx \frac{u_{0\theta}^2\left(\frac{B_z(z)}{B_{z0}}\right)}{r}\left(-\frac{r}{2}\frac{1}{B_z(z)}\frac{\partial}{\partial z}B_z(z)\right) \Rightarrow$$
$$\frac{\partial}{\partial z}u_z^2 \approx -u_{0\theta}^2\frac{\partial}{\partial z}\frac{B_z(z)}{B_{z0}} \qquad :[1.4-103].$$

Equation 1.4-103 states that as the ion moves towards the direction of increasing magnetic field ($\frac{\partial}{\partial z}\frac{B_z(z)}{B_{z0}}\Uparrow$), the ion's parallel velocity decreases, thereby demonstrating the action of the mirror force on the fluid level.

As shown in figure 1.4-2, the axial variation of B_z is greater when there is a large difference between the top and bottom electro-magnets; hence, we expect that the mirror force will be stronger for the case of $\frac{I_{top}}{I_{bot}} = \frac{230A}{180A}$, thereby yielding a smaller target

current, which is what we claimed to have been observed experimentally. The ramifications of the mirror force are

1. the control of the target current by the electro-magnet current settings
2. the target current determines the sputtering rate of the copper atoms into the plasma
3. the copper sputtering rate influences the rate of electron energy loss via excitation and ionization of the copper atoms
4. the electron energy loss rate influences the electron temperature.
5. The electron temperature's influence on the plasma surface parameters has been discussed in a previous section.

We have discussed the influence of the magnetic field strength and topology on microwave power absorption and on ion mobility parallel to the field. Now, we will discuss one last effect: the influence on cross-field diffusion. We have already observed the influence of the field strength on the cross-field diffusion coefficient in our discussion of the influence of the argon atom density:

$$D_{Cu^+} = \left(\frac{\nu_{Cu^+}^2}{\nu_{Cu^+}^2 + \Omega_{Cu^+}^2} \frac{T_{Cu^+}/m_{Cu}}{\nu_{Cu^+}} \right), \text{ where } \Omega_{Cu^+} = \frac{e}{m_{Cu^+}} \left\| \vec{B} \right\|$$

An increase in the magnetic field will reduce the ion cross-field diffusion. But what about the field topology? The field topology will induce charge particle drifts. These drifts result from the forces created by the field line curvature and gradients in the field strength.

$$0 = \vec{F} + \vec{v}_{Drift} \times \vec{\Omega} \Rightarrow$$

$$\vec{v}_{Drift} = \frac{\vec{F} \times \vec{\Omega}}{\Omega^2} \qquad :[1.4-104]$$

The important point is that the magnetic field created by the electro-magnets only has components in the 'r' and 'z' direction, and the forces associated with the field gradient and curvature are also in the 'r' and 'z' direction; hence, the drifts are in the azimuthal direction and do not contribute to cross-field diffusion.

CHAPTER 2

2.0: EXPERIMENTS

We have discussed in theory the relation among the plasma bulk parameters and the plasma surface parameters, but we have not shown any experimental results to substantiate the claims. Furthermore, the discussions were qualitative: we stated the direction of the change in the parameters but did not give an estimate on the magnitude of the change. In fact, the knowledge of the magnitude is crucial in understanding the significance of these parameters to the fill quality. Why? As was stated in the introduction, we have analyzed the fill quality for various combinations of the operating parameters (microwave power, gas pressure, electro-magnet current, and target voltage), and we have not seen any definite trends in the fill quality with any of these operating parameters; now, if we find that a particular plasma surface parameter (for example, the copper-to-argon ion fraction at the substrate) does not vary significantly within the range of our operating parameter space, then we can conclude that one possibility for the lack of a trend in the fill quality is the lack of a significant change in this surface parameter. Conversely, if we find that this surface parameter has varied significantly, then we can conclude that the fill quality is independent of this parameter.

Unfortunately, the surface parameters that would yield a more detailed picture of the fill evolution, such as the ion velocity distribution function, $f_{ion}(\vec{v})$, and the double differential sputtering cross-section, $\frac{d^2}{d\Omega dE} S_{(Cu,Ar)/Cu}(E,\Omega)$, are difficult to analyze. However, the information on a couple of the parameters (surface and bulk) such as the electron temperature (T_e), the substrate copper to argon ion fraction ($f^{sub}_{Cu^+/Ar^+}$), and the

substrate copper ion to neutral fraction ($f^{sub}_{Cu^+/Cu^0}$) is much more accessible. The focus of this chapter will be on the experimental determination of these parameters.

2.1: MEASUREMENT OF THE ELECTRON TEMPERATURE AND DENSITY $[T_e, n_e]$

The measurement of the electron temperature is quite standard; the measurement is made by a Langmuir probe, which is nothing more than an appropriately shaped piece of metal that is inserted in the plasma and is in electrical contact with a variable voltage source. The variation in the current drawn by this probe with the source voltage for $V_s < V_f$ (where V_f is the floating potential, the potential at which no current is drawn by the probe) measures the electron population's ability to overcome the retarding potential created by the probe, thereby, yielding a measure of the electron population's mobility, which is a function of its thermal speed or equivalently its temperature. The theory behind the measurement for a single ion species plasma is given by Hutchinson[1]; we will extend his derivation to model a two ion species plasma (copper and argon ions).

First, we must describe the shape and the size of the metal piece used for the measurement. A typical probe is cylindrical with its side and one edge exposed to the plasma. Its length and radius are of the order millimeters. The physics that pertains to the measurement of the electron temperature and density is the physics of the sheath, which , as discussed, is created at most plasma-boundary interfaces (surfaces which are parallel to the magnetic field will not form the sheath described because of the reduced electron mobility to the surface).

The sheath forms as a result of the disparity in the electron and ion mass. Electrons, being much 'lighter' than the ions $\frac{m_e}{m_i} \approx \frac{1}{70{,}000}$ (for argon ions), are more

mobile; therefore, they reach the plasma boundaries first and charge the surface to a negative potential with respect to the positive core; this potential difference increases the ion transport to the surface while simultaneously retarding the electron transport. The surface will continue to charge negatively until the magnitude of the potential hill is able to counter the disparity in the ion and electron mobilities, thereby yielding an ambi-polar drift (electrons and ions drifting to the surface at equal rates). Because of the large electron mobility, the electric field created by this potential difference will only penetrate a few Debye-lengths into the plasma, which is the ratio of the speed with which the electric field can penetrate into the plasma (the 'average' electron speed) to the plasma response frequency: $\lambda_D \equiv \frac{v_{Te}}{\omega_{pe}} = \sqrt{\frac{\varepsilon_0 T_e}{e^2 n_e}} \approx 10\mu m$. Therefore, near the sheath the ions and electrons will 'see' the probe as a flat surface because the probe radius of curvature is much larger than the sheath thickness : $\frac{5\lambda_D}{a_{probe}} \approx \frac{50\mu m}{1mm} = 0.05 << 1$. We will begin the analysis by writing the equations for the electron and ion velocity distribution functions at steady state

1. we are neither concerned with the fluctuations in the distribution functions from plasma 'noise'
2. nor with the dynamics resulting from the ramping of the surface potential, which occurs in the process of obtaining the I-V characteristic. The ramp rate, which can be as large as $10^3 V/\text{sec}$, is still much smaller than the plasma response frequency

[1] I. H. Hutchinson, Principles of Plasma Diagnostics, 1987, Chp. 3

($f_{pe} \approx 10^{10}/\sec$); hence, the distribution function reaches steady state before the current measurement is taken.

At steady state the governing equations for the distribution functions become:

$$\vec{w}\cdot\nabla_r f_e(\vec{r},\vec{w}) - \frac{e}{m_e}\left(\vec{E}(\vec{r}) + \vec{w}\times\vec{B}(\vec{r})\right)\cdot\nabla_w f_e(\vec{r},\vec{w}) = \left(\hat{L}^{op}_{collision} + \hat{L}^{op}_{ex,iz}\right)_e f_e(\vec{r},\vec{w})$$
$$\vec{w}\cdot\nabla_r f_i(\vec{r},\vec{w}) + \frac{e}{m_i}\left(\vec{E}(\vec{r}) + \vec{w}\times\vec{B}(\vec{r})\right)\cdot\nabla_w f_i(\vec{r},\vec{w}) = \left(\hat{L}^{op}_{collision} + \hat{L}^{op}_{ex,iz}\right)_i f_i(\vec{r},\vec{w}) \quad :[2.1-1]$$

where the right hand side represents the change in the distribution functions that result from elastic collisions (among the three species: electrons, ions, and neutrals) and from inelastic collisions (excitation and ionization collisions with the neutrals). Noting that the current to the probe is only a function of the velocity component directed towards the probe, and that we are treating the case where the probe surface normal is parallel to the magnetic field (e_z), we will integrate over the other two velocity components to obtain:

$$\nabla_{perp}\cdot\iint d^2w_{perp}\vec{w}_{perp}f_e(\vec{r},\vec{w}) + w_z\frac{\partial}{\partial z}f_e^{1D}(\vec{r},w_z) - \frac{e}{m_e}\left(E_z(\vec{r})\right)\frac{\partial}{\partial w_z}f_e^{1D}(\vec{r},w_z)$$
$$= \iint d^2w_{perp}\left(\hat{L}^{op}_{collision} + \hat{L}^{op}_{ex,iz}\right)_e f_e(\vec{r},\vec{w})$$
$$\nabla_{perp}\cdot\iint d^2w_{perp}\vec{w}_{perp}f_i(\vec{r},\vec{w}) + w_z\frac{\partial}{\partial z}f_i^{1D}(\vec{r},w_z) + \frac{e}{m_i}\left(E_z(\vec{r})\right)\frac{\partial}{\partial w_z}f_i^{1D}(\vec{r},w_z) \quad :[2.1-2]$$
$$= \iint d^2w_{perp}\left(\hat{L}^{op}_{collision} + \hat{L}^{op}_{ex,iz}\right)_i f_i(\vec{r},\vec{w})$$

If the probe surface normal is at an angle with respect to the magnetic field, then the electric field created by the sheath will have a component that is perpendicular to the magnetic field, and the motion of the charged particles will render the analysis more complicated. The force on the electron induced by the perpendicular electric field can become comparable to the force exerted by the magnetic field:

$$\frac{E_{perp}}{wB} \approx \frac{(\Phi/l_{sheath})\sin\theta}{v_{th}B} \approx \frac{\left(2\cdot 10^6 \frac{V}{m}\right)\sin\theta}{\left(2\cdot 10^6 \frac{m}{s}\right)(.04T)} = 25\sin\theta$$

$$\sin\theta = \hat{E}\times\hat{B}$$

$$\text{for } \sin\theta \geq 2^\circ \Rightarrow \frac{E_{perp}}{wB} \geq 1$$

The perpendicular electric field will introduce an ellipticity into the electron cyclotron orbit. The Larmor radius of the electron is $= \frac{v_{th}^e}{\omega_{ce}} \approx 0.1mm$, and the probe size is of the order of a mm; hence, the probe 'sees' the electron as 'magnetized' restricted to move along the magnetic field line. We can account for the restricted electron motion by using an effective collection area in the calculation of the electron current density: the component of the probe area that is normal to the field line. The force on the ion resulting from E_{perp} will dominate the magnetic field force:

$$\frac{E_{perp}}{wB} \approx \frac{(\Phi/l_{sheath})\sin\theta}{B\sqrt{\frac{T_e}{m_i}}\sin\theta} \approx \frac{\left(2\cdot 10^6 \frac{V}{m}\right)}{\left(3.5\cdot 10^3 \frac{m}{s}\right)(.04T)} = 10^4 >> 1;$$

if we compare the ion Larmor radius to the probe size and the ion cyclotron period to the ion sheath transit time, we find that

$$\frac{\rho_{larmor}^{ion}}{l_{probe}} \approx \sqrt{\frac{m_i}{m_e}}\frac{\rho_{larmor}^{ion}}{l_{probe}} \approx (300)(.1) = 30 >> 1$$

$$\frac{\tau_{ci}}{\tau_{sheath}} \approx \frac{2\pi}{\omega_{ci}\left(\frac{l_{sheath}}{v_{sheath}}\right)} \approx \frac{2\pi}{9.6\cdot 10^4 s^{-1}}\frac{5\cdot 10^3 m/s}{.1mm} \cong 10^3 >> 1,$$

implying that the ion is not 'magnetized' because its gyro-radius is much greater than the probe size (negligible curvature in the trajectory) and because the ion will reach the probe well before it even begins to make a gyro-orbit. Hence, when we analyze the ion contribution to the probe current, we will neglect the effect of the magnetic field.

We will first treat the electron contribution to the probe current. The electron drift toward the probe will be retarded by the potential hill, and most of the electrons will have their directed speed reduced to zero (and many will be reflected); hence, their transit time through the sheath will be much longer than the elastic electron-electron coulomb collision time, enabling the electron population to relax nearly to a Maxwellian. The electron distribution can not become fully Maxwellian because of

1. absorption by the probe (the electrons with sufficient energy to overcome the potential hill will be absorbed by the probe; therefore, the high energy tail in the distribution moving away from the probe will be depleted);

2. the finite drift resulting from the absorption by the probe:

$$u_z(z) = \frac{1}{\sqrt{\pi} v_{th}} \int_{\sqrt{\frac{2}{m_e}\left(V(z)-V_{probe}\right)}}^{\infty} dw_z w_z \exp\left(-\frac{w_z^2}{v_{th}^2}\right)$$

$$= \frac{v_{th}}{2\sqrt{\pi}} \exp\left(-\frac{\left(V(z)-V_{probe}\right)}{T_e}\right)$$

which near the sheath is $\approx \frac{e^{-3}}{2\sqrt{\pi}} v_{th} \cong 0.01 v_{th}$;

3. the energy loss sustained by the electrons in the high energy tail via excitation and ionization collisions with the neutral gas atoms (excitation and ionization collisions with argon atoms has an energy threshold of about $11eV$ and

$16eV$ respectively, the latter energy being approximately the ionization energy). For our plasma, the electron temperature (as will be shown) is about $5eV$, and the collision frequency for excitation and ionization collisions becomes comparable to the electron-electron collision frequency for electron energies $\geq 20eV$:

$$\frac{\nu_{ee}^{coul}}{\nu_{ex/iz}} \propto \frac{n_e}{n_g} \frac{1}{(\frac{E}{E_{iz}} - 1)}$$

$$\frac{n_e}{n_g} \leq 10\% \Rightarrow$$

$$\frac{\nu_{ee}^{coul}}{\nu_{ex/iz}}(E \geq 20eV) \leq 1$$

However, the fraction of the electron population at these energies for a Maxwellian distribution is

$$frac(\geq 20eV) \cong \frac{\int_{\sqrt{20/T_e}}^{\infty} z^2 \exp(-z^2) dz}{\int_0^{\infty} z^2 \exp(-z^2) dz} \leq 5\%;$$

therefore, excitation and ionization collisions mainly alter (deplete) the tail of the distribution function, but at lower energies, where most of the electron population resides, the distribution is 'Maxwellian'. The depletion of the high energy tail via absorption by the probe is also minute for probe potentials below the floating potential: for $|V_o - V_p| \geq |V_f - V_p| \approx 18eV$, the fraction of the electron population near the sheath that can overcome the potential hill and be absorbed (noting that probe absorption occurs only in one dimension) is

$$frac(18eV) \cong \frac{1}{2}\frac{\int_{\sqrt{18/T_e}}^{\infty}\exp(-z^2)dz}{\int_{0}^{\infty}\exp(-z^2)dz} \le 1\%$$

Even though the tail comprises a minute part of the distribution, it plays the dominant role in determining

1. excitation and ionization collision rates,
2. electron energy flux to the boundaries (the fraction of the electrons at high energies is small, but the energy carried by these electrons is obviously large; therefore, the tail contributes significantly to the energy flux),
3. ion energy flux to the boundaries (the tail of the distribution determines the potential drop through the sheath which determines the energy that is lost in accelerating the ions through the sheath at the 'floating' surfaces);

$V_p - V_f \cong 3.5T_e \approx 18eV$ for our plasma, whereas for a Maxwellian electron distribution $V_p - V_f \cong 5T_e \approx 25eV$, indicating that the electron distribution in our plasma is not Maxwellian.

The inelastic collision rates and the particle energy loss to the boundaries in turn influence the particle creation and loss rates as well as the volumetric and boundary energy loss rates, which ultimately determine the electron density and temperature. However, in our theory regarding the measurement of the electron temperature, we will assume a purely Maxwellian electron velocity distribution with the understanding that the deviation from a Maxwellian distribution, which will arise at the tail because of the inelastic collisions and absorption by the probe, will not greatly alter our analysis in measuring T_e.

With the assumption of a Maxwellian electron distribution, the contribution of the collision operators acting on the electron distribution function vanish along with the first term representing the drift across the magnetic field, yielding

$$w_z \frac{\partial}{\partial z} f_{e,Max}^{1D}(\vec{r}, w_z) - \frac{e}{m_e}\left(E_z(\vec{r})\right)\frac{\partial}{\partial w_z} f_{e,Max}^{1D}(\vec{r}, w_z) = 0 \quad [2.1-3].$$

With the substitution

$$\nabla \times \vec{E} \cong 0 \Rightarrow \vec{E} = -\nabla\Phi \text{, (a static electric field),}$$

the solution becomes

$$f_e^{1D}(z, w_z) = n_e(z_\infty)\exp\left(-\frac{w_z^2 - \frac{2e}{m_e}\left(\Phi(z) - \Phi(z_\infty)\right)}{v_{th}^2}\right) \quad [2.1-4]$$

$$= n_{e\infty}\exp\left(\frac{e\left(\Phi(z) - \Phi_\infty\right)}{T_e}\right)\exp\left(-\frac{w_z^2}{v_{th}^2}\right)$$

(the reference for the density and the potential is at the location where there is negligible perturbation from the probe, and the two quantities reach their constant unperturbed value).

We have assumed that the electron temperature has a negligible axial spatial variation as a result of the large electron thermal conductivity, and we have neglected any radial variation because of the small scale length $\approx mm$. With the above approximations for the electron distribution function, we have the electron density's and electron flux's dependence on the probe potential:

$$n_e(z) = n_{e\infty}\exp\left(\frac{\Phi(z)-\Phi_\infty}{T_e}\right) \Rightarrow$$

$$n_{e0} = n_{e\infty}\exp\left(\frac{\Phi_0-\Phi_\infty}{T_e}\right)$$

$$\Gamma(z) = n_e(z)u(z) = n_e(z)\left[\frac{v_{th}}{2\sqrt{\pi}}\exp\left(-\frac{\Phi(z)-\Phi_0}{T_e}\right)\right] :[2.1-5].$$

$$= \frac{n_{e\infty}v_{th}}{2\sqrt{\pi}}\exp\left(\frac{\Phi_0-\Phi_\infty}{T_e}\right) = n_{eo}\frac{v_{th}}{2\sqrt{\pi}} = \Gamma_0$$

We note that in obtaining the result of a constant flux, we have neglected the cross-field diffusion as well as the electron creation rate from ionization; to justify this neglect, we will compare the magnitudes of the contribution of diffusion and ionization with the contribution from the electron flux to the probe:

$$\nabla\cdot\vec{\Gamma} = n_e n_g K_{iz} \Rightarrow$$

$$\left(\Gamma_z^\infty - \Gamma_z^0\right)A_{probe} = \Gamma_r Per_{probe} l_{sheath} - n_e n_g K_{iz} Vol_{sheath}$$

$$\Gamma_{perp} \cong -D\nabla_{perp}(n) \approx -\nu_{ei} r_{larmor}^2 \frac{n}{R_{plasma}}$$

$$\nu_{ei} r_{larmor}^2 \approx .1 \rightarrow 1 m^2/s$$

$$R_{plasma} \approx .1m$$

$$n_e \approx 2\cdot 10^{18} m^{-3}$$

$$n_g \approx 5\cdot 10^{19} m^{-3}$$

$$Vol_{sheath} \cong A_{probe} l_{sheath} \approx \left(mm^2\right)(.1 \rightarrow 1mm)$$

$$Per_{probe} \approx r_{probe} \approx mm$$

$$K_{iz}\left(T_e \approx 5eV\right) \approx 5\cdot 10^{-15} m^3/s$$

With the above estimates,

$$\left|\frac{\Gamma_{perp} Per_{probe} l_{sheath}}{\left(\Gamma_z^0\right) A_{probe}}\right| \approx \frac{\left(1m^2/s\right)\left(2\cdot 10^{18} m^{-3}/.1m\right)\left(10^{-3} m\right)^2}{\left(2\cdot e^{-3}\cdot 10^{18} m^{-3}\right)\left(10^6 m/s\right)\left(10^{-3} m\right)^2} \approx 10^{-4} << 1$$

$$\left|\frac{n_e n_g K_{iz} Vol_{sheath}}{\left(\Gamma_z^0\right) A_{probe}}\right| \approx \frac{\left(2\cdot 10^{18} m^{-3}\right)\left(5\cdot 10^{19} m^{-3}\right)\left(5\cdot 10^{-15} m^3/s\right)\left(10^{-3} m\right)^3}{\left(2\cdot e^{-3}\cdot 10^{18} m^{-3}\right)\left(10^6 m/s\right)\left(10^{-3} m\right)^2} \approx 5\cdot 10^{-3} << 1$$

Hence, we are well justified in setting $\Gamma_z^{\infty} = \Gamma_z^0$.

We now will focus on the ion's contribution to the probe current. By estimating the magnitude of each term in equation 2.1-2 for the ion velocity distribution, we find:

$$\left|\frac{\nabla_{perp}\cdot\iint d^2 w_{perp}\vec{w}_{perp} f_i\left(\vec{r},\vec{w}\right)}{w_z\frac{\partial}{\partial z} f_i^{1D}\left(\vec{r},w_z\right)}\right| \approx \frac{u_i^{perp} f^{1D}/l_{sheath}}{u_i^z f^{1D}/l_{sheath}} = \frac{u_i^{perp}}{u_i^z} \approx \frac{D_{perp}\frac{1}{R_{plasma}}}{\sqrt{3T_e/m_i}} \approx \frac{\left(1m^2/s\right)\frac{1}{.1m}}{>5000 m/s} << 1$$

$$\left|\frac{\frac{e}{m_i}\left(E_z\left(\vec{r}\right)\right)\frac{\partial}{\partial w_z} f_i^{1D}\left(\vec{r},w_z\right)}{w_z\frac{\partial}{\partial z} f_i^{1D}\left(\vec{r},w_z\right)}\right| \approx \frac{\frac{e}{m_i}\left(\frac{3T_e}{e}\frac{1}{l_{sheath}}\right)\frac{f^{1D}}{v_{th}^{ion}}}{u_i^z f^{1D}/l_{sheath}} \approx \frac{u_i^z}{v_{th}^i} \approx \sqrt{\frac{T_e}{T_i}} \approx 3$$

$$\left|\frac{\iint d^2 w_{perp}\left(\hat{L}_{collision}^{op}\right)_i f_i\left(\vec{r},\vec{w}\right)}{w_z\frac{\partial}{\partial z} f_i^{1D}\left(\vec{r},w_z\right)}\right| \approx \frac{\nu_{in}}{u_i^z/l_{sheath}} \approx \frac{u_i^z/\lambda_{mfp}}{u_i^z/l_{sheath}} \approx \frac{1mm}{4cm} << 1$$

$$\left|\frac{\iint d^2 w_{perp}\left(\hat{L}_{ex,iz}^{op}\right)_i f_i\left(\vec{r},\vec{w}\right)}{w_z\frac{\partial}{\partial z} f_i^{1D}\left(\vec{r},w_z\right)}\right| \approx \frac{\nu_{iz}}{u_i^z/l_{sheath}} \approx \frac{n_g K_{iz}}{u_i^z/l_{sheath}} \approx \frac{25\cdot 10^4}{5\cdot 10^6} << 1$$

Physically, the above estimates reflect that the ion transit time through the sheath is much too quick for ionization and collisions to contribute.

With the above estimates, we are left with two terms, which must balance each other:

$$w_z \frac{\partial}{\partial z} f_i^{1D}(\vec{r}, w_z) + \frac{e}{m_i}\left(E_z(\vec{r})\right)\frac{\partial}{\partial w_z} f_i^{1D}(\vec{r}, w_z) \cong 0 : [2.1-6].$$

Note that the distribution is not Maxwellian. Before we take the zeroth and the first velocity moments of this equation, we would like an estimate of the ion random thermal energy relative to its directed kinetic energy through the sheath: $\frac{`T_i'}{T_e}$, the ion temperature is in quotes because we don't have a Maxwellian distribution. To obtain an estimate for this ratio, we need to compare the electron-ion energy equilibration time relative to the electron residence time (remember that the microwave power couples to the electron distribution; hence, the electrons gain the energy and then transfer it, via collisions, to the ions). The electron-ion energy equilibration time[2] for $T_e \cong 5eV, n_e \approx 10^{12} cm^{-3}$, assuming negligible relative drifts between the two species is $\approx 10m\,\text{sec}$; whereas, the residence time is $\approx \frac{L_{plasma}}{\Gamma/n} \approx \frac{.25m}{.01v_{th}^e} \approx 25\mu\,\text{sec}$; hence the electron leaves the plasma before it can transfer much of its energy to the ion, and we expect that the ion thermal energy is much less than the electron thermal energy. With this in mind, we can neglect the ion thermal energy relative to its directed kinetic energy when we take the first velocity moment. The zeroth and the first velocity moments of equation 2.1-6 yield the governing equations for the ion density and fluid velocity:

$$\frac{\partial}{\partial z} n_i u_i = 0$$
$$\left[m_i n_i u_i \frac{\partial}{\partial z} u_i = -e n_i \frac{\partial}{\partial z}\Phi \right] \Rightarrow \frac{\partial}{\partial z}\left(\frac{1}{2} m_i u_i^2 + e\Phi\right) = 0 \quad : [2.1-7]$$

[2] NRL Plasma Formulary

The approximation of a planar geometry is valid for the physics within the sheath because (as stated previously) the sheath thickness is much smaller than the characteristic probe size; however, as well be shown, the pre-sheath will extend far enough to render the probe geometry important. The modification from the probe geometry will be manifest in the particle conservation equation and in Poisson's equation for the potential because both these equations contain the divergence operator. In modifying the equations, we will switch to the local coordinate system of the probe

$$\left[\nabla_\rho \cdot\right] \Rightarrow \frac{1}{h(\rho)}\left[\frac{\partial}{\partial z} h(\rho)\right]$$

$$h_{cylindrical} = \rho; h_{spherical} = \rho^2$$

hence, the equation for the ion particle conservation is modified to

$$\frac{\partial}{\partial \rho}\left(h(\rho) n u\right) = 0 \Rightarrow hnu = Const = K: [2.1-8],$$

the energy equation becomes

$$\frac{1}{2} m_i u_i^2(\rho) = e\left(\Phi_\infty - \Phi(\rho)\right): [2.1-9],$$

where we have assumed that the ion energy outside the 'sheath' is negligible ('cold' ion assumption). Finally, Poisson's equation, which closes our system of equations for the ion density and fluid velocity, becomes

$$\nabla_z \cdot \left(\nabla_z \Phi\right) \Rightarrow \frac{1}{h(z)} \frac{\partial}{\partial z}\left(h(z)\left(\frac{\partial}{\partial z}\Phi\right)\right) = -\frac{e}{\varepsilon_0}\left(n_i - n_e\right): [2.1-10].$$

Note that the modifications from the probe geometry do not pertain to the electron equations because the electrons are restricted to move along the field lines.

We have justified neglecting ionization and elastic collisions within the 'sheath' (here the sheath represents not only the high electric field region adjacent to the probe, but the pre-sheath as well) by assuming that its thickness is small enough ($\approx mm$) to render the ion transit time short relative to the characteristic time for the collisions; however, we have not yet demonstrated the validity of the 'small sheath thickness' approximation. To estimate the 'sheath' thickness, we have to solve Poisson's equation for the potential variation:

$$\frac{1}{h}\frac{\partial}{\partial\rho}\left(h\left(\frac{\partial}{\partial\rho}\Phi\right)\right) = -\frac{e}{\varepsilon_0}\left(\frac{K}{hu} - n_{e\infty}\exp\left(e\left(\frac{\Phi-\Phi_\infty}{T_e}\right)\right)\right)$$

$$= -\frac{e}{\varepsilon_0}\left(\frac{K}{h\sqrt{\frac{2e}{m_i}\left(\Phi_\infty-\Phi\right)}} - n_{e\infty}\exp\left(e\left(\frac{\Phi-\Phi_\infty}{T_e}\right)\right)\right) \qquad :[2.1-11]$$

There are no analytic solutions to this equations; however, we can attempt an analysis[3] by observing two regions of opposite 'limits', and then matching their solutions at the boundary. The two regions are: the sheath, which is the region of high electric field adjacent to the probe where the electron density is negligible in comparison to the ion density because $n_i \propto \left(\Phi_\infty - \Phi\right)^{-1/2}$ and $n_e \propto \exp\left(\frac{\Phi-\Phi_\infty}{T_e}\right)$; and the pre-sheath, which is the region of quasi-neutrality where the electric field is 'small' ($\frac{n_i - n_e}{n_e} << 1 \Rightarrow \nabla^2\Phi \approx 0$). It can be shown that the sheath thickness is approximately several times the Debye length; therefore, the probe can be treated as a planar surface, implying that $h \cong const$. Hence, the equation within the sheath becomes

$$\Phi_{\rho\rho}^{sheath} \cong -\frac{e}{\varepsilon_0}\frac{K}{h}\left(\frac{2e}{m_i}\left(\Phi_\infty - \Phi\right)\right)^{-1/2} : [2.1-12],$$

and the equation for the quasi-neutral region where $h \neq const$ becomes

$$\frac{K}{h(\rho)\sqrt{\frac{2e}{m_i}\left(\Phi_\infty - \Phi\right)}} - n_{e\infty}\exp\left(e\left(\frac{\Phi - \Phi_\infty}{T_e}\right)\right) \cong 0 : [2.1-13];$$

hence, even though the electron and the ion density are set equal, the potential is not constant and an electric field does exist. This solution for the quasi-neutral region is possible because the ion collection area for a cylindrical or a spherical geometry varies with distance from the probe (or equivalently $h = h(\rho)$); however, if the geometry were planar or the ions 'magnetized' (such that their motion was restricted to one dimension), then the above equation would have no solution, and we would have to correct our assumption of a constant ion current to the probe by including the effects of ionization and diffusion in the quasi-neutral region.

Before we discuss the solutions for the potential in the two regions, we will find it convenient to determine the criterion for matching the solutions at the boundary of the two region. We will take the ion and electron densities to be equal up to the boundary:

$$n_{ib} \cong n_{eb} = n_b = n_{e\infty}\exp\left(e\frac{\Phi_b - \Phi_\infty}{T_e}\right) : [2.1-14],$$

and

$$\begin{aligned} h(\rho) &\cong h(\rho_b) \\ K &= hn_i u_i = h_b n_{ib} u_{ib} \end{aligned};$$

---

[3] I. H. Hutchinson, Principles of Plasma Diagnostics, 1987, Chp. 3

hence, Poisson's equation becomes

$$\Phi_{\rho\rho} \cong -\frac{e}{\varepsilon_0} n_b \left(\left(\sqrt{\frac{\Phi_\infty - \Phi_b}{\Phi_\infty - \Phi}} \right) - \exp\left(e \frac{\Phi - \Phi_b}{T_e} \right) \right) : [2.1-15],$$

Near the sheath, the quantity

$$\eta \equiv \frac{e\left(\Phi - \Phi_b\right)}{T_e} << 1,$$

and we can Taylor expand about $\eta = 0$, to obtain a tractable solution near the sheath. If we define

$$\eta_\infty \equiv \frac{e\left(\Phi_\infty - \Phi_b\right)}{T_e}$$

$$\beta \equiv \frac{\rho}{\lambda_D}; \lambda_D \equiv \frac{\varepsilon_0 T_e}{e^2 n_{e\infty}},$$

and carry out the expansion, we will obtain

$$\eta_{\beta\beta} + \alpha^2 \eta \cong 0$$

$$\alpha^2 \equiv \exp\left(-\eta_\infty\right)\left(-1 + \frac{1}{2\eta_\infty}\right) : [2.1-16].$$

Depending on the sign of α^2, this differential equation 2.1-16 will either have a sinusoidal or an exponential solution; to satisfy the boundary condition, the solution to this equation must be exponentially decaying, implying that

$$\alpha^2 \leq 0 \Rightarrow \eta_\infty \geq \frac{1}{2}.$$

Now, if we differentiate the equation describing the quasi-neutral region, we will find that

$$\chi \equiv \frac{e\left(\Phi_\infty - \Phi\right)}{T_e}$$

$$\frac{d\chi}{d\rho} \propto -\left(\frac{1}{2}\chi^{-1/2} - \chi^{1/2}\right)^{-1}$$

As we move away from the unperturbed region towards the sheath, the equation for the quasi-neutral region states that χ becomes progressively larger until it reaches the value of $1/2$, where $\frac{d\chi}{d\rho}$ or equivalently the electric field becomes infinite; hence, the assumption of a small electric field breaks down and the sheath forms at or before this point:

$$\chi_b = \eta_b \leq 1/2 .$$

The two criterion for η_b can be satisfied simultaneously if we set

$$\eta_b = 1/2 ;$$

this is the Bohm sheath criteria, which determines the potential, the density and the ion velocity at the sheath boundary. The potential and the ion velocity at the sheath boundary become

$$\Phi_\infty - \Phi_b = \frac{T_e}{2e}$$

$$n_{ib} = n_{eb} = n_{e\infty} \exp\left(-1/2\right) \qquad :[2.1-17],$$

$$u_{ib} = \sqrt{\frac{2e}{m_i}\left(\Phi_\infty - \Phi_b\right)} = \sqrt{\frac{T_e}{m_i}}$$

and the ion saturation current density at the probe becomes

$$J_i^{probe} = e\frac{K}{h_p} = e\frac{h_b n_{ib} u_{ib}}{h_p} = e\frac{h_b}{h_p}\sqrt{\frac{T_e}{m_i}} n_{e\infty} \exp\left(-1/2\right) :[2.1-18].$$

With the boundary values for the potential, density, and ion velocity established, we will discuss the solutions for the potential in the separate regions.

The equation within the sheath with $\chi \equiv \frac{e(\Phi_\infty - \Phi)}{T_e}$,

$$\chi_{\beta\beta} = \sqrt{2}\exp(-1/2)\chi^{-1/2} \cong 0.86\chi^{-1/2} : [2.1-19],$$

can be solved analytically by multiplying both sides by χ_β and integrating:

$$\frac{1}{2}\left((\chi_\beta)^2 - (\chi_\beta)_b^{\,2}\right) = 0.86\left(\sqrt{\chi} - \sqrt{(\chi)_b}\right);$$

note that $\chi_\beta \equiv \frac{d\chi}{d\beta}$ and $(\chi)_b \equiv \chi(\beta_b) = \chi(\rho_b/\lambda_D)$. We will set $(\chi_\beta)_b \approx 0$, thereby neglecting the electric field at the sheath boundary, and integrate once more to obtain:

$$1.3(\beta_b - \beta) = \int_{\chi_b}^{\chi} \frac{d\chi}{\sqrt{\left[\sqrt{\chi} - \sqrt{(\chi)_b}\right]}} = 2\int_0^{\sqrt{\chi}-\sqrt{(\chi)_b}} dU\left(\sqrt{U} + \frac{\sqrt{(\chi)_b}}{\sqrt{U}}\right)$$

$$= \frac{4}{3}\left[\sqrt{\chi} - \sqrt{(\chi)_b}\right]^{1/2}\left[\sqrt{\chi} + 2\sqrt{(\chi)_b}\right]; \qquad :[2.1-20].$$

$$(\chi)_b = e\frac{\Phi_\infty - \Phi_b}{T_e} = \frac{1}{2}$$

The sheath thickness (up to the boundary) becomes

$$\delta_{sheath} = \lambda_D(\beta_b - \beta_0) = \left\{\sqrt{\left[\sqrt{\chi_0} - \sqrt{1/2}\right]}\left[\sqrt{\chi_0} + 2\sqrt{1/2}\right]\right\}\lambda_D \qquad :[2.1-21].$$

$$\chi_0 = e\frac{\Phi_\infty - \Phi_0}{T_e}$$

Remember that our formula is valid for $(\delta_{sheath}/l_{probe}) << 1$; otherwise, the assumption $h \cong const$ would be violated. Typically, when obtaining the I-V characteristic, we begin at a voltage that is sufficiently negative to obtain the ion saturation current and then increase it to the plasma potential (at which point all of the incoming electron flux is collected, and

the electron current density contribution becomes $e\frac{n_{e\infty}v_{th}}{2\sqrt{\pi}}$) to obtain the electron saturation current. The lower limit on the voltage is determined by first locating the floating potential, the potential at which no current is drawn and then decreasing the probe potential to a sufficiently negative value to be rid of the remaining electron contribution $\exp\left(e\frac{\Phi_0-\Phi_{float}}{T_e}\right)\le 0.01 \Rightarrow \Phi_0-\Phi_{float}\le -23V$; typically, the floating potential is near the ground potential; hence, we need $\Phi_0 \cong -30V$ to guarantee ion saturation current. To obtain the electron saturation current, we need to obtain the plasma potential relative to the floating potential. For a Maxwellian electron distribution, this potential can easily be determined by setting our expression for the electron current equal to the ion saturation current:

$$e\frac{n_{e\infty}v_{th}}{2\sqrt{\pi}}\exp\left(\frac{\Phi_{float}-\Phi_\infty}{T_e}\right)\left\langle \vec{A}_{probe}\cdot\hat{B}\right\rangle = en_{e\infty}\exp(-1/2)\sqrt{\frac{eT_e}{m_i}}A_{probe}:[2.1-22],$$

We have taken the effective electron collection area as the component of the probe surface normal that is along the magnetic field and have assumed that the sheath thickness at the floating point is not large enough to render a significant difference between the ion collection area at the sheath boundary (which is the area that should be used in the above equation) and the probe area. For a cylindrical probe, the ratio of the ion to the electron collection area is $\approx \pi$, and for a probe shape that can be approximated as a half-sphere, the ratio is ≈ 2. Using the estimates for the ratio of the collection areas, we obtain,

$$\Phi_\infty-\Phi_{float}=\frac{T_e}{e}\chi_{float}=\frac{1}{2}\left[\ln\left(\frac{m_i}{2\pi(4\to 10)m_e}\right)+1\right]\cong(4\to 4.5)\frac{T_e}{e}:[2.1-23],$$

for the value of the potential drop through the 'sheath' at a floating surface; therefore, for $T_e \cong 5eV$, $\Phi_\infty - \Phi_{float} \cong +20V$, and for $\Phi_{float} \cong 0$, $\Phi_\infty \cong +20V$. Hence, we only need to sweep the voltage from $-30V$ to $20V$. In this voltage regime,

$0 \le \chi_0 = e\dfrac{\Phi_\infty - \Phi_0}{T_e} \le 10$, and the maximum sheath thickness for

$n_e \approx 10^{12} cm^{-3}, T_e \cong 5eV$ becomes $\cong 7\lambda_D \approx 70\mu m$; hence,

$\left(\delta_{sheath}/l_{probe}\right) \cong \dfrac{70\mu m}{1mm} = 0.07 << 1$, and our approximation that $h \cong const$ is valid.

We still need to determine the thickness of the pre-sheath to validate our analysis (remember that we have assumed a 'sheath' (sheath + pre-sheath) thickness of $\approx mm$). To determine the pre-sheath thickness, we will examine the equation for the potential variation in the quasi-neutral region:

$$\sqrt{\chi}\exp(-\chi) = \frac{\exp(-1/2)}{\sqrt{2}}\frac{h(\rho_b)}{h(\rho)} : [2.1-24];$$

we will define the pre-sheath thickness as the value of $\delta_{pre-sheath} = \rho_{pre} - \rho_b$ such that the difference between the potential at ρ_{pre} and that at ρ_∞ is equal to $1\% T_e$; hence, ρ_{pre} is the radius at which $\chi = \chi_p = 0.01$:

$$\frac{h(\rho_{pre})}{h(\rho_b)} = 4.33;$$

for a cylindrical probe,

$$h(\rho) = \rho \Rightarrow \delta_{pre-sheath} = 3.33\rho_b \cong 3.33\left(r_{probe} + \delta_{sheath}\right) \approx 3.5mm;$$

and for a spherical probe,

$$h(\rho) = \rho^2 \Rightarrow \delta_{pre-sheath} = \left(\sqrt{4.33} - 1\right)\rho_b \cong 1.1\left(r_{probe} + \delta_{sheath}\right) \approx 1.2mm;$$

hence, the pre-sheath thickness is much large than the sheath, and it is of order mm, thereby validating our analysis. Now ,we will summarize the results:

$$\left|I_{si}(V)\right| = e\exp(-1/2)n_{e\infty}\sqrt{\frac{eT_e}{m_i}}\frac{h_b(V)}{h_{probe}}A_{probe}$$

$$\left|I_{se}\right| = en_{e\infty}\sqrt{\frac{eT_e}{2\pi m_e}}\left\langle \vec{A}_{probe}\cdot\hat{B}\right\rangle$$

$$I(V) = \left|I_{se}\right|\exp\left(\frac{e(V-\Phi_\infty)}{T_e}\right) - \left|I_{si}(V)\right| \Rightarrow \qquad :[2.1-25];$$

$$T_e = e\left[\frac{d}{dV}\ln\left(I + \left|I_{si}\right|\right)\right]^{-1}$$

In general, the points in the I-V characteristic that are used to determine the electron temperature are such that $\left|\frac{d}{dV}I\right| >> \left|\frac{d}{dV}\left|I_{si}\right|\right|$; hence, we neglect I_{si}'s contribution to the measurement of the electron temperature.

The above analysis can easily be extended to two singly charged ion species. The addition of a second ion species does not change the boundary condition; hence, the electron temperature analysis does not change, and the ion saturation current becomes the sum of the saturation currents of the two species. Each species will reach its Bohm speed at the boundary, $\sqrt{T_e/m_j}$, and because the total current to the probe for each species is a constant of the radial position:

$$n_{jb}u_{jb}h_b = n_j u_j h \Rightarrow$$

$$\frac{n_{1b}}{n_1} = \frac{u_1}{u_{1b}} = \sqrt{\frac{\Delta\Phi}{T_e}} = \frac{n_{2b}}{n_2} \Rightarrow$$

$$\left|\frac{I_{si2}}{I_{si1}}\right| = \frac{n_{2b}u_{2b}h_b}{n_{1b}u_{1b}h_b} = \frac{n_{2\infty}}{n_{1\infty}}\sqrt{\frac{m_1}{m_2}} \Rightarrow :[2.1-26],$$

$$\left|I_{si}\right| = \left(1+\frac{n_{2\infty}}{n_{1\infty}}\sqrt{\frac{m_1}{m_2}}\right)\left|I_{si1}\right|$$

$$n_{e\infty} = n_{1\infty} + n_{2\infty}$$

The modification to the 'sheath drop' potential drop becomes:

$$\Phi_\infty - \Phi_{float} = \frac{T_e}{e}\chi_{float} = \frac{1}{2}\frac{T_e}{e}\left[\ln\left(\frac{m_1}{2\pi(4\to 10)m_e}\left(\frac{1+\frac{n_{2\infty}}{n_{1\infty}}}{1+\frac{n_{2\infty}}{n_{1\infty}}\sqrt{\frac{m_1}{m_2}}}\right)^2\right)+1\right] :[2.1-27],$$

and is quite negligible for $m_1 \approx m_2$; there are no modifications to the pre-sheath analysis.

Conventionally, we obtain the electron temperature from the $\ln(I)-V$ plot and the 'sheath' potential drop from the I-V plot by associating the value of Φ_∞ with the voltage that corresponds with the 'knee' near the electron saturation region and Φ_{float}, by definition, with the voltage that corresponds to no net current (the electron current never saturates because of the probe edges' contribution to the increase in the collection area). Presuming that we have an accurate estimate of the magnetic field's modification of the electron collection area, a comparison of the measured 'sheath drop' potential with the one calculated by our formula will serve as a feed-back on our assumption of a Maxwellian electron distribution; moreover, a smaller measured 'sheath' potential drop, which is the case, will indicate a depleted 'high' energy tail. The electron density, in principle, can be estimated either from the ion or the electron saturation current; however,

the saturation current measurements that we have made with a spherical probe contained systematic errors as a result of a continual increase in the collection area from copper deposition when we were operating with the copper target 'on' (which created a conducting path between the probe tip and the surrounding conducting bodies); in fact, the probe eventually 'shorted'. Fortunately, even though our knowledge of the collection area was uncertain, for our measurements in a pure argon plasma, the rate of change of the current with voltage (which determines the electron temperature) was not affected. There were, however, systematic errors in the measured electron temperature from hysteresis in the I-V trace. The hysteresis resulted from the change in the surface work function[4] as the surface impurity concentration (namely oxygen) was depleted with increasing probe voltage via probe temperature rise from the increase in the incident electron heat flux ($q_e(V) \approx 2T_e|I_e(V)|$). This hysteresis could have been eliminated if the probe surface were initially biased near the plasma potential so that the intense electron heat flux would raise the probe temperature sufficiently to fully deplete the surface impurity concentration. The origin of the hysteresis was not known at the time of the measurement; however, we naively did eliminate the hysteresis by repeating each trace a few times. Another source of error in the electron temperature measurements was the plasma oscillations, which became prominent for microwave powers exceeding $3kW$. The contribution of the above mentioned sources resulted in relative errors in T_e of approximately 20% (or equivalently $\delta T_e \approx 0.2(\approx 5eV) = 1eV$).

[4] Auciello and Flamm, Plasma Diagnostics, 1989, p. 171

Measurements of the electron temperature near ($R = 0, Z = 9''$, where the axial position is measured with respect to the location of the copper target) were made for various microwave powers, argon pressures, electro-magnet current settings, and two target voltage settings (off: pure argon plasma; on at $-1kV$: a copper/argon plasma) with the following results:

FIGURES 2.1-1,2: THE VARIATION OF ELECTRON TEMPERATURE AND SHEATH POTENTIAL DROP WITH ARGON PRESSURE FOR TWO MICROWAVE POWER SETTINGS.

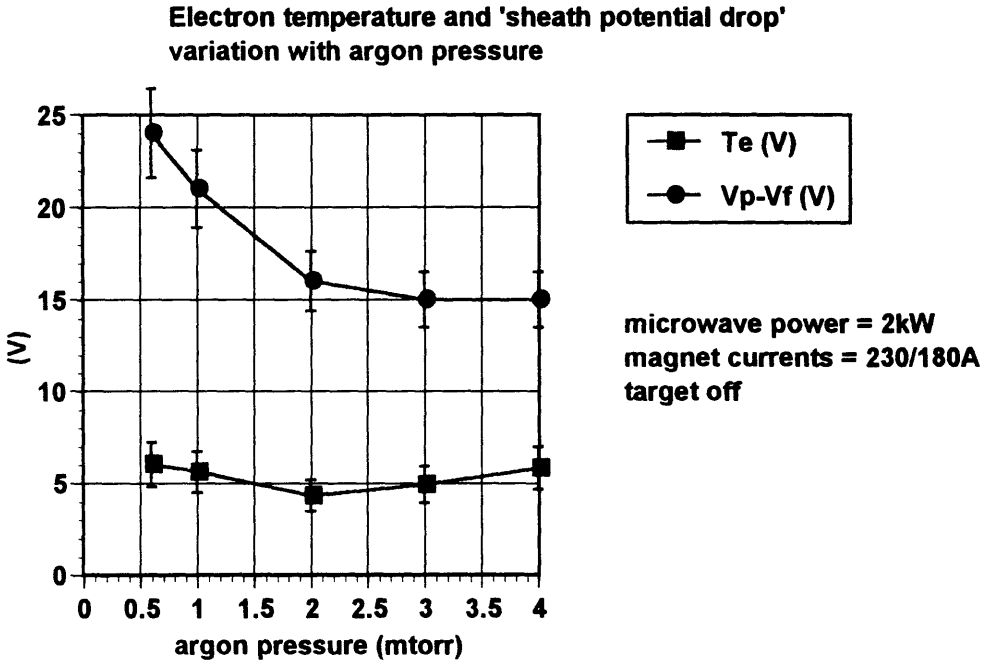

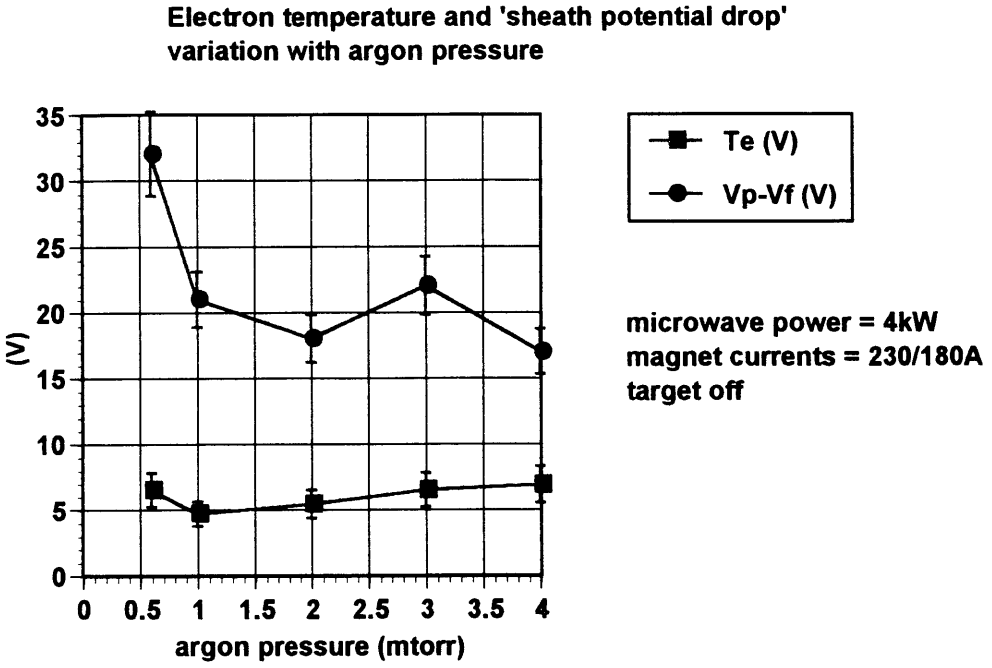

FIGURES 2.1-3,4: THE VARIATION OF ELECTRON TEMPERATURE AND SHEATH POTENTIAL DROP WITH MICROWAVE POWER FOR TWO ARGON PRESSURES.

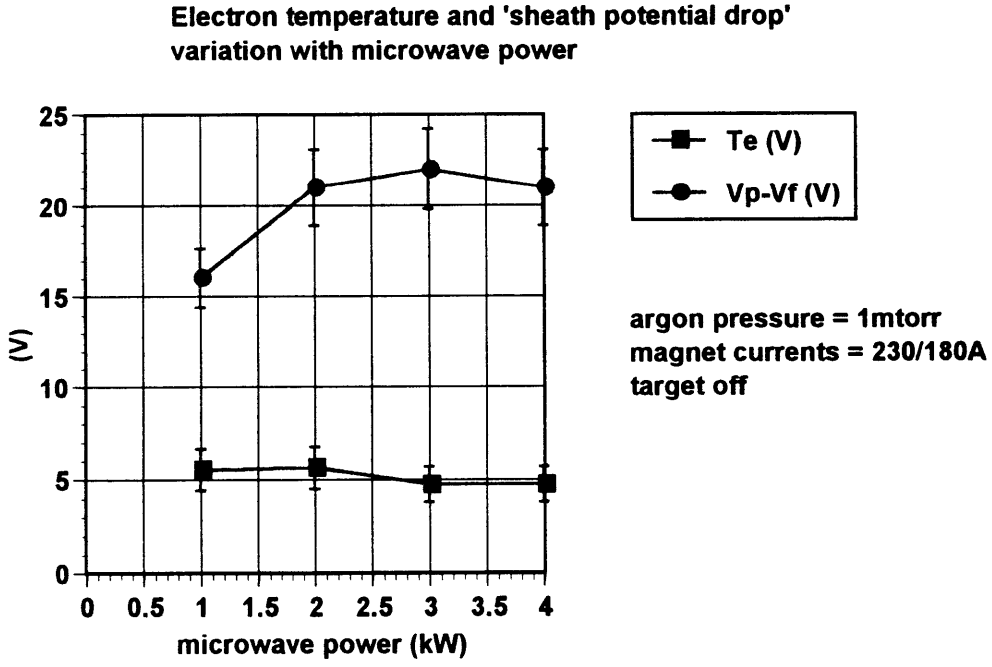

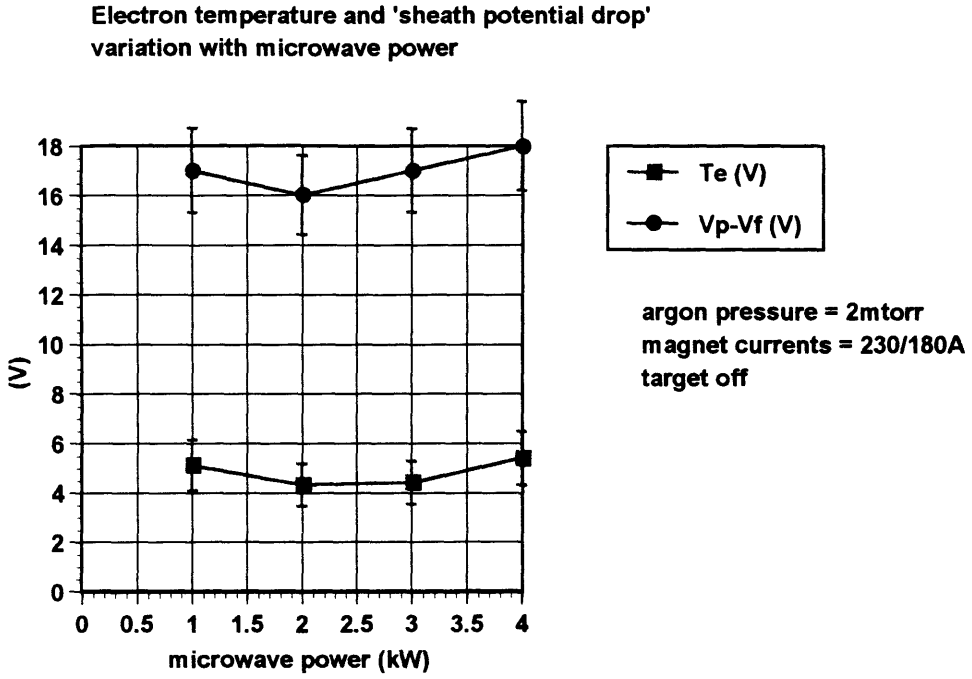

FIGURES 2.1-1,2: THE VARIATION OF ELECTRON TEMPERATURE AND SHEATH POTENTIAL DROP WITH ARGON PRESSURE FOR TWO MICROWAVE POWER SETTINGS WITH A DIFFERENT ELECTRO-MAGNET CURRENT SETTING..

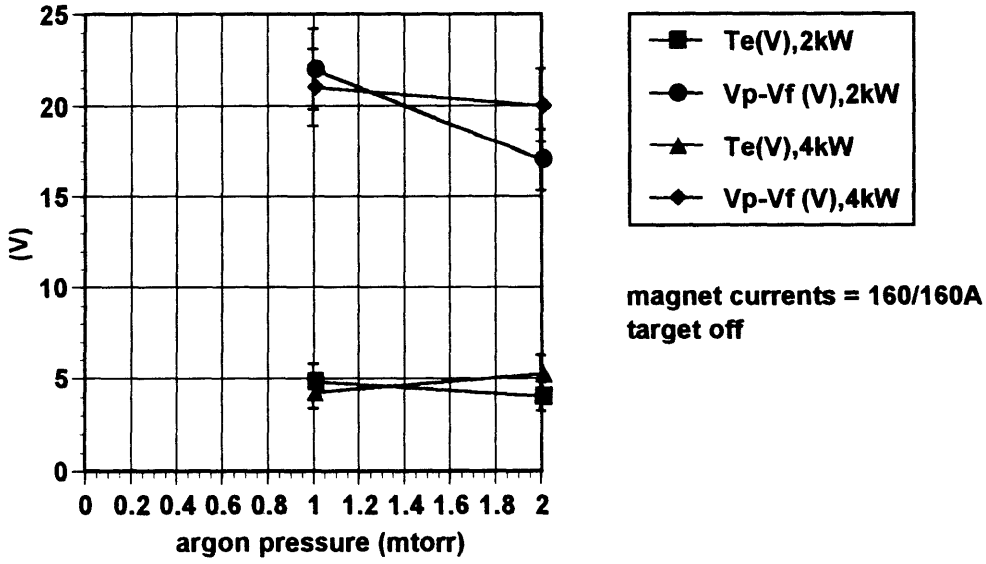

As shown by these figures, the electron temperature at ($R \approx 0, Z \approx 9''$) lies between $4 \rightarrow 7eV$. We have not shown the variation of the electron temperature with electro-magnet current settings or with the addition of copper to the plasma via the biasing of the copper target because there are no noticeable changes to T_e with these parameters. Because we only measured the electron temperature at one location, we can not compare our results with the global model presented in the earlier section; why? The electron temperature not only has a non-constant radial profile, but the profile varies with power and pressure. The temperature profile and its variation are a function of

1. microwave propagation and absorption, which is controlled by the microwave launching configuration, the chamber geometry, gas pressure, and the temperature profile itself,
2. radial and axial conduction of the absorbed power, which is controlled by the temperature profile and gas density.

Hence, even though the global model predicts a decrease in T_e with increasing gas pressure, the trend observed with increasing gas pressure (which is an initial decrease in T_e followed by an increase) can be attributed to a redistribution of power absorption towards preferential heating of the chamber center. Unfortunately, we don't have the data to justify this claim; however, Dr. Xing Chen at Astex has measured the radial density and temperature profile and its variation with microwave power by using a cylindrical probe. Before we examine Dr. Chen's results, we will examine one 'local' trend that is apparent from our local T_e measurements: the variation with gas pressure of the ratio of the 'sheath drop' potential to the electron temperature. This ratio should remain constant and equal to ≈ 4.5 for a Maxwellian distribution; however, the ratio decreases with increasing argon

pressure. This decrease results from the increase in the argon atom density: the increased atom density increases the ionization and excitation collision rates, experienced by the electrons in the 'high' energy tail of the distribution; the increased collision rates deplete the 'high' energy tail. With fewer 'high' energy electrons, the potential drop in the 'sheath' does not need to be as large as for a Maxwellian electron distribution to repel the electrons to create a floating surface. From the above figures, we see that this ratio for argon pressures below $1mtorr$ is essentially what we have calculated; however, above $1mtorr$,

$$\frac{(\Delta\Phi)_{'sheath'}^{observed}}{T_e} \leq 3,$$

thereby demonstrating the deviation from a Maxwellian distribution. The variation of this ratio with microwave power is noticeable for 'low' pressures, $1mtorr$: the ratio increases from a value of ≈ 3 at $1kW$ to the value expected of a Maxwellian distribution of $\cong 4$ for powers $\geq 2kW$. This trend can be attributed to the increase in the number of 'high' energy electrons resulting from the increased power. For 'higher' pressures, $2mtorr$, the ratio is ≈ 3.5 (below what is expected of a Maxwellian distribution) and does not vary with increased power; an indication that the increased rate at which the 'high' energy tail is depleted far exceeds the rate at which it is replenished from the increased power.

We have not shown the results for the electron density because, as stated previously, the measured density is inversely proportional to the collection area whose value is uncertain. However, we will note that measurements of the electron saturation current ($|I_{se}| \propto n_e\sqrt{T_e}$) indicated that the current had a 2 to 3 fold increase with increasing microwave power of 1 to $4kW$ and a 2 to 3 fold decrease with increasing

pressure of 0.06 to 4*mtorr*, which is consistent with the 'zeroth order' global prediction: $n_e \propto \frac{P_{\mu wave}}{n_g}$; but we must take caution in interpreting these results because

a) the collection area did gradually change over time, and

b) these are 'local' measurements; therefore, they do not account for any variation in the density profile.

As stated above, a comparison of our measurements with the predictions of the global model requires a measurement of the temperature and density profiles; therefore, we, now, will focus on Dr. Xing's results of the measured radial temperature and density profiles for two microwave power settings.

FIGURE 2.1-6,7: THE RADIAL PROFILE OF THE ELECTRON TEMPERATURE, THE PLASMA POTENTIAL AND THE FLOEATING POTENTIAL FOR TWO POWER SETTINGS.

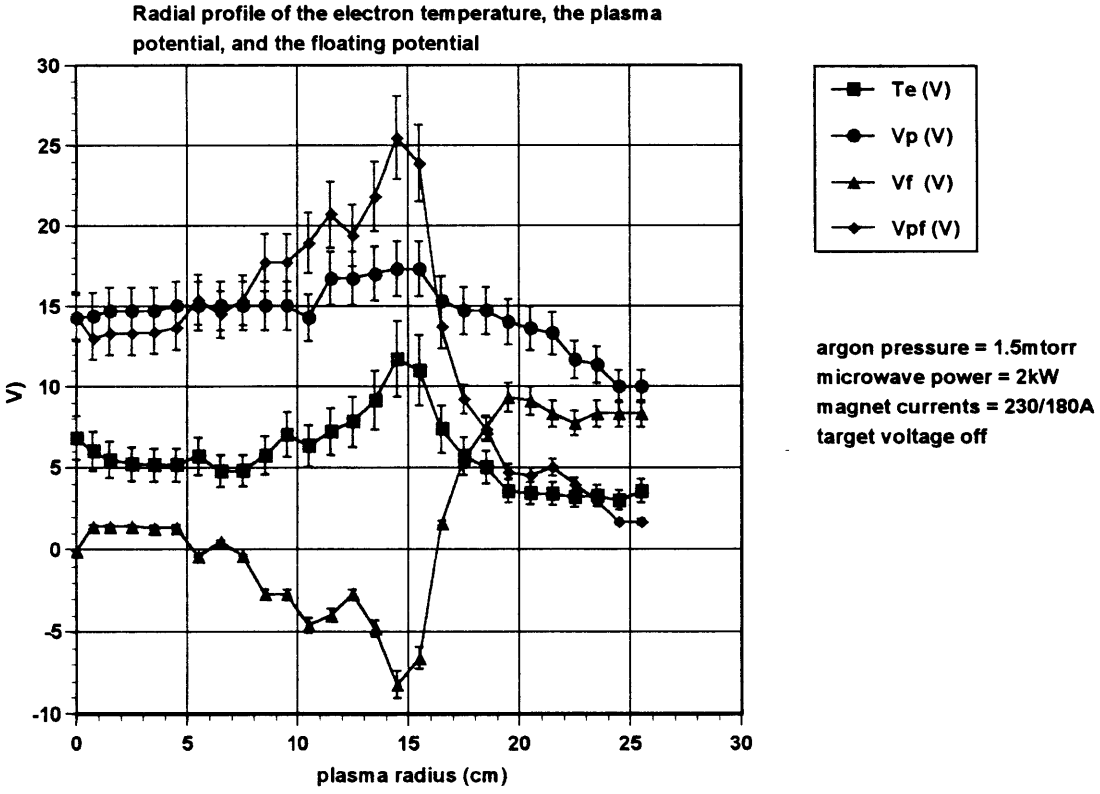

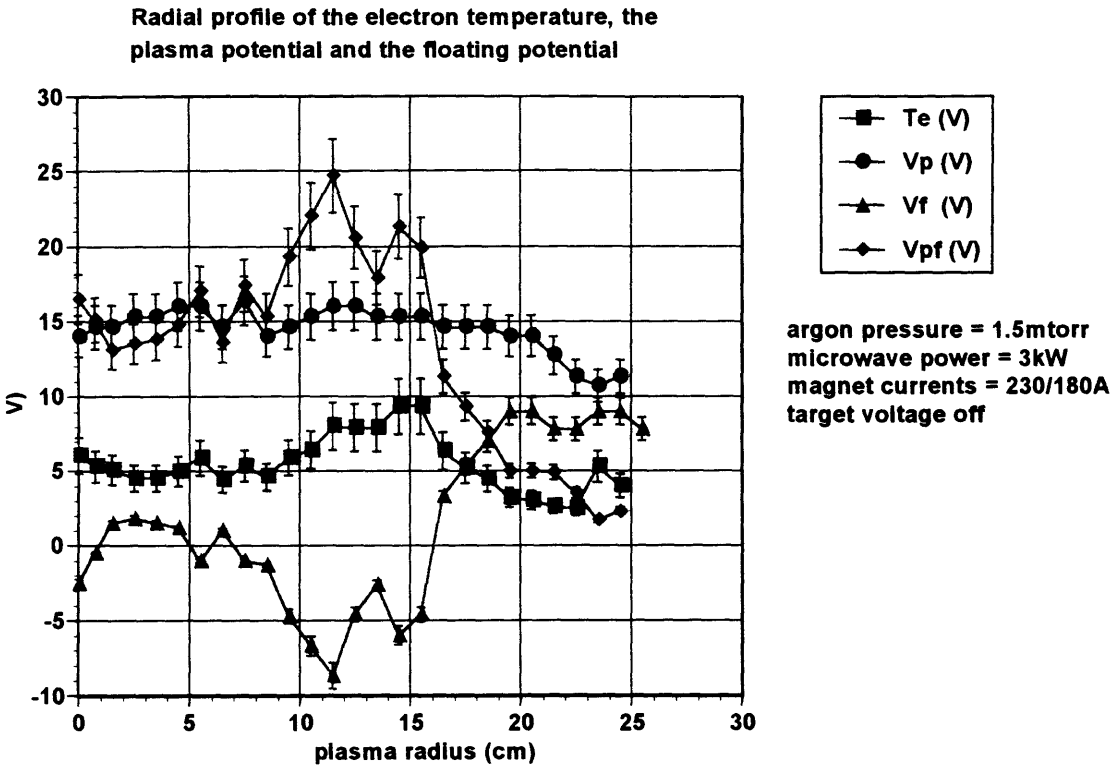

FIGURE 2.1-8: THE RADIAL ELECTRON DENSITY PROFILE FOR TWO POWER SETTINGS.

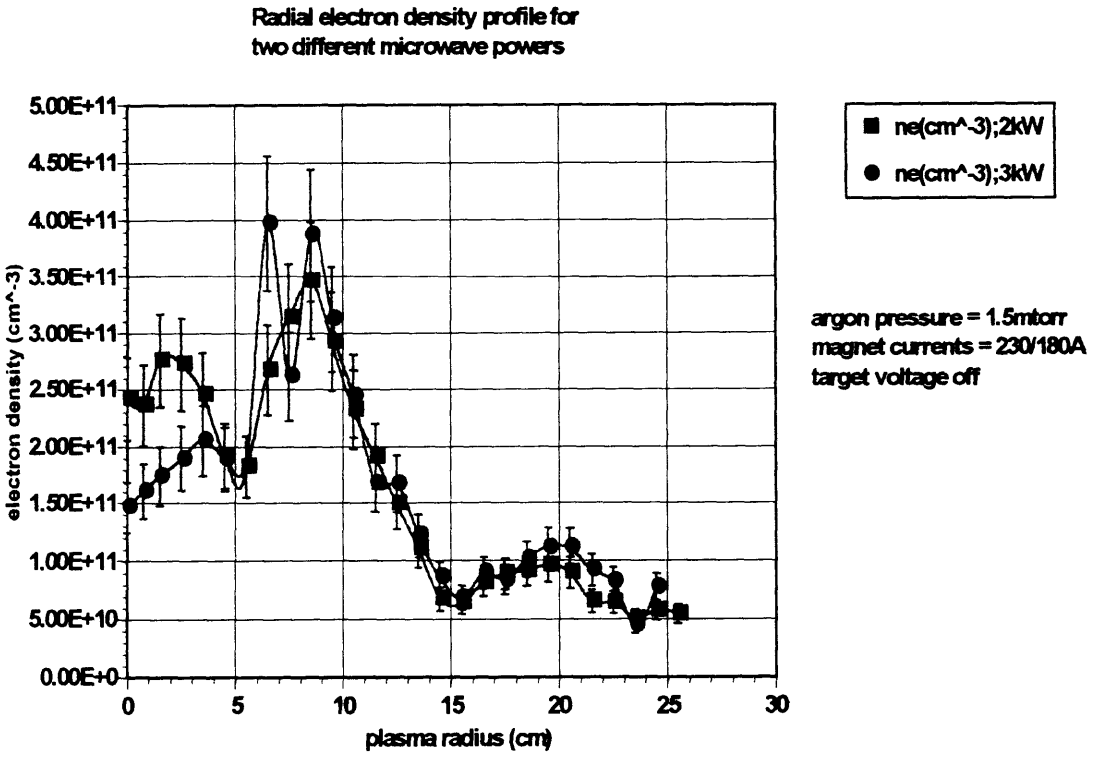

Figures 2.1-6,7,8 show that the temperature and density profiles are peaked at radial positions of 10 to 15 cm and 6 to 9 cm from the axis respectively. Also note that the peaks in density are accompanied by peaks in the ratio of $\Phi_{'sheath'}/T_e$, an indication that the greater absorbed power in these regions has led to a larger 'high' energy electron population). Although, we can not say much about the profiles without a detailed calculation of wave propagation and absorption accompanied by an analysis of the fluid equations, we can say that the off-center peaks might hint that the preferential path for the wave propagation is along the cylindrical surface of the top cavity (which is located at $R \cong 6cm; 0cm \le Z \le 13cm$, where the target is located at $Z = 0$) as opposed to propagation through the bulk plasma. 'Surface' waves are treated by Liebermann[5]. Dr. Xing's results also show that the plasma potential is relatively constant near the axis, rendering the radial electric field near the axis negligible; however, the potential begins to drop near the edge (an indication of the violation of quasi-neutrality).

Using the reaction rates for excitation and ionization of an argon plasma found in Liebermann[6], the zero-dimensional model presented in section 1.0, predicts an electron temperature and density of $4eV$ and $10^{11} cm^{-3}$; an excellent prediction considering that the model is crude.

---

[5] Liebermann and Lichtenberg, Principles of Plasma Discharges and Materials Processing, 1994, Chp. 13
[6] Liebermann and Lichtenberg, Principles of Plasma Discharges and Materials Processing, 1994, Chp. 3

2.2: MEASUREMENT OF THE COPPER ION-TO-ARGON ION FRACTION AT THE SUBSTRATE:

$$f^{sub}_{Cu^+/Ar^+} \equiv \left[\frac{\Gamma_{Cu^+}}{\Gamma_{Cu^+} + \Gamma_{Ar^+}}\right]_{substrate}$$

Γ_j denotes the flux of species 'j'

Information about $f^{sub}_{Cu^+/Ar^+}$ was crucial in the attempt to understand the argon ions' influence on the fill evolution. We knew that the argon ions could do nothing but sputter the deposited copper, and based on our model for a successful fill, we would have liked to minimize such sputtering; hence, we needed to observe the fill quality as we varied this parameter. The knowledge of this parameter requires its measurement; therefore, we, now, will discuss our method for measuring $f^{sub}_{Cu^+/Ar^+}$:

The measurement requires the use of a very thin sheet of copper (if we had a mixture of aluminum and argon instead, we would use a piece of aluminum). We would like the piece to be thin so that we could detect the change in its weight from etching and deposition with a micro-balance (the weight change is typically $\approx 1 \rightarrow 10mg$). The piece is biased to a known potential to obtain ion saturation current (the biased used in our experiment was $\cong -90V$); the current measured, corrected for secondary electron emission, then, yields the sum of the rates of the copper and argon ions incident on the piece. With the 'sheath drop' potential known from the Langmuir probe measurements and the floating potential measured, we have the total potential drop through the 'sheath': $\Delta V = \left(\Phi_\infty - \Phi_{float}\right) + \left(\Phi_{float} - V_{bias}\right)$. If we neglect any acceleration resulting from axial

potential variations within the bulk plasma and neglect the copper ions' directed energy when sputtered from the target (the directed energy can be neglected if the mean-free-path for copper-argon collisions is small with respect to the target-substrate distance), then the incident energy of the argon and copper ions at the piece will be $\cong e\Delta V$ (note that we have neglected the contribution from doubly ionized ions; even though each doubly ionized ion contributes $2\sqrt{2}$ -fold [note that $I_{si} \propto q\sqrt{q\frac{T_e}{m_i}}n_{e\infty} \Rightarrow I_{si} \propto Z\sqrt{Z}$] to the current relative to a singly ionized ion, the density of doubly ionized ions relative to singly ionized ions is less than 1%; the inclusion of doubly ionized ions in the analysis would decrease the total number of ions incident on the piece because each doubly ionized ion contributes two-fold to the current, hence, the total number of particles incident will be less than what the current indicates; however, doubly ionized ions have an incident energy that is twice that of the singly ionized ions, therefore, the doubly ionized ions sputter more copper than the singly ionized ions; the two corrections that would result from the inclusion of doubly ionized ions will attempt to cancel one another, thereby, rendering the contribution from doubly ionized ions even more negligible). The incident energy corresponds to a particular sputtering coefficient for each ion species (the copper ions stick as well as sputter; hence the coefficient for the copper ions, which is defined as the self-sputtering coefficient, is the difference between the sputtering and the sticking coefficient, which is experimentally measured as one coefficient because the two processes are difficult to measure separately). The copper as well as the argon neutrals do not gain sufficient energy to sputter (the sputtering threshold is $\approx 25eV$ [1], an energy that incident

[1] Robley V. Stuart and Gottfried K. Wehner, Phys. Rev. Lett. **4 #8**, pp.409-410 (4/15/1960)

neutrals can not reach even if they originated from ions via charge exchange reactions [recombination rates are negligible]: note that the sheath thickness [where most of the energy drop occurs] is $\approx 100\mu m$ and the mean-free-path for charge exchange and ionization collisions[2] is $\approx 5cm$; hence, negligible number of ions will have energies substantially less than $e\Delta V$ [from neutrals being ionized within the sheath and not being able to accelerate to the energy corresponding to the full potential drop] and negligible number of neutrals will gain energies sufficient to sputter [from charge exchange reactions that would create 'fast' neutrals within the sheath]). Of course the pre-sheath thickness for a flat piece of copper can extend to a few cm's and the charge exchange and ionization collisions can contribute significantly; however, the pre-sheath potential drop is $\approx T_e/2e \approx 3V$, therefore, the ions that originate within the pre-sheath from the ionization of or charge exchange with neutrals will almost gain the entire energy of $e\Delta V \approx (90+20)eV$, and the neutrals that originate from the ions via charge exchange reactions will have an energy gain of at most $\approx T_e/2e \approx 3V$, much less than the threshold for sputtering). Therefore, the copper neutrals can only bounce or stick. Data for the self-sputtering coefficient for copper[3] ($ST_{Cu/Cu} \equiv (S-T)_{Cu/Cu}$; where $T_{Cu/Cu}$ denotes the sticking coefficient) indicates that below $40eV$, $ST_{Cu/Cu} \cong -1$, thereby implying that the copper neutrals stick with a 100% probability (no bouncing), $T_{Cu^0/Cu} \cong 1$. With the above information regarding the weight change of our piece, the current incident on our piece, and the incident energy of the ions and their corresponding sputtering coefficients, we can construct one equation with two unknowns: f_{Cu^+/Ar^+}, f_{Cu^+/Cu^0}; the copper-to-

[2] Liebermann and Lichtenberg, Principles of Plasma Discharges and Materials Processing, 1994, Chp. 3

argon ion fraction, and the copper ion-to-neutral fraction. To solve for f_{Cu^+/Ar^+}, we will need information about f_{Cu^+/Cu^0}. We will assume that $f_{Cu^+/Cu^0} \cong 1$ (100% ionized copper flux) to obtain $\left[f_{Cu^+/Ar^+}\right]_{\max}$, where $f_{Cu^+/Ar^+} \leq \left[f_{Cu^+/Ar^+}\right]_{\max}$ and the equality holds if $f_{Cu^+/Cu^0} = 1$; we will show later in our analysis of f_{Cu^+/Cu^0} that this fraction is $\geq 90\%$, thereby establishing that $f_{Cu^+/Ar^+} \cong \left[f_{Cu^+/Ar^+}\right]_{\max}$.

Before we discuss the equations and the measurements of $\left[f_{Cu^+/Ar^+}\right]_{\max}$, we have to mention a few words about the validity of the tabulated sputtering coefficients. The data for the sputtering yield of copper for argon ion energies ranging from $50eV$ to $600eV$ was taken from the work of Laegreid[4] et al.. They used a DC-discharge with a thermionic oxide cathode to create an argon plasma and biased a spherical copper target with diameter $\cong 0.6cm$ to obtain the sputtering yields. The voltage drop between the anode and the cathode of the discharge ranged from $34V$ to $40V$, and the gas pressure ranged from $2mtorr$ to $4mtorr$. Assuming that most of the voltage drop occurred within of the cathode sheath of thickness $\approx 0.1mm$ (the cathode being the source of the secondary electrons), the mean-free-path for the production of doubly charged ions[5] (the production of ions with a charge ≥ 3 has much less probability) and for electron-argon elastic collisions is $\approx 15cm$ and $1cm$ respectively; hence, the energetic secondary electrons (which have the larger probability of producing multiply charged ions) will 'slow down' well before they produce significant numbers of multiply charged ions. As for the

---

[3] W. H. Hayward and A. R. Wolter, J. Appl. Phys. **40 #7**, pp. 2911-2916 (6/1960)
[4] Nils Laegreid and G. K. Wehner, J. Appl. Phys. **32 #3,** pp. 365-369 (1961).
[5] NRL Plasma Formulary , p. 54 (1994)

bulk electrons, no measurements of the electron temperature were given, but by assuming a typical range of $1eV \leq T_e \leq 10eV$, we can compare the relative production rates of doubly charged to singly charged ions for a Maxwellian electron distribution with $T_e \approx 5eV$ and obtain a ratio of $\cong 10^{-2}$, implying that the presence of multiply charged ions can be neglected (as stated in the article).

Other possible sources for systematic errors in their experiments were surface oxide formation (which would have modified the sputtering yield), the effect of a changing target temperature ($300^{\circ}C$ to $500^{\circ}C$) on the yield, and re-deposition of the sputtered copper from 'back'-diffusion via collisions with the background argon gas atoms (which would have rendered the measured sputtering yield less than the 'true' yield). However, no variations of the sputtering yield with target current density (which is proportional to the incident heat flux) were observed, implying that the target temperature variation did not modify the yield and that oxide surface layer formation did not exist (if oxide layers had exited, they would have evaporated with increased incident heat flux, and a change in the yield would have been observed). The sputtering yield also remained independent of pressure for the operating pressure range (*2mtorr* to *4mtorr*) and began to drop for argon pressures greater than *15mtorr*; therefore, for the operating pressure range, the modification of the yield resulting from re-deposition was negligible.

The sputtering yield measured is assumed to be the yield at normal incidence from a mono-energetic ion flux; however, because of the finite ion temperature and collisions in the pre-sheath, the incident ion flux has a spread in its parallel and perpendicular energies with a value of at most $T_e/2$ (a significant portion of the ion parallel energy gain of $T_e/2$

through the pre-sheath can be transferred to its random thermal energy via collisions with the background gas atoms). This energy spread introduces a negligible change in the parallel energy ($(T_e/2)/(e\Delta V) \approx 2\% << 1$) and introduces a deviation from normal incidence of $a\tan\left((T_e/2)/e\Delta V\right) \approx 1^\circ$. A review article on sputtering by Oechsner[6] shows that the angular dependence of the yield decreases with lower energy bombardment, and even at energies near $1keV$, the angular dependence is less sensitive than what is predicted by a $\sec(\theta)$ model; hence even a 10° deviation from normal incidence would modify the yield by a factor $\leq 1\%$.

One last modification to the tabulated yield that must be considered is the correction to the measured current from secondary electron emission. Liebermann[7] gives a discussion of secondary electron emission in which he states the relation:

$$\gamma_{se} \cong (.016)\left(U_{iz}^{ion} - 2W_{Cu}\right)/eV : [2.2 - 1];$$

U_{iz}^{ion} is the ionization energy of the incident ion

$W_{Cu} \approx 4.65eV$ [8] is the electron work function for copper

Note that the coefficient is independent of the incident ion energy because the characteristic time for the emission is much smaller than the ion-lattice interaction time[9]. For incident argon ions ($U_{iz}^{ion} \cong 15.76eV$ [10]), this relation yields the value, $\gamma_{se} \cong 10\%$,

---

[6] H. Oechsner, Appl. Phys. **8**, pp.185-198 (1975)

[7] Liebermann and Lichtenberg, Principles of Plasma Discharges and Materials Processing, 1994, p. 282

[8] CRC Handbook of Chemistry and Physics, 73^{rd} edition, 12-109 (1992-3)

[9] Liebermann and Lichtenberg, Principles of Plasma Discharges and Materials Processing, 1994

[10] CRC Handbook of Chemistry and Physics, 73^{rd} edition, 10-211 (1992-3)

which is consistent with the value stated to be valid for incident ion energies below $1keV$ in[11].

The data for the self-sputtering coefficient ($ST_{Cu/Cu} \equiv (S-T)_{Cu/Cu}$) has been taken from the work of Hayward et al. [12]. They used a copper ion beam, which they deflected to extract any copper neutrals. The beam had an energy spread of $\approx 5eV$ (resulting in error in the parallel energy of $\approx 5/100 = 5\%$) and a maximum angular spread (with respect to the target normal) of 20° with less than 10% of the beam population at this extreme. We have estimated the error from the angular spread (assuming the beam to be Gaussian and the angular variation of the yield to be $\sec(\theta)$, which is an overestimate) to be less than 2%. Another source for error resulted from the use of the oscillating piezo-electric target crystal, which was used to determine the mass change of the copper target. The determination of the mass change required a calibration constant, which was determined by assuming a $10eV$ sputtering threshold; the assumption, the authors claim, resulted in less than 1% error for sputtering yields greater than 0.1.

In our experiments, the copper piece was exposed to the flux of two ion species: argon and copper, and in our analysis, we assumed that the two species acted independently: we assumed that there were no modifications to $S_{Cu/Ar}$ and $ST_{Cu/Cu}$ that might result from a synergism between the two species at the surface. This assumption is valid because the characteristic time between the arrival of two ions at one location on the surface ($\approx 10^{-10}s$), which is given by the ratio of the ion speed near the surface

[11] Nils Laegreid and G. K. Wehner, J. Appl. Phys. **32 #3**, pp. 365-369 (1961).
[12] W. H. Hayward and A. R. Wolter, J. Appl. Phys. **40 #7**, pp. 2911-2916 (6/1960)

$$\approx v_{surface} \approx \sqrt{2e\Delta V_{'sheath'}/m_{ion}}$$

to the average distance of separation between each ion at the sheath boundary

$$d \approx \left(n_{Cu^+} + n_{Ar^+}\right)_b^{-1/3} \approx \left(.5n_{e\infty}\right)^{-1/3},$$

enhanced by the 1-D density expansion factor from the acceleration within the 'sheath'

$$v_{surface}/v_b \cong \sqrt{2e\Delta V_{'sheath'}/T_e},$$

is much greater than the characteristic time of $\approx 10^{-13}s$ for the collision cascade[13] beneath the surface that is responsible for sputtering the copper atoms.

With the origins of the sputtering coefficients validated, we will discuss the details of the calculation of $\left[f_{Cu^+/Ar^+}\right]_{\max}$. Before we ran the experiments to determine this fraction, we used a pure argon plasma (copper target off) to sputter the copper piece (biased at $-92V$ and situated at $R \cong 2'' = 5cm$, $Z \cong 10'' = 25cm$) for two different operating conditions:

1. argon pressure: $0.75mtorr$

   microwave power: $2kW$

   electro-magnet currents (top/bottom) : $230A / 180A$,

2. argon pressure: $1.5mtorr$

   microwave power: $4kW$

   electro-magnet currents (top/bottom) : $230A / 180A$

Sputtering with only an argon plasma served two purposes:

[13] H. Oechsner, Appl. Phys. **8**, pp.185-198 (1975)

a) it yielded an experimental sputtering coefficient, which verified the data from the work of Laegreid et al. [14], and assuming that their data is valid, then our experimental sputtering coefficient yielded an energy for the incident argon ions, thereby giving an estimate for the plasma potential;

b) by comparing the sputtering coefficients for the two operating conditions, we were able to determine the degree of re-deposition of the sputtered copper; note that we did not expect re-deposition to be a factor because the work of Laegreid et al. demonstrated that there was insignificant re-deposition for gas pressures below $15mtorr$; note also that we changed the power as well as the pressure because we wanted to determine whether re-deposition would be significant from the sputtered copper neutrals being ionized within the pre-sheath and subsequently drawn back by the electric field to the copper piece (increasing the power increases the electron density, which increases the ionization rate, thereby decreasing the mean-free-path for ionization).

The sputtering coefficients (not corrected for secondary electron emission) for the first and second operating condition were determined to be $S_{Cu/Ar} \cong 0.45 \pm 0.1$ and $\cong 0.46 \pm 0.1$ respectively. Hence, with respect to the precision of our measurements, neither re-deposition from collisions with the background gas atoms nor re-deposition from the trapping of the copper neutrals in the potential well via ionization is significant. From the sputtering versus energy curves presented in the work of Laegreid et al. [15] and in the work of Matsunami[16], this sputtering coefficient corresponds to an incident ion

---

[14] Nils Laegreid and G. K. Wehner, J. Appl. Phys. **32 #3,** pp. 365-369 (1961).
[15] Nils Laegreid and G. K. Wehner, J. Appl. Phys. **32 #3,** pp. 365-369 (1961).
[16] M. Matsunami, At. Data Nucl. Data Tables 31,1 (1984)

energy of $\cong 100eV \rightarrow 110eV$. With the floating potential near the ground potential, the ion energy estimated from the sputtering curves corresponds to a 'sheath' potential drop of

$$\Phi_{\infty} - \Phi_{float} \cong E_{ion} + V_{bias} \approx 12V \rightarrow 20V,$$

which is consistent with the 'sheath drop' potential determined by the Langmuir probe at $R \cong 5cm$ (note, however, that the Langmuir probe measurements were taken for slightly different operating conditions). The determination of the incident ion energy is important when we bombard the copper piece with a mixture of argon and copper ions because we need this energy to determine the corresponding copper self-sputtering coefficient from the self-sputtering versus energy curve presented in the work of Hayward et al. In fact, it is the uncertainty in the incident ion energy that dominates the error in our measurement of the copper-to-argon ion fraction. Taking the incident ion energy to be $105eV \pm 5eV$, the corresponding self-sputtering coefficient becomes $ST_{Cu^+/Cu} \cong -0.46 \pm 0.04$.

With the established values for the sputtering coefficients, we will derive the equation that relates the copper-to-argon ion incident flux fraction to the current drawn by the piece and its mass change. The current drawn is related to the rate of incidence of the copper and argon ions:

$$\int_0^{\tau_{exp}} dt\left(I(t)/e\right) = (1+\gamma_{se}^{Ar})N_{Ar^+} + N_{Cu^+} : [2.2-2],$$

$$\gamma_{se}^{Ar} \cong 0.1,$$

where N_j is the total number of ions of species 'j' that are incident on the copper piece. This equation assumes that the secondary electron emission that results from copper ion

bombardment is negligibly small, an assumption that is validated by Liebermann's approximation for the secondary electron emission, equation 2.2-1, which predicts a value of zero for γ_{se}^{Cu}. The change in the mass of the copper piece results from copper deposition and etching (from sputtering):

$$\Delta M_{Cu} = M_{before} - M_{after} = \left(\frac{MW_{Cu}}{N_{Av}}\right)\Delta N_{Cu} \quad :[2.2-3],$$
$$\Delta N_{Cu} = S_{Cu/Ar} N_{Ar^+} + ST_{Cu/Cu} N_{Cu^+} - N_{Cu^0}$$

where

$MW_{Cu} = 64.5 g/mol$ is the molecular weight of copper

$N_{Av} = 6.023 \cdot 10^{23}\ atoms/mol$ is the Avogadro's number , and

$$S_{Cu/Ar}^{\exp}\left(V_{Bias} = -92V\right) \cong (.45 \pm .01) \Rightarrow S_{Cu/Ar}^{true}\left(V_{Bias} = -92V\right) \cong (.45 \pm .01)\left(1 + \gamma_{se}^{Ar}\right)$$

$$S_{Cu/Cu}\left(V_{Bias} = -92V\right) \cong -0.46 \pm 0.04$$

N_{Cu^0} is the total number of copper neutrals incident on the piece

After some algebraic manipulations, we obtain an expression relating the copper-to-argon ion fraction to the copper ion-to-neutral fraction and the measured current and mass change:

$$F_{Cu^+/Ar^+} \equiv \frac{1 - f_{Cu^+/Ar^+}}{f_{Cu^+/Ar^+}}$$
$$F_{Cu^+/Cu^0} \equiv \frac{1 - f_{Cu^+/Cu^0}}{f_{Cu^+/Cu^0}}$$
$$r \equiv \frac{\frac{1}{e}\int dt I(t)}{\Delta N_{Cu}}$$

$$F_{Cu^+/Ar^+} = \frac{1 - r\left(ST_{Cu^+/Cu} - F_{Cu^+/Cu^0}\right)}{\left(1+\gamma_{se}^{Ar/Cu}\right)\left[rS_{Ar^+/Cu}^{\exp} - 1\right]} :[2.2-4]$$

$$f_{Cu^+/Ar^+} = \frac{1}{1+F_{Cu^+/Ar^+}}$$

The measurements for the copper ion-to-neutral fraction (which we will discuss shortly) indicate that this fraction is $\geq 90\%$, and as stated previously, we set this fraction to $100\% \Rightarrow F_{Cu^+/Cu} = 0$ to obtain a maximum for the copper-to-argon ion fraction:

$$\left[F_{Cu^+/Ar^+}\right]_{\min} = \frac{1 - rST_{Cu^+/Cu}}{\left(1+\gamma_{se}^{Ar/Cu}\right)\left[rS_{Ar^+/Cu}^{\exp} - 1\right]} :[2.2-5].$$

$$\left[f_{Cu^+/Ar^+}\right]_{\max} = \frac{1}{1+\left[F_{Cu^+/Ar^+}\right]_{\min}}$$

The major contributors to the error in this measurement are

1. the precision of the micro-balance ($\pm 0.5mg$) coupled with the 'small' changes in the mass of the copper piece (as low as $5mg$ for some of the operating conditions) because of the time constraint of the experiment (which is set to render the experiment practical: $\tau_{\exp} \cong 30\min$)
2. the error in the value of $ST_{Cu/Cu}$ resulting from the uncertainty in the incident ion energy; the relative error is of order $\frac{\delta_{ST}}{ST} \approx 10\%$

The relative errors in the measured current and in the secondary electron emission is less than 1%; therefore, they are neglected. The relative error in the measurement of the copper to argon ion fraction is determined via the formula:

$$\left|\frac{\delta f_{Cu^+/Ar^+}}{f_{Cu^+/Ar^+}}\right| = \left(\sum_i \left(\frac{\partial}{\partial x_i}\ln\left(f_{Cu^+/Ar^+}\left(x_1, x_2, \ldots\right)\right)\right)^2 \left(\delta x_i\right)^2\right)^{1/2} : [2.2-6],$$

where the x_i's are the measured current, mass change, and the sputtering coefficients.

The variation of the measured 'maximum' copper-to-argon ion fraction (at $R \cong 2''$, $Z \cong 10''$) with power and pressure are shown in figures 2.2-1,2:

FIGURE 2.2-1: VARIATION OF THE MAXIMUM COPPER TO ARGON ION FRACTION WITH PRESSURE.

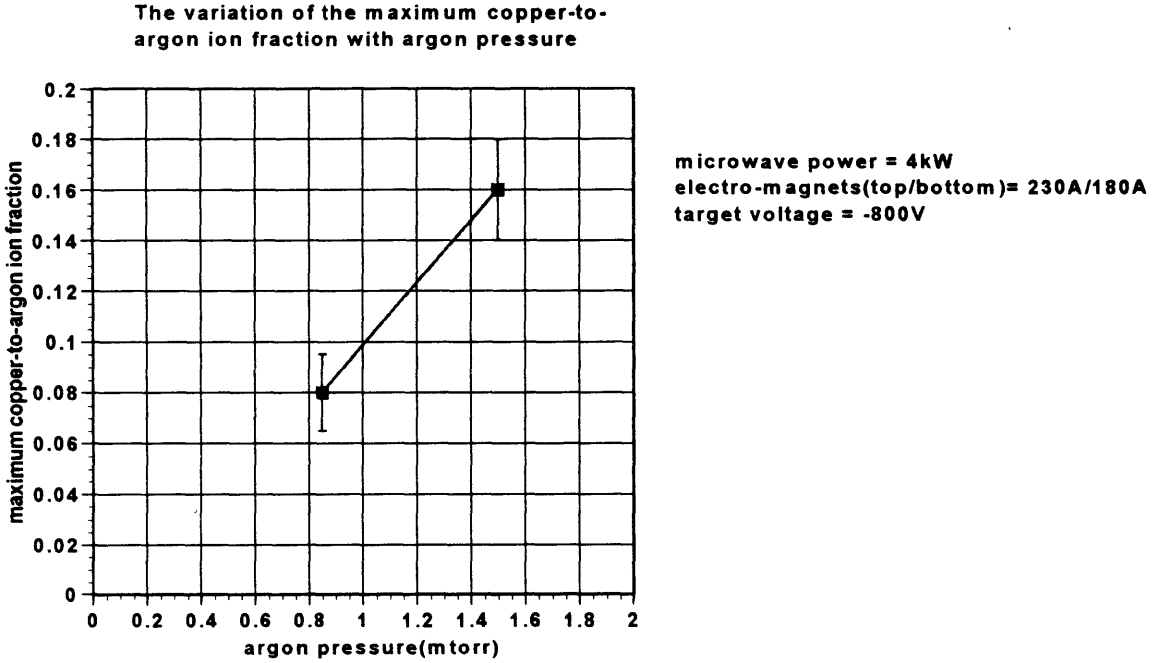

FIGURE 2.2-2: VARIATION OF THE MAXIMUM COPPER TO ARGON ION FRACTION WITH PRESSURE.

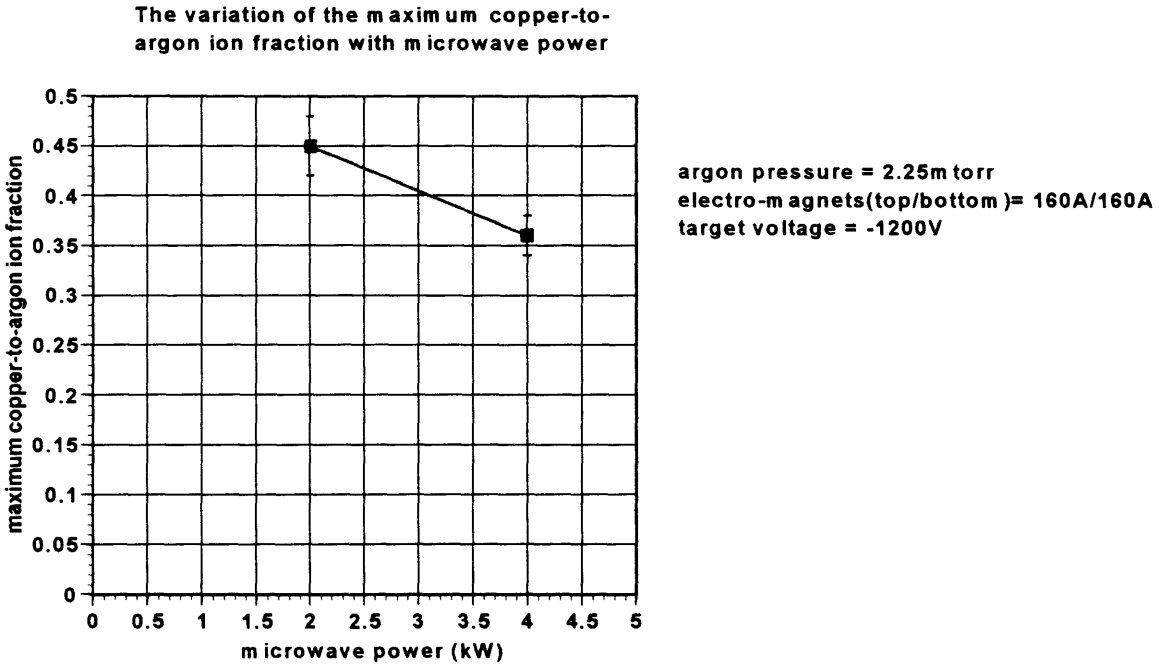

Figure 2.2-1 indicates that there is a potential for a substantial increase in the copper-to-argon ion fraction with increasing gas pressure. To understand this trend, we will first discuss the behavior of the target current. The increase in the gas pressure results in an increase in the target current as depicted in figure 2.2-3:

FIGURE 2.2-3: THE VARIATION OF THE TARGET CURRENT WITH PRESSURE.

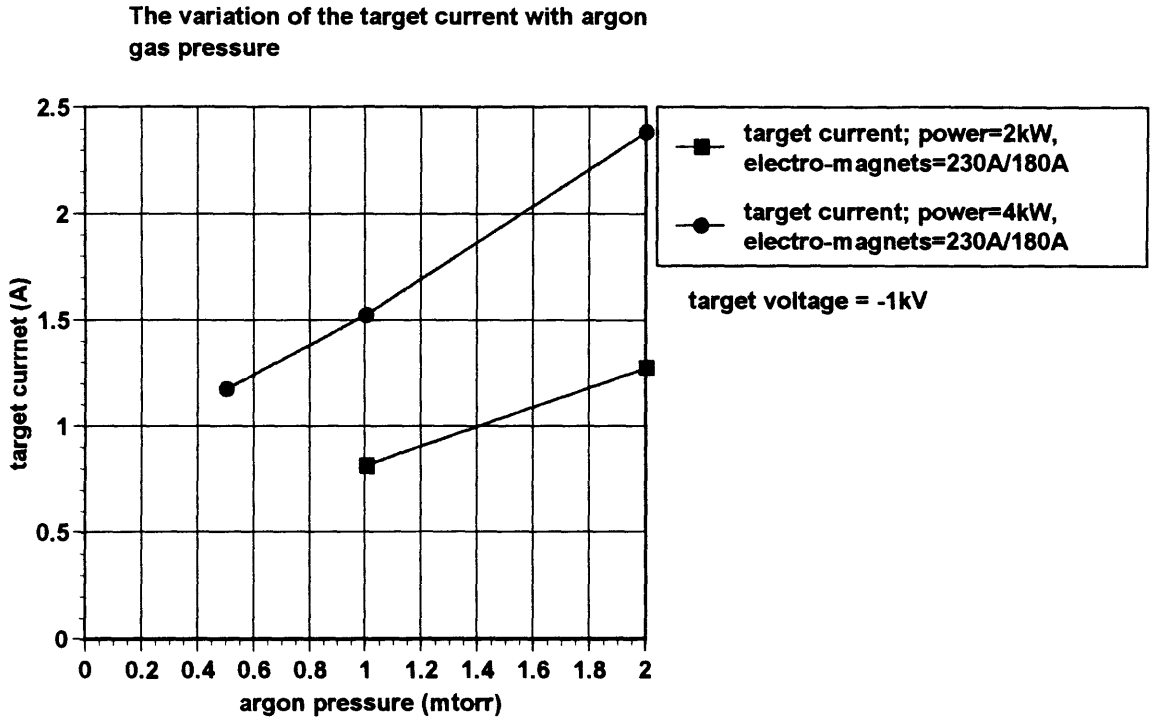

The increase in the target current is peculiar because the Liebermann model that we have presented in the beginning predicts that an increase in the gas density will not only decrease the temperature, it will also decrease the electron density. Noting that the current density is $\propto n_e \sqrt{T_e}$, the zero-dimensional model predicts a decrease in the target current with increasing gas pressure. This paradox can be resolved by noting that

a) the model is indeed zero-dimensional; therefore, it does not account for changes in the density and temperature profile, and

b) we have assumed that 100% of the microwave power is absorbed by the plasma; however, some of the power propagates along the metal cavity, depositing its power by resistively heating the metal surface. It maybe the case that the microwave power is more efficiently absorbed by the plasma at 'higher' pressures (as a result of the increase interaction between the heated electrons and the

background gas); hence, a greater fraction of the power would be deposited in the plasma at larger pressures.

The increase in the target current results in the increase in the number of copper atoms sputtered into the plasma; once ionized, the copper atoms contribute to the increase in the copper ion density as well as a decrease in the argon ion density (because for a given input power the total number of electrons remains the same; in fact the power input increases with target current as a result of an increase in the emission of energetic secondary electrons [$\left|I_{se}\right| \cong 10\% \left|I_T\right|$, and $U_{se} \approx -eV_T \cong 1KeV$]). Hence, $f^{bulk}_{Cu^+/Ar^+}$ increases, and if the copper ion transport efficiency is not degraded terribly from the increased gas density, the result will be an increase in $f^{sub}_{Cu^+/Ar^+}$, as observed in figure 2.2-1. Another possible contribution to the increase in $f^{sub}_{Cu^+/Ar^+}$ stems from the lower ionization energy of the copper atoms, which allows for the production of electrons (via ionization) with lesser electron energies, thereby reducing the requirement on the electron temperature to sustain the plasma (which lowers the electron temperature). For the copper's lower ionization energy to influence the electron temperature, however, the copper neutral density must be 'significant'; this is not the case for our plasma:

$$\left(n_{Cu}\right)_{Target} \approx \frac{S_{Cu/Ar^+}\left(I_T/e\right)}{A_T\left\langle u_{Cu}\right\rangle} \approx \frac{3\left(2A/e\right)}{\left(100cm^2\right)\left(5\cdot 10^5\, cm/s\right)} \cong 5\cdot 10^{11} cm^{-3} \Rightarrow$$

$$\frac{\left(n_{Cu}\right)_{Target} K^{Cu}_{iz}}{n_{Ar^0} K^{Ar}_{iz}} \approx \frac{5\cdot 10^{11} cm^{-3}}{5\cdot 10^{13} cm^{-3}} \exp\left(\frac{8eV}{T_e}\right) = 0.05 << 1$$

Figure 2.2-2 shows the variation of $\left[f^{sub}_{Cu^+/Ar^+}\right]_{\max}$ with increasing microwave power, but before we discuss the trend with microwave power, we note that these

measurements were made with modifications to the argon pressure, the target voltage, and the electro-magnet current settings. The modifications were motivated by the desire to maximize $\left[f^{sub}_{Cu^+/Ar^+}\right]_{\max}$. The increase in the argon pressure to a value of $2.25 mtorr$ follows from our interpretation of figure 2.2-1. The modifications to the target voltage ($1kV \rightarrow 1.2kV$) and electro-magnet currents ($230A/180A \rightarrow 160A/160A$) were motivated by the belief that an increase in the copper sputtering rate from the target would enhance $\left[f^{sub}_{Cu^+/Ar^+}\right]_{\max}$. The copper sputtering rate is controlled by the relation

$$\dot{N}_{Cu} \cong \frac{(I_T/e)}{1+\gamma_{se}} S_{Cu/Ar^+}(V_T),$$

S_{Cu/Ar^+} is a function of the incident ion energy, which is controlled by the target voltage, and it increases with increased incident ion energy in the energy range being considered ($< 1.5KeV$).

Actually, the sputtering of the copper target is done by both the argon and copper ions, but we have used the fact that $S_{Cu/Cu} \cong S_{Cu/Ar}$. The equation shows that an increase in the copper sputtering rate requires either an increase in the target current or an increase in the target voltage; hence, the justification for the increase in the target voltage. The justification for the modification to the electro-magnet settings comes from a previous discussion in which we argued that altering the electro-magnet settings in the particular way stated reduces the mirror force, which enhances the mobility of the ions to the target, thereby increasing the current to the target (as observed in figure 1.4-6).

Now, figures 2.2-1,2 demonstrate two things:

1. we have indeed enhanced $\left[f^{sub}_{Cu^+/Ar^+}\right]_{\max}$ with our modifications from a value of 8% for ($\Pr = .85mtorr, |V_T| = 800V, Magnets = 230A/180A, P_{\mu wave} = 4kW$) to a value of 36% for ($\Pr = 2.25mtorr, |V_T| = 1200V, Magnets = 160A/160A, P_{\mu wave} = 4kW$), and
2. $\left[f^{sub}_{Cu^+/Ar^+}\right]_{\max}$ decreases with increasing microwave power.

There is no concrete explanation for the observed variation of $\left[f^{sub}_{Cu^+/Ar^+}\right]_{\max}$ with microwave power. Our zero-dimensional model demonstrates that a variation of the microwave power results in a variation in the electron density with no change to the electron temperature, the latter is determined solely by the gas density and the source geometry. However, our zero-dimensional model does state that if the ionization is significant (that is if $\frac{n_e}{n_0} \approx 1$), then the microwave power will influence the electron temperature as well. The reason is that the steady state gas density is

$n_0 = n_g - n_e$,

n_g is the gas density before the creation of the plasma, and it is a function of the gas flow rate.

Therefore, for electron densities comparable to n_g, the drop in n_0 will increase the electron temperature, thereby increasing the preferential ionization of the argon. However, we know that for typical electron densities, the ratio

$$\frac{n_e}{n_g} \approx \frac{10^{12} cm^{-3}}{5 \cdot 10^{13} cm^{-3}} = 0.02 << 1;$$

therefore, there is no significant 'dent' in the gas density, and we do not observe (within the resolution set by experimental errors) a change in T_e with microwave power. However, we would like to emphasize a few points:

1. the ionization rates are somewhat sensitive to the electron temperature; therefore, a change in T_e by a fraction of an eV (which is below the resolution of experimental observation, $\delta T_e \approx 1eV$) can make a difference in the ratio of the ionization rate of copper to argon;
2. increasing the power will increase the electron density, hence, the ionization rate (which is proportional to the electron density); therefore, even if there is no change in the electron temperature, there will be an increase in the ionization rates of both copper and argon. The increase in the copper ionization rate implies an increase in the transport efficiency of the copper (the transport efficiency is dependent on the ionization of the copper as well as on its radial confinement, and both are improved with increased ionization of the copper as discussed in section 1.3). However, the increase in the ionization rate of argon will compete to reduce $\left[f^{sub}_{Cu^+/Ar^+} \right]_{\max}$; and
3. The increase in the microwave power increases the target current, as shown in figure 2.2-4:

FIGURE 2.2-4: THE VARIATION OF THE TARGET CURRENT WITH POWER.

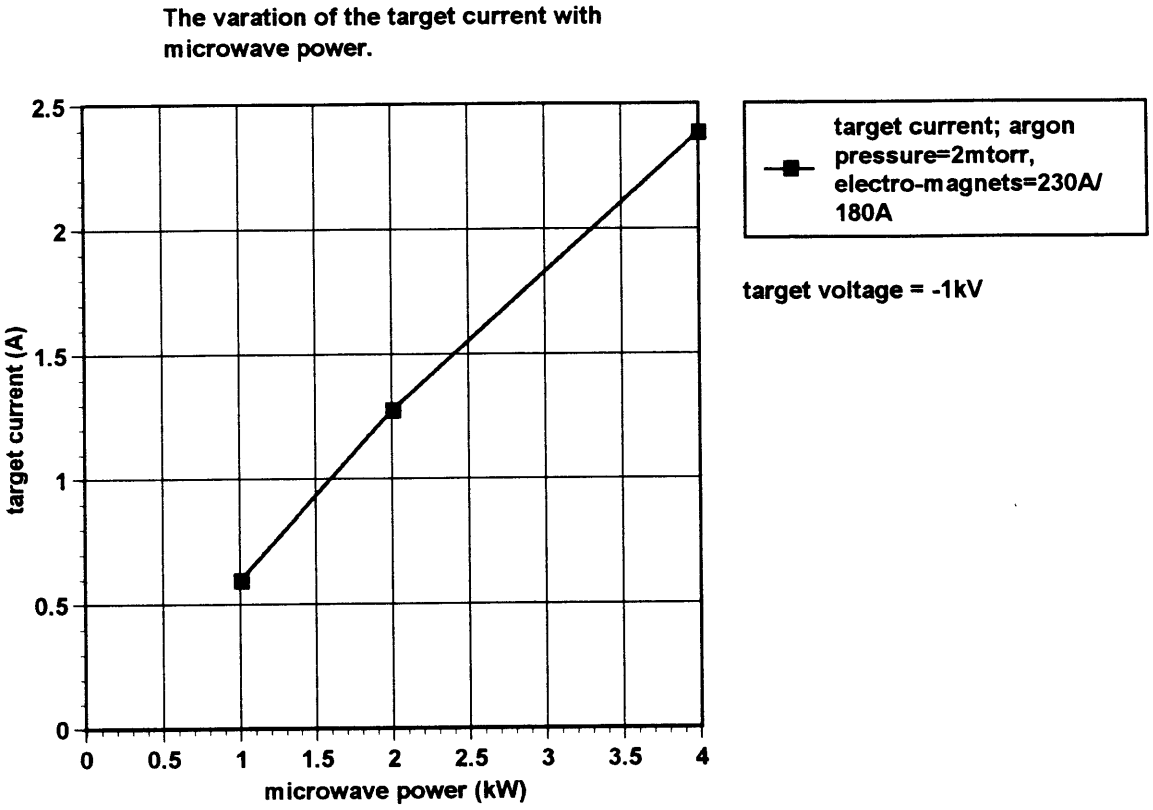

Therefore, if we isolate the microwave power's influence on the target current, we would expect an increase in $\left[f_{Cu^+/Ar^+}^{sub}\right]_{\max}$, opposite of what is observed.

4. we have to remember that we have a local ($R = 5cm, \Theta = 0^\circ$) measurement of this fraction; therefore, we have not accounted for any plasma profile variation with microwave power, which will ultimately influence the copper transport to our local region.

FIGURE 2.2-5: THE VARIATION OF THE COPPER DEPOSITION UNIFORMITY WITH MICROWAVE POWER.

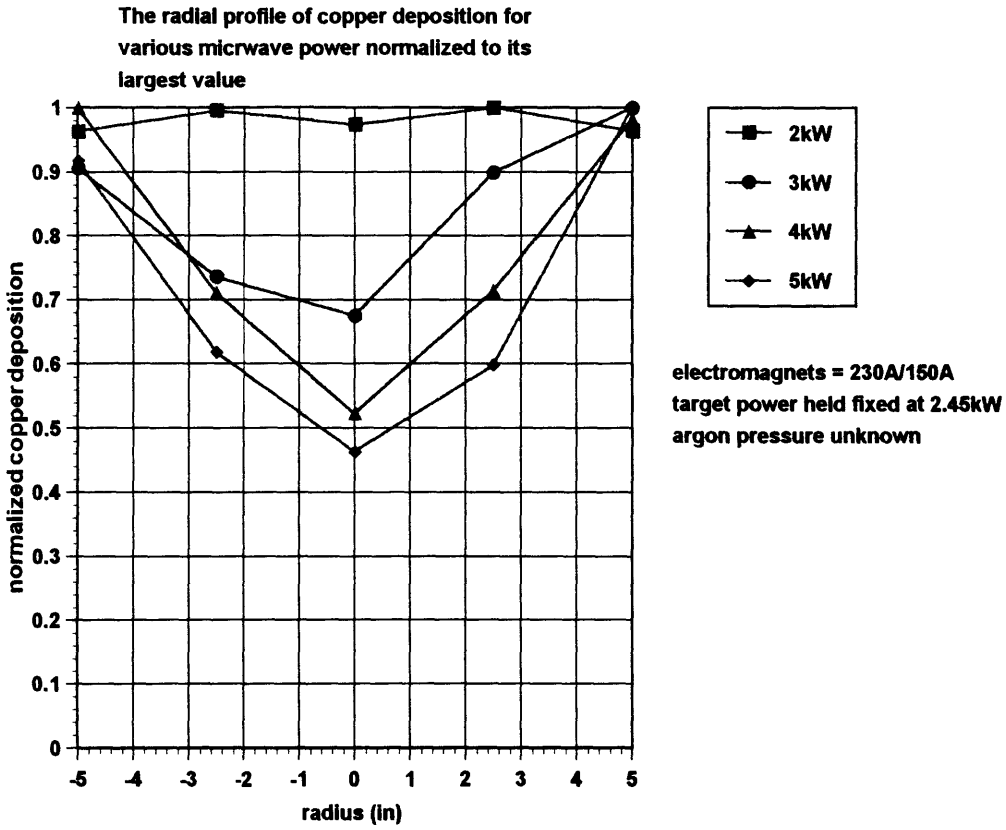

Figure 2.2-5 illustrates the change in the radial profile of deposited copper at the substrate with microwave power. The profile shifts radially outward with increased power. This shift suggests that the target current density (which is somewhat equivalent to the copper sputtering profile) also shifts outward with increased power. This radial shift in the copper sputtering profile reduces the copper transport efficiency (because more of the copper will deposit on the side-wall) and can explain the reduction in $\left[f^{sub}_{Cu^+/Ar^+}\right]_{\max}$ with power.

The point to take away from the analysis of $\left[f^{sub}_{Cu^+/Ar^+}\right]_{\max}$ is that there is potential for significant improvement in this fraction, a potential that was not exploited in the choice

of previous run conditions (previous run conditions were concentrated near pressures at or below $1.5mtorr$ with electro-magnet settings of $230A / 180A$). The question that remained was whether the fill characteristics would improve upon changing the process parameters to yield larger $\left[f^{sub}_{Cu^+/Ar^+}\right]_{\max}$; we will address this question after we discuss the measurement of an equally important plasma surface parameter: $f^{sub}_{Cu^+/Cu^0}$.

2.3: MEASUREMENT OF THE COPPER ION-TO-NEUTRAL FRACTION AT THE SUBSTRATE

$$f^{sub}_{Cu^+/Cu^0} \equiv \left[\frac{\Gamma_{Cu^+}}{\Gamma_{Cu^+} + \Gamma_{Cu^0}}\right]_{substrate}$$

Γ_j denotes the flux of species 'j'

In the previous section, we stated, without proof, that the copper neutral fraction was negligible; this assumption allowed us to determine $f^{sub}_{Cu^+/Ar^+}$. However, we noted that with the presence of a copper neutral flux at the substrate, the calculated $f^{sub}_{Cu^+/Ar^+}$ would be an overestimate of this fraction; hence, we labeled it $\left[f^{sub}_{Cu^+/Ar^+}\right]_{\max}$. In this section, we will propose a method for obtaining an upper limit for the copper neutral-to-ion fraction, $1 - f^{sub}_{Cu^+/Cu^0}$, and we will use the method to show that

$$f^{sub}_{Cu^+/Cu^0} > 90\%$$

for all relevant process conditions; hence, validate that $\left[f^{sub}_{Cu^+/Ar^+}\right]_{\max}$ is an excellent approximation to $f^{sub}_{Cu^+/Ar^+}$.

The method consists of the measurement of the efficiency with which copper from the target is transported to a crucible at the substrate; the measured efficiency is proportional to the ratio of the change in mass of the crucible, as a result of copper deposition, to the integrated (integrated over the period of the run) target current, which is a measure of the number of copper particles sputtered from the target:

$$\eta_{Cu}^{\exp} \equiv \frac{Cu_{deposited}}{Cu_{sputtered}} = \frac{Mass_{Cu}^{deposited}\left(\frac{N_{Av}}{MW_{Cu}}\right)}{\frac{1}{e}\left(S_{Cu/Ar}\int dt \cdot I_{Ar^+}^{target} + S_{Cu/Cu}\int dt \cdot I_{Cu^+}^{target}\right)}$$

$$I^{target} = \left(1+\gamma_{se}^{Ar}\right)I_{Ar^+}^{target} + \left(1+\gamma_{se}^{Cu}\right)I_{Cu^+}^{target} \qquad :[2.3-1]$$

$$I \equiv \int_0^{R_{target}} 2\pi r dr \cdot J$$

$$f_{Cu^+/Ar^+}^{target} \equiv \frac{J_{Cu^+}^{target}}{J_{Cu^+}^{target} + J_{Ar^+}^{target}}$$

The measured efficiency is then compared to a *conservative* theoretical calculation of the copper **neutral** transport efficiency. The difference between the two efficiencies would then be attributed to the copper ion transport. For example, if the ratio of the theoretical copper neutral transport efficiency to the experimental copper transport efficiency (which is the copper ion + neutral) is $\frac{\eta_{Cu^0}^{theory}}{\eta_{Cu}^{\exp}} \cong 0.1$, then we know that more than 90% of the contribution ('more than', because the theoretical calculation is conservative, therefore, it will overestimate the copper neutral contribution) to the copper deposition in the crucible is from the copper ions; hence we would conclude that $f_{Cu^+/Cu^0}^{sub} \equiv \left[\frac{\Gamma_{Cu^+}}{\Gamma_{Cu^+} + \Gamma_{Cu^0}}\right]_{substrate} \geq 90\%$. Now that we have established the logic behind the calculation, we will discuss the theoretical calculation of the copper neutral transport efficiency.

Before, we discuss the method, we will describe the geometry:

FIGURE 2.3-1: Schematic of the geometry needed for the calculation of the neutral transport efficiency from the target

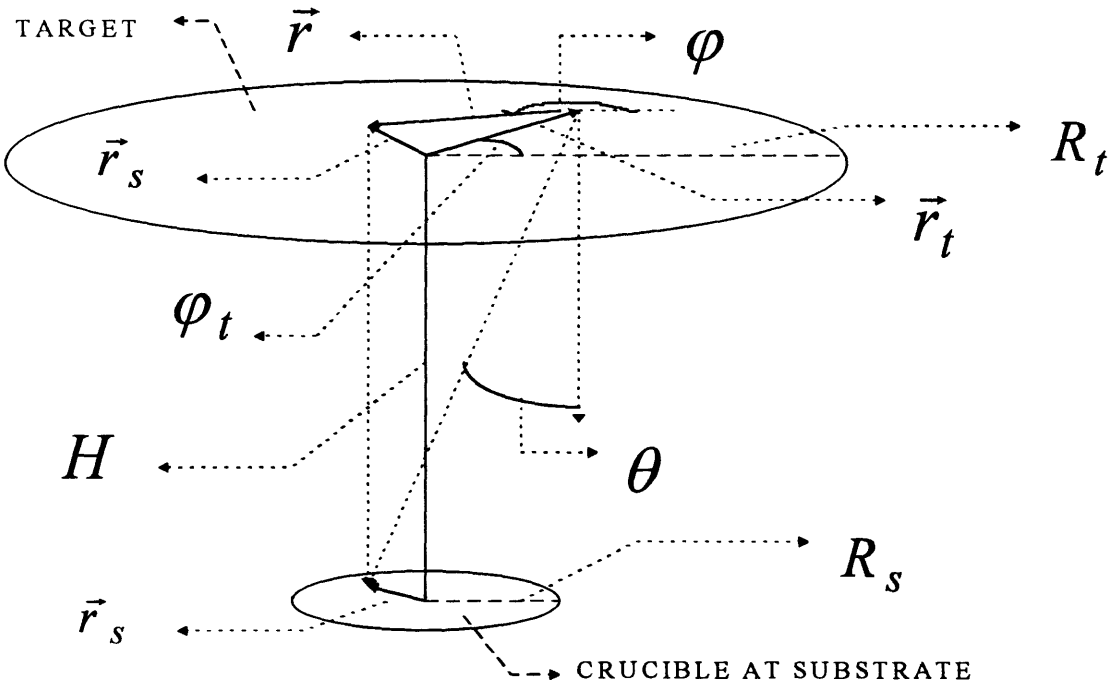

Figure 2.3-1 is an illustration of the geometry of the target and the crucible. We situate a crucible (with a one inch diameter: $R_s = .5''$) at the substrate, which is 9.5 inches from the target ($H = 9.5''$). We are interested in the efficiency with which the copper particles reach this crucible. We assume that the copper particles do not experience any collisions during their flight towards the crucible; this assumption is, of course, very conservative, therefore, it will give us an upper bound on the copper transport efficiency. With collisions eliminated, the calculation of the transport efficiency becomes purely geometric. The only knowledge that is required is the angular (θ) dependence of the copper flux leaving the target, the value of the copper sputtering coefficient at the incident target ion energies, and the radial current density distribution.

The geometry is in the calculation of the range in (θ,φ) at a given target position (r_t,φ_t) such that the particles being sputtered from that location reach the crucible. From figure 2.3-1, it is apparent that the criteria to be satisfied is

$$r_s = \|\vec{r}_t + \vec{r}\| \le R_s : [2.3-2],$$

or equivalently

$$r_s^2 = r^2 + r_t^2 + 2rr_t\cos(\chi) \le R_s^2$$
$$\cos(\chi) \equiv \frac{\vec{r}\cdot\vec{r}_t}{rr_t} = e_r \cdot e_{r_t} \qquad :[2.3-3].$$

To obtain this criteria as a function of the relevant variables, (θ,φ), we note the relations:

$$\chi(\varphi,\varphi_t) = \varphi - \varphi_t$$
$$r(\theta) = H\tan(\theta) \qquad :[2.3-4].$$

The total contribution from the target must be broken into two distinct regions:

1) $r_t \le R_s$

2) $r_t \ge R_s$,

where $r_t \equiv \|\vec{r}_t\|$.

In addition, the integrals over region (1) must be separated into two distinct contributions:

a) $r_t + r \le R_s$

b) $r_t + r \ge R_s$,

where $r \equiv \|\vec{r}\|$.

These separations become clear when we examine figure 2.3-2:

FIGURE 2.3-2: A top view of the target and the crucible at the substrate accompanied by an illustration of the three distinct classes of contributions (denoted by the subscripts on the radius vectors) to the transport efficiency integrals.

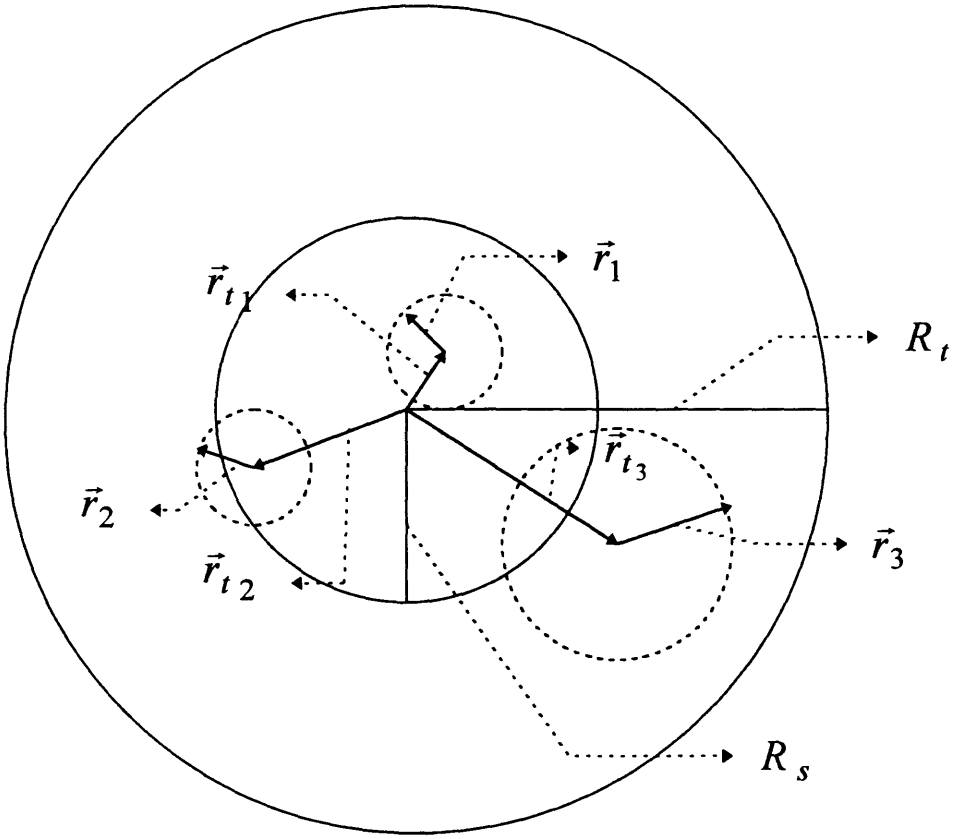

The figure depicts the three distinct contributions to the crucible collection efficiency. We note again that for the sputtered particle to deposit into the crucible, the magnitude of its radial coordinate, $\|\vec{r}_s\| = \|\vec{r}_t + \vec{r}\| = \left(r_t^2 + r^2 + 2rr_t\cos(\chi)\right)$, must be less than R_s. Hence, figure 2.3-2 shows that for the first class of contributions, where $r + r_t \leq R_s$, the sputtered particle will reach the crucible for all χ, $0 \leq \chi \leq 2\pi$:

$$r_1^{LB} = 0 \Rightarrow \theta_1^{LB} = a\tan\left(\frac{0}{H}\right) = 0$$

$$r_1^{UB} = R_s - r_t \Rightarrow \theta_1^{UB} = a\tan\left(\frac{R_s - r_t}{H}\right) :[2.3-5];$$

$$\chi_1^{LB} = \varphi_1^{LB} - \varphi_t = 0$$

$$\chi_1^{UB} = \varphi_1^{UB} - \varphi_t = 2\pi$$

where as for the second and third class of contributions, both 'r' and 'χ' are limited (there are values of 'r' and 'χ' such that $\|\vec{r}_s\| = \|\vec{r}_t + \vec{r}\| \geq R_s$ and the particle does not reach the crucible). The limits on χ are determined by equation 2.2-3. For the class (2) contributions, where $r_t \leq R_s$ but $r_t + r \geq R_s$, the lower and upper limits on 'r' and 'χ' are:

$$r_2^{LB} = R_s - r_t \Rightarrow \theta_2^{LB} = a\tan\left(\frac{R_s - r_t}{H}\right)$$

$$r_2^{UB} = R_s + r_t \Rightarrow \theta_2^{UB} = a\tan\left(\frac{R_s + r_t}{H}\right)$$

$$\chi_2^{LB} = \varphi_2^{LB} - \varphi_t = a\cos\left(\frac{R_s^2 - \left(r_t^2 + r^2\right)}{2rr_t}\right) \qquad :[2.3-6]$$

$$\chi_2^{UB} = \varphi_2^{UB} - \varphi_t = 2\pi - a\cos\left(\frac{R_s^2 - \left(r_t^2 + r^2\right)}{2rr_t}\right)$$

The limits for the class (3) contributions, where $r_t \geq R_s$, are identical to the class (2) limits except for one modification: $r^{LB} = r_t - R_s$.

With the above limits, we can establish the integrals needed for obtaining the transport efficiency. We will assume that we know the profile for the differential source rate from the target (the number of copper neutrals sputtered per steradian per unit target area per second) and calculate it later:

$$d\dot{s} = \dot{s}\left(E_{inc}^{ion}, \theta, \varphi, r_t, \varphi_t\right) d\Omega dA_t$$
$$d\Omega = \sin(\theta)(d\theta)(d\varphi); \qquad :[2.3-7]$$
$$dA_t = r_t dr_t d\varphi_t$$

Given this differential source rate, we can calculate the rate of copper deposition into the crucible (again, with the assumption of the straight line trajectories [no collisions]) by integrating the differential source rate over the solid angle (with the appropriate limits, which are functions of the local target coordinate) and then over the target area, noting the three separate class of contributions. With the above prescription, the deposition rate becomes the sum of three integrals (corresponding to the three classes):

$$\dot{D} = \int_{r_t=0}^{R_t} dr_t r_t \int_{\varphi_t=0}^{2\pi} d\varphi_t \left(\dot{d}_1\left(r_t, \varphi_t\right) + \dot{d}_2\left(r_t, \varphi_t\right) + \dot{d}_3\left(r_t, \varphi_t\right)\right)$$
$$\dot{d}_j\left(r_t, \varphi_t\right) = \int_{\theta=\theta_j^{LB}\left(r_t,\varphi_t\right)}^{\theta_j^{UB}\left(r_t,\varphi_t\right)} d\theta \sin(\theta) \int_{\varphi=\varphi_j^{LB}\left(r_t,\varphi_t,\theta\right)}^{\varphi_j^{UB}\left(r_t,\varphi_t,\theta\right)} d\varphi \; \dot{s}\left(E_{inc}^{ion}, \theta, \varphi, r_t, \varphi_t\right) \qquad :[2.3-8].$$

One further simplification comes from the knowledge that the source is neither a function of 'φ_t' (because of azimuthal symmetry) or 'φ' (because of the symmetry in the target crystal structure). The simplification leads to

$$\dot{d}_j\left(r_t, \varphi_t\right) = \int_{\theta=\theta_j^{LB}\left(r_t,\varphi_t\right)}^{\theta_j^{UB}\left(r_t,\varphi_t\right)} d\theta \sin(\theta)\left(\varphi_j^{UB}\left(r_t, \varphi_t, \theta\right) - \varphi_j^{LB}\left(r_t, \varphi_t, \theta\right)\right)\left(\dot{s}\left(E_{inc}^{ion}, \theta, r_t\right)\right) \qquad :[2.3-9]$$

The differential source rate is determined from the characteristics of the differential sputtering yield. The review by Oechsner[1] states that the θ-dependence of the sputtering yield can be approximated by $\cos^l(\theta)$ with $l \approx 1$ for incident ion energies of $\approx 1KeV$. Now, both copper and argon ions are incident on the target; therefore, the source rate will

be the sum of the contributions from both of these ion species. To obtain an accurate measure of the differential source rate, we need the velocity distribution function for each ion species, because as stated previously, the sputtering yield is both a function of the incident ion energy and angle; however, for typical run conditions

a) the target is biased to $\approx 1KeV$,

b) the electron temperature is $\approx 5eV$,

c) the plasma potential is $\approx 20V$,

d) the mean-free-path for collisions is $\approx 5cm$,

e) the sheath thickness (this is not including the pre-sheath) is $\leq 1mm$, and

f) uncertainties in the parallel and perpendicular temperature resulting from collisions in the pre-sheath will be $\leq T_e/2$ because most of the energy gain will be through the sheath which is , as stated, less than $1mm$ from the target where collisions are negligible ($\left(\leq 1mm/5cm\right) \leq 0.02$).

Hence, the uncertainty in the incident ion parallel energy that will result from the uncertainties in the plasma potential is

$$\frac{\delta E_{inc}^{ion}}{E_{inc}^{ion}} \approx \frac{\delta eV_{plasma}}{\left(-eV_{target} + V_{plasma}\right)} \approx \frac{5eV}{1KeV} = 0.002;$$

and the spread in the ion incident angle will be

$$\theta_{inc} \approx \tan\left(\theta_{inc}\right) \approx \frac{v_{perp}}{v_{parallel}} = \sqrt{\frac{E_{perp}}{E_{parallel}}} \cong \sqrt{\frac{T_e/2}{-eV_{target}}} \approx 0.05 radians.$$

---

[1] H. Oechsner, Appl. Phys. **8**, pp.185-198 (1975)

The uncertainties in the sputtering coefficient that will arise from the uncertainties in E_{inc} and θ_{inc} (with $S = S_{Cu/Ar^+}$) depend on the variation of the sputtering coefficient with these variables[2 3]:

$$\left|\frac{\delta S}{S}\right| = \left|\left[\frac{\partial \ln(S)}{\partial \ln(E_{inc})}\right]_{E_{inc}=1keV}\left(\frac{\delta E_{inc}}{E_{inc}}\right)\right| \approx .5\left|\frac{\delta E_{inc}}{E_{inc}}\right| \approx 10^{-3},$$

$$\left|\frac{\delta S}{S}\right|_{\theta} = \left[\frac{\partial \ln(S)}{\partial \theta_{inc}}\right]_{\theta_{inc}=0}\delta\theta_{inc} \approx \tan(0)\delta\theta_{inc} + \sec^2(0)\frac{(\delta\theta_{inc})^2}{2} \cong 10^{-3}.$$

As demonstrated, these uncertainties do not affect the value of the sputtering coefficient significantly; hence, we can justify treating the incident ion flux as a mono-energetic beam with the energy of $(-e(V_{target} - V_{plasma}) \approx 1keV)$ directed normal to the target ($\theta_{inc} = 0$). The sputtering coefficients at this energy are $S_{Cu/Ar^+} \cong 2.8$ and $S_{Cu/Cu^+} \cong 2.95$.

With the approximation of a mono-energetic beam for the incident ion flux, the differential source rate becomes

$$\dot{s} \equiv \frac{\partial^2 \dot{s}}{\partial\Omega\partial A_t} = \Gamma_{Cu^+}\frac{\partial^2 S_{Cu/Cu^+}}{\partial\Omega} + \Gamma_{Ar^+}\frac{\partial^2 S_{Cu/Ar^+}}{\partial\Omega} \qquad :[2.3-10],$$

$$\frac{\partial^2 S_{Cu/j^+}}{\partial\Omega} = \frac{(l_j+1)}{2\pi}\left(\cos^{l_j}(\theta)\right)S_{Cu/j^+}$$

where $l_j \cong 1$,

Γ_j is the incident ion flux of species 'j',

---

[2] M. Matsunami, At. Data Nucl. Data Tables 31,1 (1984)
[3] H. Oechsner, Appl. Phys. **8**, pp.185-198 (1975)

S_{Cu/j^+} is the sputtering coefficient of copper via bombardment by ion species 'j' evaluated at the ion incident energy ($\cong 1keV$),

and $\frac{(l_j+1)}{2\pi}$ is the normalization constant (such that $\int d\Omega \frac{\partial^2 S_{Cu/j^+}}{\partial\Omega} = S_{Cu/j^+}$).

The current to the target relates the flux of both the copper and argon ion species:

$$I_{target} = 2\pi \int_0^{R_t} dr_t r_t J(r_t);$$

$$J(r_t) = (1+\gamma_{se}^{Ar})\Gamma_{Ar^+}(r_t) + (1+\gamma_{se}^{Cu})\Gamma_{Cu^+}(r_t); \Rightarrow \quad :[2.3-11],$$

$$I_{target} = 2\pi \int_0^{R_t} dr_t r_t (1+\gamma_{se}^{Ar})(e\Gamma_{Ar^+}(r_t)) \left[1 + \frac{(1+\gamma_{se}^{Cu})}{(1+\gamma_{se}^{Ar})} \frac{f_{Cu^+/Ar^+}^{target}(r_t)}{1 - f_{Cu^+/Ar^+}^{target}(r_t)}\right]$$

where γ_{se}^{j} is the secondary electron emission resulting from bombardment by species 'j',

'e' is the electron charge

and $f_{Cu^+/Ar^+}^{target} = \left[\frac{\Gamma_{Cu^+}}{\Gamma_{Cu^+} + \Gamma_{Ar^+}}\right]_{target}$ is the copper-to-argon ion flux fraction at the target.

If we take f_{Cu^+/Ar^+}^{target} to be independent of the target radius, then the differential source rate becomes

$$\dot{s}(\theta, r_t) = \hat{J}(r_t)\left[S_{Cu/Ar^+}(l_{Ar}+1)\cos^{l_{Ar}}(\theta)\right]\frac{I_{target}/e}{2\pi(1+\gamma_{se}^{Ar})} R_{Cu/.Ar}(\theta) \quad :[2.3-12],$$

where

$$R_{Cu/.Ar}(\theta) = \frac{1 + f_{Cu^+/Ar^+}^{target}\left(\left(\frac{l_{Cu}+1}{l_{Ar}+1}\right)\left(\frac{S_{Cu/Cu^+}}{S_{Cu/Ar^+}}\right)\left(\frac{\cos^{l_{Cu}}(\theta)}{\cos^{l_{Ar}}(\theta)}\right)-1\right)}{1+\frac{f_{Cu^+/Ar^+}^{target}\left(\gamma_{se}^{Cu}-\gamma_{se}^{Ar}\right)}{1+\gamma_{se}^{Ar}}} : [2.3-13],$$

and, $\hat{J}(r_t) = \frac{1}{I_{target}} J(r_t)$, is the normalized current density, the current profile.

We will simplify the calculation by noting that

a) even though the profile of the sputtered copper has a θ-dependence of $\approx \cos(\theta) \rightarrow l \approx 1$, we will take $l = 0$ (thereby modeling the copper source as isotropic in the hemisphere). This approximation is appropriate because the copper particle will experience many collisions before reaching the substrate ($\approx \frac{H}{\lambda_{mfp}} \approx \frac{25cm}{5} = 5$); hence, the initial directional copper flux that is leaving the target will become isotropic via collisions (pre-dominantly) with the background argon gas atoms;

b) the secondary electron emission for copper (as stated previously) is negligible, and $\gamma_{se}^{Ar} \cong 0.1$;

c) with the approximation in (a) and (b) and with $\frac{S_{Cu/Cu^+}}{S_{Cu/Ar^+}} \cong 1.05$,

$R_{Cu/.Ar} = \frac{1+.05 f_{Cu^+/Ar^+}^{target}}{1-.09 f_{Cu^+/Ar^+}^{target}}$, becomes independent of 'θ' and quite insensitive to the target copper-to argon-ion fraction:

$$\frac{R_{Cu/.Ar}\left(f^{target}_{Cu^+/Ar^+}=.5\right)-R_{Cu/.Ar}\left(f^{target}_{Cu^+/Ar^+}=0\right)}{R_{Cu/.Ar}\left(f^{target}_{Cu^+/Ar^+}=0\right)}=\frac{1.07-1}{1}=0.07$$, note that we took $0 \le f^{target}_{Cu^+/Ar^+} \le 0.5$ because the argon ion density tends to dominate the copper ion density for typical run conditions (see figures 2.2-1,2 in conjunction with the understanding that $f^{sub}_{Cu^+/Ar^+}$ is a good indication for $f^{target}_{Cu^+/Ar^+}$).

If we integrate this differential source rate over the appropriate limits (as given), then we will obtain the 'geometric' efficiency for neutral copper deposition; however, we also need to account for the ionization of the copper as it travels towards the substrate. The ionization can easily be incorporated by assuming a constant axial and radial electron density and temperature profile, yielding an approximate factor of

$$\exp\left(-\frac{H/\cos(\theta)}{\lambda_{iz}}\right);$$

$$\lambda_{iz}=\frac{u_n}{n_e K_{iz}\left(T_e\right)}$$, (the mean-free-path for ionization)

where, $u_n \approx 2\cdot 10^3\, m/s$, is the average speed of the neutral particles leaving the target (see figure 1.2-1),

K_{iz} is the ionization rate constant (determined with a Maxwellian electron velocity distribution function, which will overestimate the ionization rate because the true distribution function will have a depressed high energy tail, thereby underestimate the neutral collection efficiency (not preferred if we want to obtain an upper bound on the neutral collection efficiency)),

and $H/\cos(\theta)$ is the distance traveled by the copper atom from the target

location (r_t) to a location inside the crucible (r_s) such that

$$r = \left\| \vec{r}_s - \vec{r}_t \right\| = H \tan(\theta) .$$

Of course, the density and temperature profiles are not constant; they are shifted 'outward' as shown in figures 2.1-6,7,8; therefore, the particles that emerge from the target edge will be ionized more efficiently than the ones that emerge from the target center. Furthermore, the sputtered neutral profile (being proportional to the incident target current density profile) will also be shifted 'outward'; therefore, the true geometric collection efficiency will be less than the geometric efficiency of a uniformly sputtered neutral distribution because of the decrease in the view factor of the particles emerging from the target edge. Hence, by assuming a uniform temperature and density profile and by using a low estimate for the electron density and temperature, we will obtain an upper bound on the neutral transport efficiency and an upper bound on $f^{sub}_{Cu^0/Cu^+} = 1 - f^{sub}_{Cu^+/Cu^0}$.

The theoretical calculation with the following parameters,

$$n_e = 3 \cdot 10^{13} cm^{-3}$$
$$T_e = 5eV$$
$$f^{target}_{Cu^+/Ar^+} = 0.1$$
$$\gamma^{Ar}_{se} = 0.1; \gamma^{Cu}_{se} = 0.05$$
$$l_{Cu} = l_{Ar} = 0$$

yields

$$\eta^{theory}_{Cu} = 1.3 \cdot 10^{-4} .$$

A comparison of the theoretical efficiency with the measured values ($\approx 3 \cdot 10^{-3}$) shown in the figures 2.3-3,4 demonstrates that $\left[\frac{\eta_{Cu}^{theory}}{\eta_{Cu}^{\exp}}\right]_{\max} < 10\%$, thereby confirming that the copper ion-to-neutral fraction, $f^{sub}_{Cu^+/Cu^0} = 1 - f^{sub}_{Cu^0/Cu^+} \geq 1 - \frac{\eta_{Cu}^{theory}}{\eta_{Cu}^{\exp}} > 90\%$.

FIGURE 2.3-3,4: THE VARIATION OF THE COPPER TRANSPORT EFFICIENCY WITH PRESSURE AND POWER.

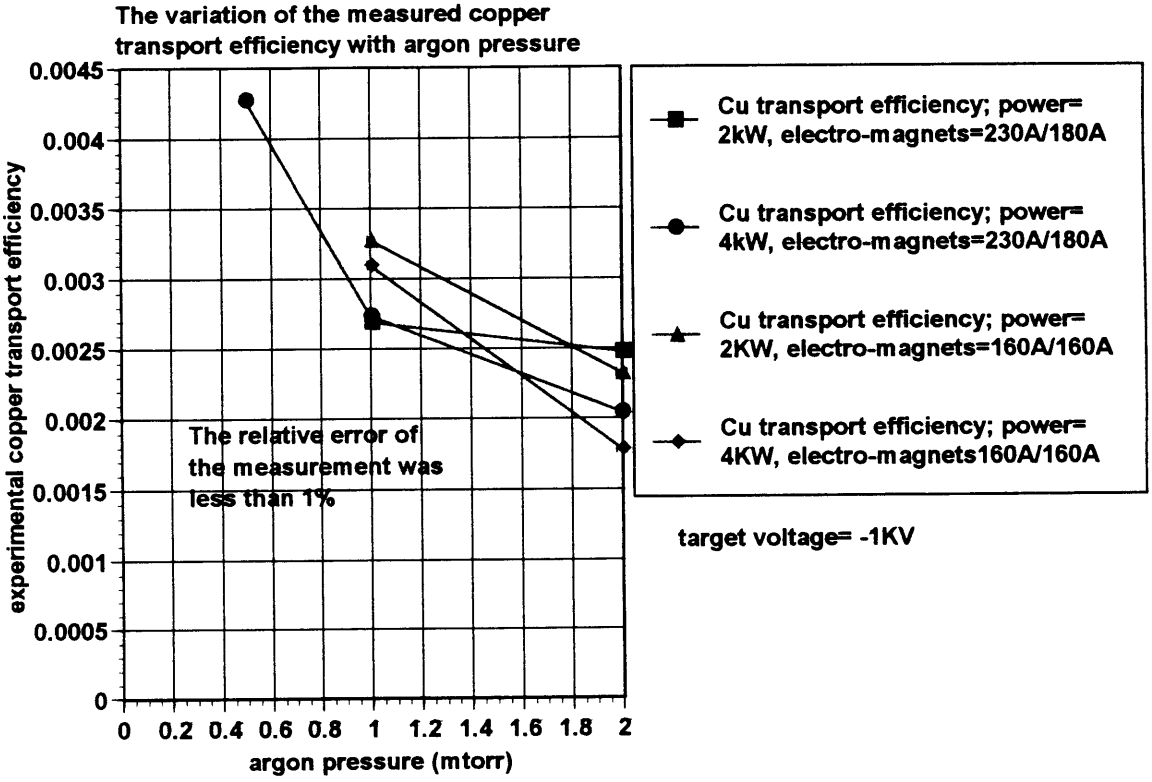

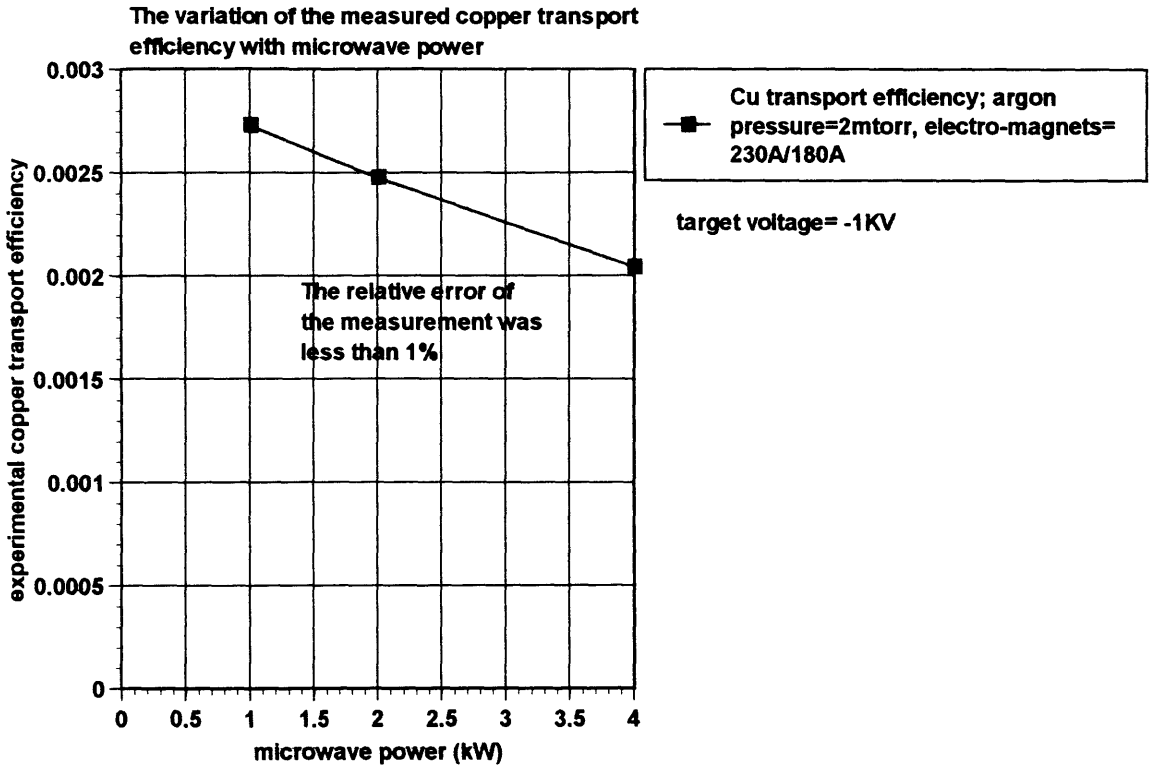

The decrease in the copper collection efficiency with increased argon pressure can be explained from arguments in chapter 1: the enhanced copper ion radial diffusion, which results from the increase in the copper ion-argon neutral collision frequency. Whereas, the decrease in the efficiency with power is the result of the radial shift in microwave power absorption (see figure 2.2-5 and the following paragraph).

CHAPTER 3

3.0: DISCUSSION OF THE RESULTS:

The experimental results indicated that

1. there exist operating regimes, which had not been exploited, that could enhance the substrate copper-to-argon ion fraction (which was about 10% for the typical run conditions of $1mtorr$ argon pressure, $4kW$ microwave power, $230A / 180A$ electro-magnet settings, $-1kV$ target voltage) by a factor of 4 to 5: these regimes were located at greater pressures ($> 2mtorr$) and lower electro-magnet settings ($160A / 160A$),
2. the copper flux incident on the substrate was more than 90% ionized for all run conditions, and
3. an increase in microwave power degraded copper deposition uniformity.

Result #2 suggested that the copper ion-to-neutral fraction at the substrate was not a factor in our failure to fill the 'high' aspect ratio trenches ($A \geq 2.4$). Because deposition uniformity was not a pertinent issue, we adjusted the run conditions according to result #1. Once again the fill results were dismal; even though we had improved $f^{sub}_{Cu^+/Ar^+}$ by a factor of 4, we neither succeeded in filling the 'high' aspect ratio features nor observed any improvements in the fill quality. The question that remained was whether the improvement in $f^{sub}_{Cu^+/Ar^+}$ was not enough (in other words, did we need to push $f^{sub}_{Cu^+/Ar^+}$ to a value greater than 90% $\Rightarrow$ no argon). Before, we address this question, we will discuss a very important process parameter, the discussion of which we have postponed up to now: **substrate biasing**.

Substrate biasing has a tremendous effect on the fill quality because it controls the ion momentum and energy via the potential change in the sheath

$$\begin{aligned}\Delta\Phi_{sheath}^{bias} &= \Phi_{plasma} - V_{substrate} = \Delta\Phi_{sheath}^{float} + \left(\Phi_{float} - V_{substrate}\right) \\ \Delta\Phi_{sheath}^{float} &= \left(\Phi_{plasma} - \Phi_{float}\right)\end{aligned} \quad [3.0-1];$$

as discussed in chapter 1, the ratio of the ion (argon or copper) parallel-to-perpendicular (to the surface normal) momentum determines the directionality $\langle\theta_{inc}\rangle$, and its energy controls deposition (via sputtering of the deposited copper film).

The sensitivity of the fill quality to the substrate bias was exploited simultaneously with experimentation with the other process parameters (pressure, power,...); however, the data presented in the previous chapters were obtained with the substrate floating (no bias) so that we may isolate the influence of substrate biasing. Much of what we said in regard to the dismal results we obtained for the fill quality variation with pressure and power with no substrate bias is also true for the fill quality with substrate bias.

We employed two methods for biasing the copper substrate via a coaxial chuck: radio-frequency (RF) and direct current (DC). For either method to have been successful, the bias on the substrate needed to couple the voltage to the trenches, in which we wanted to deposit the copper. However, the trenches are a dielectric, $SiO2$, and they are situated on a wafer, which is, itself, a dielectric ($SiO2$). DC biasing was made possible by the thin electrically conducting coating of TiN (which also served as an adhesive for the deposited copper film and as a diffusion barrier) on the trenches and a metal clip, which formed the contact between the top of the wafer and the substrate. However, the large resistance of the thin metal layer created a voltage drop across the wafer, rendering the biasing of the

wafer non-uniform. RF biasing is the more attractive option for processing because it does not require a conducting path to the wafer; hence, it can be applied uniformly. The sheath physics resulting from the two biasing methods is, of course, different; the DC bias accelerates the ions by an energy equal to the potential drop across the sheath; whereas the RF bias renders a time varying potential drop, and the ion gains a different amount of energy depending on the phase of the RF cycle upon the ion's entrance into the sheath and on the product of the bias frequency and the ion sheath transit time. We note that the ion will never decelerate because the substrate potential will never exceed the plasma potential. Why?

In RF biasing, there can not be a net charge transfer thorough the substrate (the substrate is electrically isolated from ground), hence, (see figure 3.0-1) the surface potential will begin to charge negative (more negative than the floating potential) because the ions don't have the mobility (compared to the electrons) to reach the surface on the 'negative' half of the cycle (which attracts ions). The surface will finally reach a "self-biasing" potential about which it oscillates. Now, because of the large disparity between the ion and electron mobility (electron's mobility being much greater), for the greater part of the cycle, the surface potential will be below the floating potential.

FIGURE 3.0-1: A SHEMATIC OF THE DYNAMICS OF RF BIASING

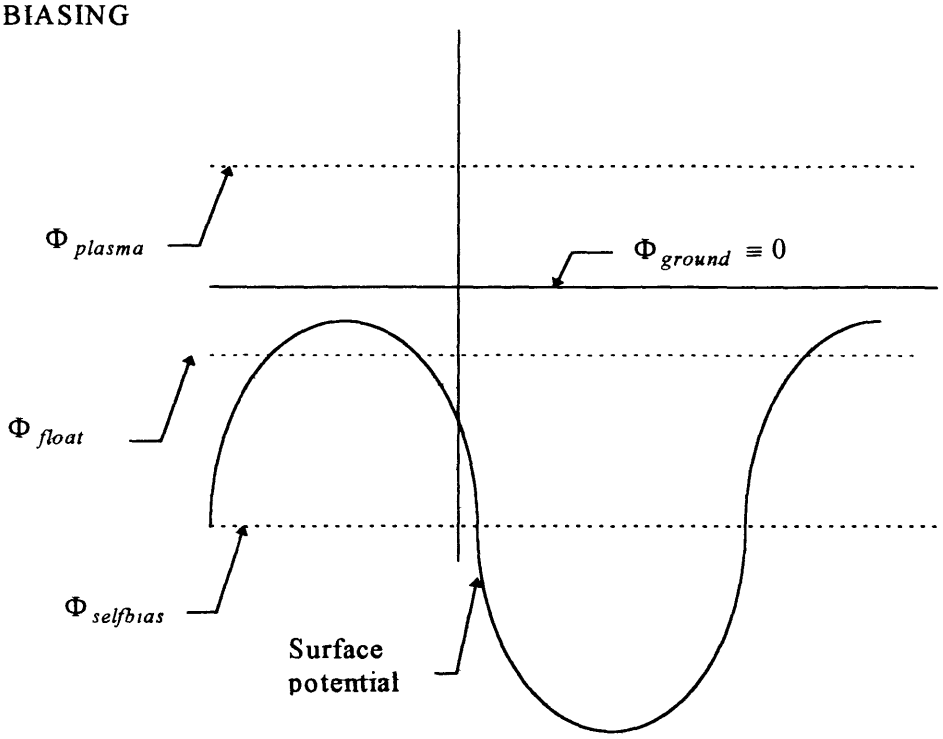

There are more detailed discussions of the effects of RF biasing in[1] and [2].

With DC bias, we were limited to a voltage of $|V_{sub}| \leq 50V$ because of etching of the dielectric (a phenomenon know as faceting); see figure 3.0-2. At a large substrate voltage, the argon and copper ions would gain enough energy to sputter the deposited copper on top of the trench and also sputter the dielectric (the etching of the dielectric would take place at the corners because sputtering coefficients have a maximum at an oblique incidence of $\approx 60°$ [3]); there would still be deposition within the trench because the sputtered copper would stick to the side-walls (the sputtered copper within the trench is trapped).

---

[1] John B.O. Caughman and W. M. Holber, J. Vac. Sci. Tech. A 9 (6), Nov/ Dec 1991, pp. 3113-3118
[2] John B.O. Caughman, J. Vac. Sci. Tech. A 11 (6), Nov/ Dec 1993, pp. 2897-2902
[3] H. Oechsner, Appl. Phys. **8**, pp.185-198 (1975)

FIGURE 3.0-2: AN ILLUSTRATION OF THE ETCHING OF THE TRENCH CORNERS AND THE TRAPPING OF THE COPPER SPUTTERED INSIDE THE TRENCH

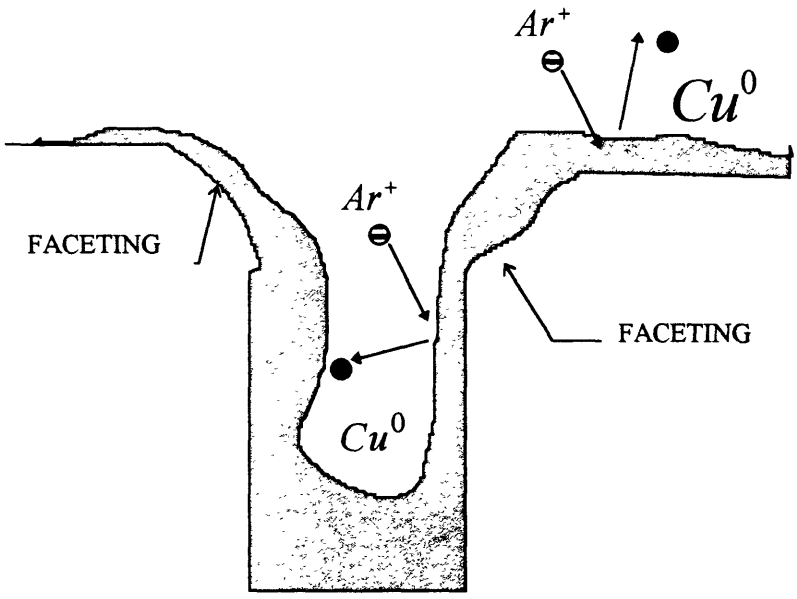

The RF bias voltage also had similar limitations with $\left|V_{peak-peak}\right| \leq 80V$; the larger value for the RF voltage resulted from a fraction of the ions not gaining the complete energy from the peak-to-peak voltage because of the temporal evolution of the voltage during the ion's flight through the sheath and the voltage phase at the time of the ions' arrival into the sheath. To understand the influence of the voltage time variation on the ion's energy, we will need an estimate of the product of the ion sheath transit time and the frequency of the RF voltage: The general equation of motion for the ion is

$$v\cdot\left[\frac{d^2}{dt^2}x=\frac{eE(x,t)}{m_{ion}}\cong\frac{-e}{m_{ion}}\frac{\partial}{\partial x}\Phi_{sheath}(x,t)\right]\Rightarrow$$

$$\frac{d}{dt}\left(\left(\frac{dx}{dt}\right)^2\right)\cong\frac{-e}{m_{ion}}\left(\frac{d}{dt}\Phi_{sheath}(x(t),t)-\frac{\partial}{\partial t}\Phi_{sheath}(x(t),t)\right)\Rightarrow \qquad [3.0-2]$$

$$\left(\frac{dx}{dt}\right)^2+\frac{e}{m_{ion}}\Phi_{sheath}(x(t),t)-\left(v_0^2+\frac{e}{m_{ion}}\Phi_{sheath}(0,0)\right)\cong\frac{e}{m_{ion}}\int_0^t dt'\frac{\partial}{\partial t}\Phi_{sheath}(x(t'),t')$$

Assuming that

1. the ion transit frequency is much greater than the frequency of the voltage applied

2. the initial ion energy is much smaller than the energy gain through the sheath

$$\left(\frac{T_e/2}{e\Delta\Phi_{sheath}}\approx\frac{2eV}{40eV}<<1\right)$$

3. constant electric field in the sheath, $E_{sheath}\approx\frac{\Delta\Phi_{sheath}}{d_{sheath}}$,

we can obtain a simple estimate for the ion sheath transit time,

$$\tau_{transit}^{ion}\approx\left(\sqrt{\frac{d_{sheath}^2}{0.5*\left(e\Delta\Phi_{sheath}/m_{ion}\right)}}\right)\approx 0.01\rightarrow 0.1\mu\sec\,[3.0-3].$$

For the applied source frequencies, which ranged from 13 to $90MHz$, the product of the transit time with the source frequency was ≈ 1. Hence the ion dynamics was strongly perturbed by the varying voltage. To observe the perturbation, we will solve the equation of motion for a simple sheath potential profile (see figure 3.0-1):

$$\Delta\Phi_{sheath}(x,t)=\left[\Phi_{self-bias}+0.5\cdot V_{peak-peak}*\sin(\omega\cdot t+\varphi)\right]\cdot\frac{x}{d_{sheath}}\;[3.0-4];$$

$$\Phi_{self-bias}\approx\Phi_{float}-0.5\cdot V_{peak-peak}$$

using typical values for the sheath thickness, the applied voltage, and the floating potential,

$$\Phi_{float} \approx -20V$$
$$V_{peak-peak} \approx 80V,$$
$$d_{sheath} \approx 0.1mm$$

we plot the position of the ion with time for different frequencies and initial phases of the RF potential (φ):

FIGURE 3.0-3: TEMPORAL EVOLUTION OF THE ION'S POSITION THROUGH THE SHEATH FOR A RANGE OF SOURCE FREQUENCIES AND INITIAL PHASES.
$d = 0m$ CORRESPONDS TO THE PLASMA-SHEATH INTERFACE, AND
$d = 10^{-4}m$ CORRESPONDS TO THE SURFACE.

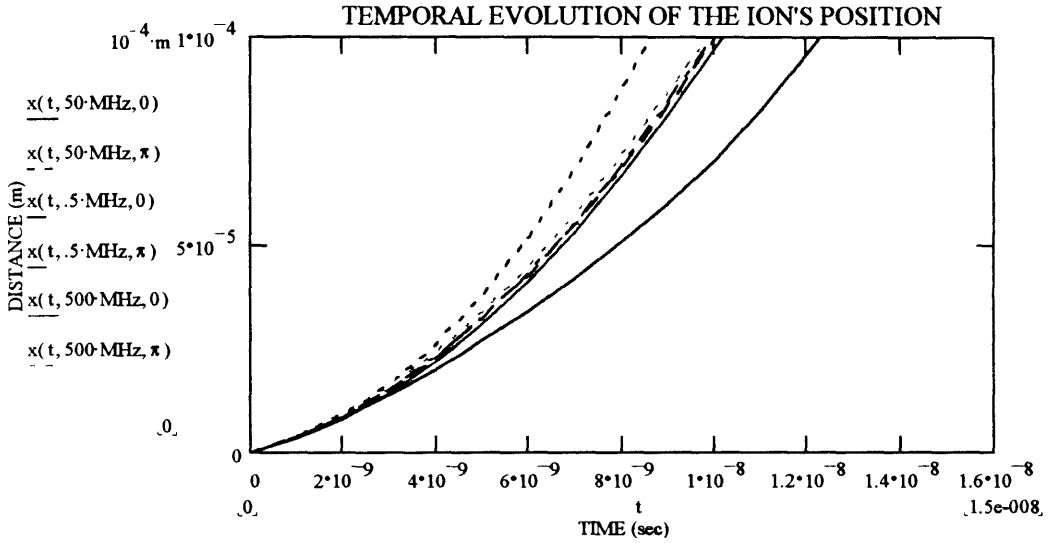

Figure 3.0-3 shows that the typical sheath transit time is $\approx 10^{-8}$ sec = 0.01μsec, which is consistent with the previous estimate. It also demonstrates that the phase of the source voltage at the time of the ion's entrance into the sheath has an impact on the ion's trajectory for frequencies at or below $50MHz$; whereas for larger frequencies, the ion feels the 'average' potential, $\Phi_{self-bias}$, and the initial phase does not matter. The next

two figures, 3.0-4 and 3.0-5, show the temporal evolution of the ion's speed for large and moderate frequencies for different voltage phases:

FIGURE 3.0-4: THE TEMPORAL EVOLUTION OF THE ION'S SPEED AT A LARGE SOURCE FREQUENCY FOR DIFFERENT SOURCE PHASES.

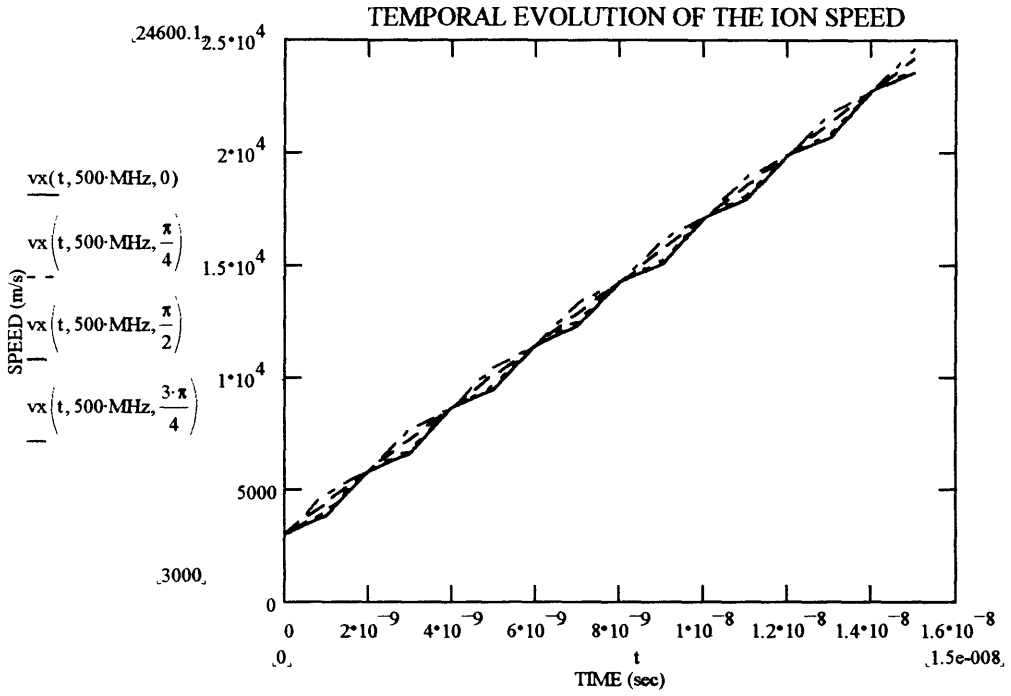

FIGURE 3.0-5: THE TEMPORAL EVOLUTION OF THE ION'S SPEED AT A MODERATE SOURCE FREQUENCY FOR DIFFERENT SOURCE PHASES.

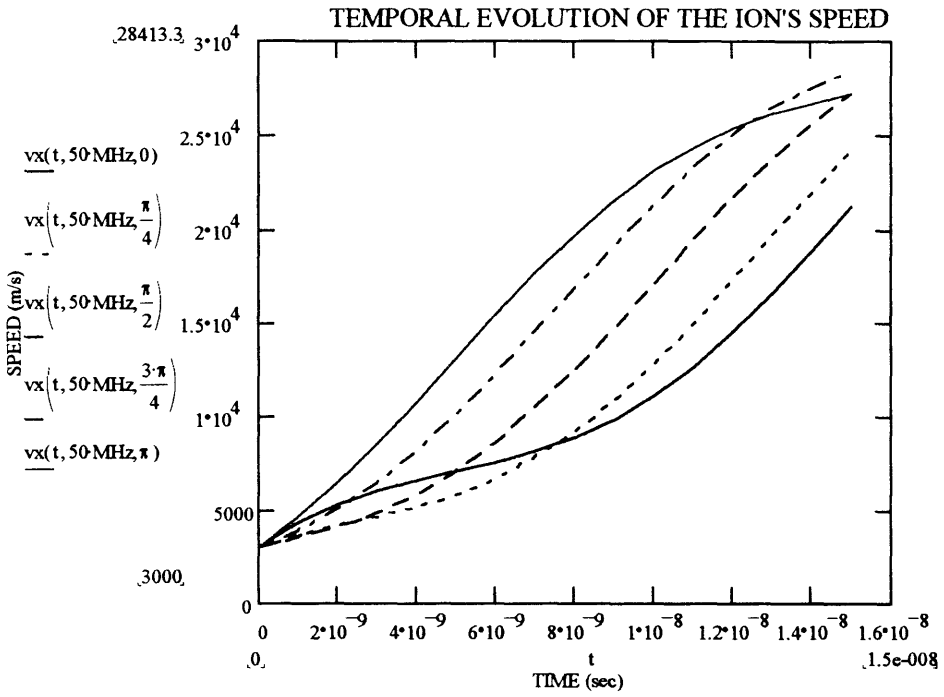

The two figures illustrate the weak influence of the voltage phase on the ion's motion for large frequencies and the strong influence of the phase for moderate frequencies. Hence for the range of our source frequencies, 13 to $90MHz$, we can see that the ion's energy at the surface will be heavily influenced by the phase of the source at the time of its arrival into the sheath. This dependence results in a spread in the energy gained by the incident ion flux with the average energy gained corresponding to a sheath voltage drop of $\Delta\Phi \approx 20V + .5 * V_{peak-peak} = \Delta\Phi_{floating} + .5 * V_{peak-peak}$.

The point to take away is that the bias for both RF and DC was limited to $[V_{DC}, 0.5 \cdot V_{RF}] \leq [50V, 50V]$; hence, we were not able to explore the effects of a larger

bias. This limitation brings us back to the issue regarding the influence of $f^{sub}_{Cu^+/Ar^+}$.

There are now two reasons for maximizing the value of $f^{sub}_{Cu^+/Ar^+} \to 1$:

1. the first, as mentioned before, is to determine whether pushing the value of $f^{sub}_{Cu^+/Ar^+} > 50\%$ would modify the fill quality (with no bias),

2. the second is to enable a larger substrate biasing range ($V_{BIAS} \geq 100V$); as mentioned in section 2.2 and 2.3, for the typical run conditions, $f^{sub}_{Cu^+/Ar^+} \leq 20\%$ and $f^{sub}_{Cu^+/Cu^0} > 90\%$, therefore, the deposition rate at the top of the trench, which is determined by the general relation

$$\dot{D}ep = Area \cdot \left(\left(T_{Cu/Cu} - S_{Cu/Cu} \right) \cdot \Gamma_{Cu^+} + \Gamma_{Cu^0} - S_{Cu/Ar} \cdot \Gamma_{Ar^+} \right) \Rightarrow$$

$$\Gamma_{Cu^+} \cdot Area \cdot \left(-ST_{Cu/Cu} + \left(\frac{1}{f^{sub}_{Cu^+/Cu^0}} - 1 \right) - S_{Cu/Ar} \cdot \left(\frac{1}{f^{sub}_{Cu^+/Ar^+}} - 1 \right) \right) [3.0-5],$$

$$\approx \Gamma_{Cu^+} \cdot Area \cdot \left(-ST_{Cu/Cu} - 9 \cdot S_{Cu/Ar} \right)$$

is positive for $\left(-ST_{Cu/Cu} - 9 \cdot S_{Cu/Ar} \right) > 0 \Leftrightarrow \frac{-ST_{Cu/Cu}}{S_{Cu/Ar}} > 9$; this inequality limits the incident ion energies to a value below $50eV$, thereby, as discussed, limiting the substrate bias voltage. For $f^{sub}_{Cu^+/Ar^+} = 1$ (no argon ions), we will have net deposition for copper ion energies at or below $\approx 180eV$ because below this energy the copper sputtering coefficient is less than its sticking coefficient ($ST_{Cu/Cu}\left(E_{inc} \leq 180eV\right) \leq 0$, see section 2.2 for details).

To eliminate the argon, we employed a copper evaporative source because we could not sustain the discharge with the sputtered copper from the target alone. The

evaporative system consisted of a DC voltage source, copper square bars ($l \approx 1 \rightarrow 2cm$), and a "heat bath" in series with the copper bars, which contained high refractory metal bars (tungsten, which has low thermal conductance relative to copper) holding a tungsten crucible filled with copper pellets ($\approx mm$ in diameter). Large currents flowing through the copper bars would heat the tungsten to temperatures of order $T_{melting}^{Cu} \approx 1000°K$, which would melt and subsequently evaporate the copper pellets. The heat bath was situated a few inches above the substrate with crucible's opening facing the copper target, illustrated in figure 3.0-6:

FIGURE 3.0-6: FIGURE 1.0-3 WITH THE ADDITION OF THE COPPER EVAPORATION SYSTEM

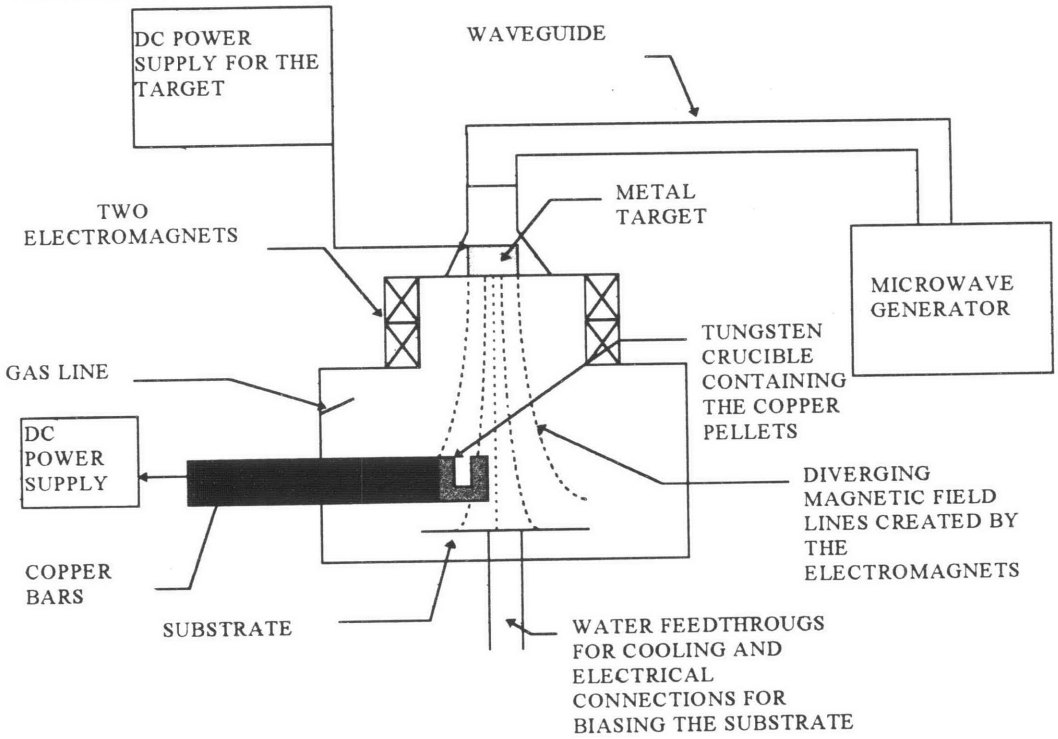

The procedure for running the plasma source with the evaporator was to ignite an argon plasma, begin the evaporation process, then gradually reduce to argon flow rate to zero (we did not use the copper target). The copper evaporation rate was about $.1 grams/\min$

(the crucible could hold about $1gram$ of copper, and the copper completely evaporated within ten minutes).

The evaporated copper would then be ionized by the microwave and follow the field lines to deposit on the substrate. Because the copper evaporated towards the target, the only way copper neutrals could reach the substrate would be through back-scattering (which requires a small collision mean-free path or equivalently a large copper neutral density). To estimate the copper neutral density profile, we will model the evaporation source as a point source and assume that diffusion dominates:

$$\nabla \cdot \vec{\Gamma} = \frac{1}{r^2}\frac{\partial}{\partial r} r^2 \Gamma_r = 0 \Rightarrow \Gamma_r = \Gamma_o \left(\frac{r_0}{r}\right)^2$$

$$\Gamma_r = -D\nabla n$$

$$D = \frac{v_{th}}{n\sigma} \qquad [3.0-6],$$

$$v_{th} \approx 500 m/s$$

$$\sigma \approx 10^{-14} cm^2$$

the solution of which is

$$n = n_0 \exp\left(\frac{\Gamma_0 a\sigma}{v_{th}}\left(\frac{a}{r} - 1\right)\right) [3.0-7],$$

where '$a \approx 1cm$' is the radius of the crucible and

$$\Gamma_0 \cong \frac{(.1g/\min)N_{Av}}{64 gram/mol} \frac{1}{Area_{crucible}} \approx 5 \cdot 10^{18}/cm^2 \cdot \sec$$

$$n_0 \approx \frac{\Gamma_0}{v_{th}} = 10^{14} cm^{-3}$$

$$\frac{\Gamma_0 a\sigma}{v_{th}} \cong 1$$

Therefore, the density in the chamber is $\approx n(r = 10cm) \cong \frac{n_0}{2} = 5 \cdot 10^{13} cm^{-3}$. The corresponding mean-free path for back-scattering is $\lambda = \frac{1}{n\sigma} \approx 2cm$; hence it's possible for the copper flux towards the substrate to consist of some back-scattered copper neutrals. However, the copper neutral flux fraction was experimentally determined to be insignificant via the comparison of the substrate current density of $\approx 2.3 mA/cm^2$ (due solely to the copper ion flux, remember that there is no argon) and the copper deposition rate of $\approx 0.1 \mu m/\min \Leftrightarrow 2.3 mA/cm^2$ (due to both the copper ion and neutral flux).

With the evaporation source, we were able to experimentally simulate the ideal condition: $f^{sub}_{Cu^+/Ar^+} = 1$ and $f^{sub}_{Cu^+/Cu^0} = 1$, a pure copper ion flux incident on the substrate. Hence, besides the substrate bias, we had no parameter to vary except for the microwave power, which controlled the rate of deposition through increased ionization of the evaporated copper; the copper neutral pressure, which is a function of the evaporation rate was out of our control.

The ideal conditions enabled us to test whether the conditions within the plasma had any bearings on the fill quality. We attempted to fill the trenches without using a substrate bias (substrate floating); with this condition we filled trenches with aspect ratio $A \leq 2.4$, which was slightly better than what we had done with an argon plasma $A < 2.4$ (remember that the height of our trenches were $h = 1.2 \mu m$, therefore, aspect ratios $A \leq 2.4$ was equivalent to trench widths $w \geq 0.5 \mu m$). However, we noticed something peculiar upon the introduction of DC substrate bias, which is illustrated in figure 3.0-7:

FIGURE 3.0-7: ILLUSTRATION OF THE COPPER FILL QUALITY WITH DC BIAS, USING A COPPER EVAPORATION SOURCE, WHICH YIELDS A PURE COPPER ION FLUX TO THE SUBSTRATE

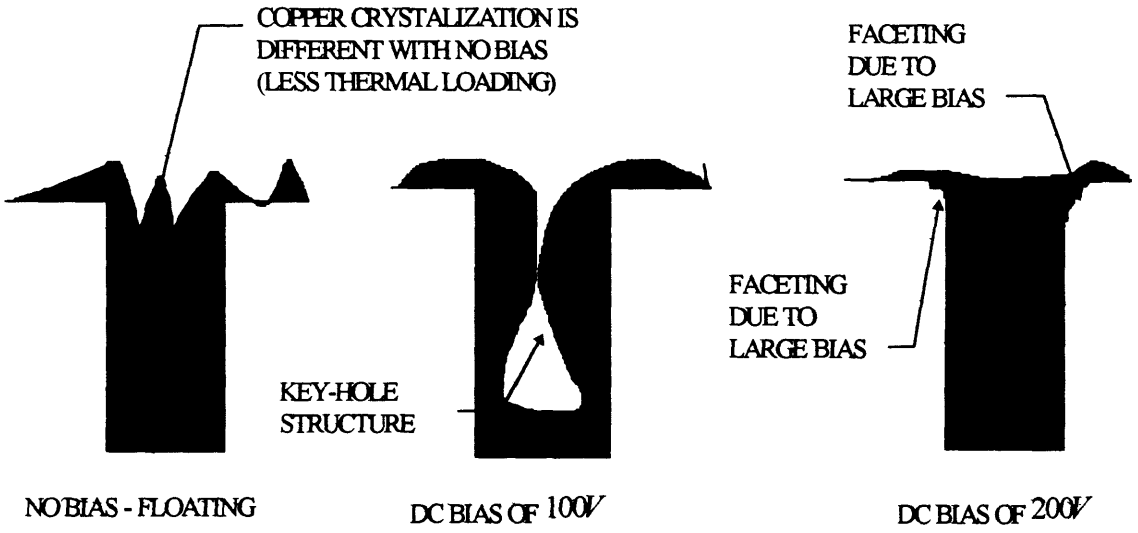

the fill quality was degraded for a DC bias $\leq 100V$ (we observed the phenomenon of pinch-off, which left a key-hole inside the trench) but improved for bias voltages of order $200V$ (remember that the self-sputtering coefficient, $ST_{Cu/Cu}$, switches sign at this voltage from net deposition to net etching; hence, we could not go above this voltage without etching the dielectric).

The improvement in the fill quality for $V > 100V$ suggested that sputtering within the trench was not as detrimental as once thought; hence, it may be possible to obtain the same results with argon present provided that we use a dielectric that can withstand ion energies above $200V$ such as some polymers being investigated at the present. There is another issue for the use of DC biasing: the preservation of the conducting path to the trench. Once the copper film is sputtered from the trench top, the conductive TiN coating will become exposed and will be sputtered away with the dielectric. The sputtering of the conductive coating will cut-off the electrical path, and the trench voltage

will float (as in the case of no biasing). This problem can be alleviated by embedding a conductive path within the dielectric (which may not be desirable because it adds to the complexity of the metallization process) or by using RF biasing.

Figure 3.0-7 also suggests that the metallization process maybe quite insensitive to the conditions within the plasma and that the understanding of the process will result from the modeling of the metal film formation (which is controlled by metal film parameters such as metal film surface tension, metal film adhesion, particle and heat diffusion within the metal film), and the influence of the ion incident heat flux on these film parameters as well as detailed information regarding the differential sputtering yields, $\left(dS/dEd\Omega\right)_{Ar/Cu}, \left(dS/dEd\Omega\right)_{Cu/Cu}$, which are described in section 1.1.

Finally, there is a technique by the name of 're-flow', which can be used in conjunction with a metallization process to enhance the fill quality. This method uses local laser heating to melt the deposited metal so that the metal film will flow into the trenches and fill any voids. This method has been proven successful in filling sub-micron features with aspect ratios ≥ 4; the drawback being, of course, the increase in the process complexity.

7042-67